Physical and Mathematical Modeling in Billet Molds for Steel Quality Improvements

by

Ken Morales-Higa

Department of Mining and Materials Engineering

McGill University, Montreal, Canada

August, 2014

A thesis submitted to McGill University in partial fulfillment of the requirements of the degree of Doctorate of Philosophy

ABSTRACT

The continuous casting of billets can be associated with defects such as inclusions, oscillation marks, centerline segregation, depressions and Mold Powder Entrainment (MPE). Mathematical simulations and physical measurements in a full-scale water model of round and square billet casters, corresponding to those operated at the Rio Tinto Fer et Titane (RTFT) plant located at Sorel Tracy, Quebec, Canada, were employed to unveil possible MPE mechanisms. The physical modeling included dye tracer injection with fast video recording, Particle Image Velocimeter (PIV) and water-oil experiments. For both round and square billet casters, flows present are asymmetric, and intermittent vortex flows are formed throughout the volume of both types of mold and near the meniscus region, under different operating and casting conditions, including low casting speeds. The strong flows impingements compromise uniform growth of the steel shell, while the fluctuations in the meniscus influence the generation of MPE and subsequent subsurface defects. The observed fluid flow patterns when operating with a proposed alternative for a Submerged Entry Nozzle (SEN) design, reduced the impingement of jets on the forming steel shells, and decreased mold level fluctuations in the meniscus region, as compared with the results delivered by the current operations.

RÉSUMÉ

La coulée continue de billettes d'acier peut être associée à des défauts comme des inclusions, des marques d'oscillation, des ségrégations de la ligne du centre, des dépressions et de la rétention de moule poudre (MPE). Des simulations mathématiques et la prise de mesures physiques sur un modèle à eau plein échelle pour la coulée des billetées rondes et carrés, correspondant à ceux utilisés par l'usine Rio Tinto Fer et Titane (RTFT) située à Sorel Tracy, Québec, Canada, furent employés pour révéler les possibles mécanismes de MPE. Le modèle physique inclus l'injection d'encre avec l'enregistrement de vidéo rapide, la vélocimétrie d'image particule (PIV) et des expérimentations avec l'eau et l'huile. Tant pour las lingotières rondes que pour las lingotières carrées, les flux sont asymétriques, et des vortex de flux intermittents se forment au long du volume des deux types de lingotières et près de la région du ménisque sous différentes conditions de coulée et d'opération, incluant de basses vitesses de coulée. Les fortes collisions des jets compromettent la croissance uniforme des couches d'acier, alors que las fluctuations de ménisque influence la génération de MPE et de subséquentes surfaces défectueuses. Les patrons d'écoulements de liquide observés lorsque opérant avec l'alternative proposée pour un design de submergée buse d'entrée (SEN), réduit la forte collision des flux sur la couche d'acier en solidification ainsi que la fluctuation des niveaux du moule dans la région du ménisque en comparaison avec les résultats obtenus par l'opération courante.

ACKNOWLEDGEMENTS

I owe my deepest gratitude to my supervisor, Professor R.I.L. Guthrie and co-supervisor Dr. Mihaiela Isac, for their constant effort in providing the guidance, support and academic advice from the beginning to the end of my studies at the MMPC.

I am grateful to the National Council of Science and Technology in Mexico (CONACyT) for their financial support during my Ph.D. studies.

I would also like to thank the Natural Sciences and Engineering Research Council of Canada (NSERC) for their financial support from the beginning to the end of my studies.

In addition, a thank you to the Roberto Education Program (RREP) for their financial support and the opportunity provided for becoming a fellow of this program.

I would also like to thank National Institute Polytechnique in Mexico (IPN) for the support given during the physical experiments.

Special thanks to Francis Lapointe and Chantal Labrecque from Rio Tinto Fer et Titane (RTFT) for their close collaboration and the help provided for this project.

Lastly I wish to thank my family. I am in deep gratitude to my mother Naoko for her moral and emotional support and to my sister Erika for her encouragement. I would like to express my sincere gratitude to my father Rodolfo for his patience, unconditional support and guidance.

NOMENCLATURE

ρ : Density, $\mathrm{kg/m^3}$

g : Gravitational acceleration, $\frac{m}{s^2}$

μ : Molecular viscosity, kg/m*s

v : Kinematic viscosity, $\frac{m^2}{s}$

u : Instantaneous Velocity, $\frac{m}{s}$

P : Pressure, $\frac{N}{m^2}$

μ_{eff} : Effective viscosity, kg/m*s

μ_l : Laminar viscosity, kg/m*s

G : Generation of kinetic energy of turbulence, $\frac{m^2}{s^2}$

μ_t : Turbulent viscosity, kg/m*s

k : Kinetic energy of turbulence per unit mass of fluid, $\frac{m^2}{s^2}$

ε : Dissipation rate of kinetic energy of turbulence, $\frac{m^2}{s^3}$

Q : Volumetric flow rate, $\frac{L}{min}$

V_c : Casting speed, m/s

a : Fluid acceleration, $\frac{m}{s^2}$

σ: Surface tension, $\frac{N}{m}$

L_m: Characteristic length, *m*

λ : Scale factor

K : Thermal conductivity, W m^{-1} K^{-1}

τ_{ij}^{l} : Laminar viscous stresses, $\frac{N}{m^2}$

τ_{ij}^{t} : Reynolds stresses, $\frac{N}{m^2}$

y+ : Dimensionless wall distance

m, p, Subscripts indicate model and prototype respectively

Γ_{eff} : Effective diffusivity, m^2 s^{-1}

D_{eff} : Effective diffusion coefficient, m^2 s^{-1}

C_D : Drag coefficient

d_p : Particle diameter, m

u_p : Particle velocity, m/s

ρ_p : Density of the particle, kg m^{-3}

H : Enthalpy, J/kg

T : Temperature, K

T_{liq}: Temperature liquidus, K

T_{sol} : Temperature solidus, K

T_{break} : Break point temperature, K

K_{eff} : Effective thermal conductivity, W m^{-1} K^{-1}

Q : Heat source, W/m^3

ζ : Vorticity vector, s^{-1}

H : Magnetic field, A m^{-1}

E : Electric field, V m^{-1}

B : Magnetic flux density, T

J : Conduction current density, A m^{-2}

φ : Gradient of a scalar potential

C_i : Instantaneous dimensionless concentration

u : x component of velocity, m s^{-1}

v : y component of velocity, m s^{-1}

w : z component of velocity, m s^{-1}

F_D : Drag force, N

VOF: Volume of Fluid

TKE: Turbulence Kinetic Energy

DNS: Direct Numerical Simulation

DPM: Discrete phase modelling

SIMPLE: Semi-Implicit Method for Pressure Linked Equations

PISO: Pressure Implicit Splitting of Operators

PRESTO: Pressure Staggering Option

PST: Positive strip time

NST: Negative Strip time

EMS: Electromagnetic Stirring

EMBr: Electromagnetic Braking

M-EMS: Mold Electromagnetic Stirring

S-EMS: Strand Electromagnetic Stirring

F-EMS: Final Electromagnetic Stirring

TABLE OF CONTENTS

1.0 Introduction

During the last five decades, the steel industry has been evolving rapidly, largely because of the continuous casting process. Continuous Casting reduces additional processes involved in Ingot Casting. Therefore, several advantages are attained, such as a reduced number of operations, equipment, energy consumption, labor and time requirements.

Prior to the continuous casting step, molten metal is tapped from the furnace into a teeming ladle for secondary steelmaking operations. After degassing, alloying, and fixing the casting temperature, the ladle is positioned above the bottomless molds of the continuous casting machines. The de-oxidized liquid steel is then transferred from the ladle through a ladle shroud into a tundish (see Figure 1.1). The refractory shroud is used to protect the incoming steel from being in contact with air, as the shroud itself is sealed to the outlet of the ladle. The steel flow rate into the tundish is controlled by the ladle shroud which is fitted by a slide gate valve, or equivalent. The bottom of the shroud is submerged in the steel bath within the tundish, except during a ladle change. The tundish vessel feeds liquid steel into a series of molds for the casting machines set below. This typically employs a series of Submerged Entry Nozzles (SEN´s). The open casting molds set below are made of copper and are cooled with water. Mold fluxes are added and constantly supplied to the top of each mold during casting, so as to prevent the freezing steel shells from sticking to the walls of the copper mold once solidification has begun. Sticking of freezing steel to the mold walls is further prevented by oscillating the molds. On leaving its mold, the surface of the strand between the support rolls is cooled down by water sprays or air sprays, until the steel core is completely solidified.

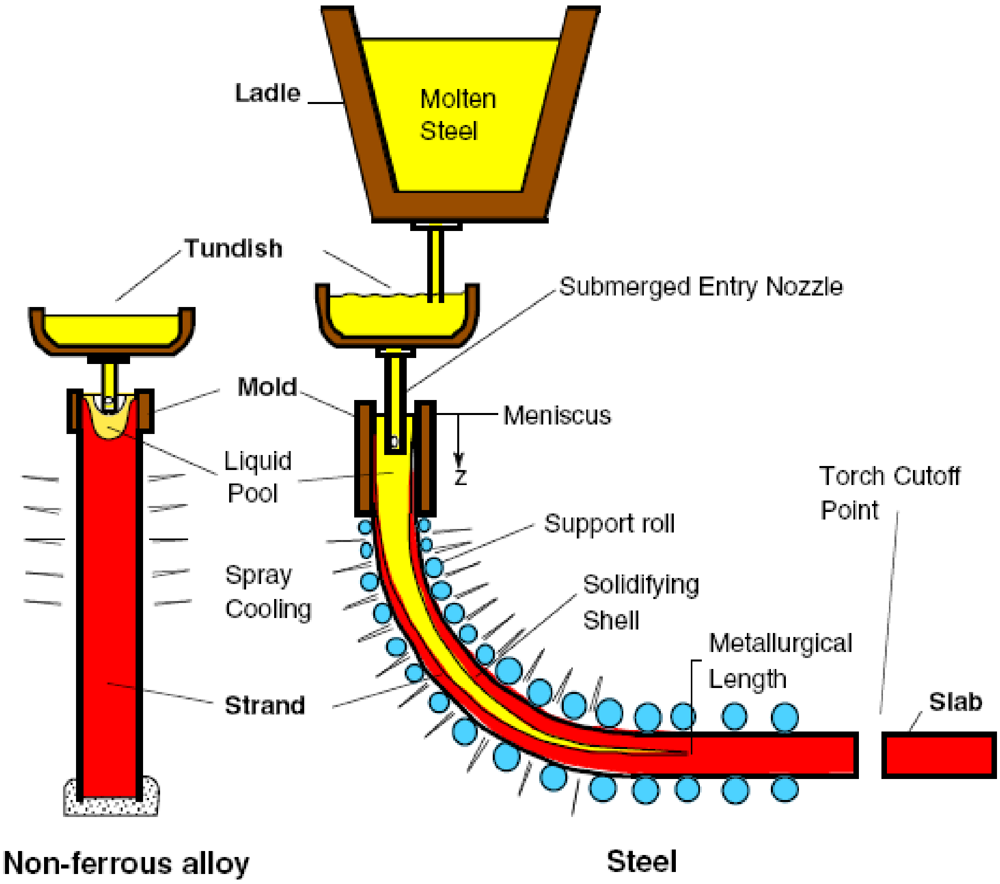

Figure 1.1 Schematic diagram of the elements and processes in the continuous casting machine[1].

During continuous casting, the most critical stage of the process begins when liquid steel first enters into the mold through the nozzle. There, different variables that act conjointly, determine the quality of the final product. The difficulties related to the process are the need for proper control of the casting velocity, mold oscillation, cooling conditions, precise control of superheat temperature, and the proper selection of mold powder for lubrication.

An inherent part of the continuous casting process that has a strong influence in the quality of steel and remains a challenge for improvement is the control of turbulent flows of steel within the molds. The turbulent flows inside the molds are triggered as soon as the gravity driven liquid metal exits through the SEN ports, producing high momentum discharging jets that can penetrate deeply into the molten metal bulk. This introduction of liquid metal generates high frequency turbulent flows that spread throughout the bulk of the liquid metal causing high velocity gradients which are not welcome, particularly those comprising the liquid steel/slag interface, or the shell-mold gap where mold lubricant is flowing; These velocity fluctuations can lead to variations in slag flux infiltration, in resultant heat flux withdrawal, as well as defects related to Mold Powder Entrainment. All these variations can result in deleterious effects to the quality of the final steel product. Furthermore, the transient fluid flows can be increased by changes in the caster operating conditions. The changes in the operating conditions include: stopper-sliding gate aperture, casting speed, nozzle misalignment, nozzle submergence depth, EMS and EMBr practices.

In the current operation at Rio Tinto Fer et Titane (RTFT), MPE defects have been detected in both square and round billets, for different casting speeds and different conditions. These sub-surface defects formed by MPE are present even when careful control of the casting operation is conducted, and represents a major drawback to the quality of the final product. In addition, their immediate detection during the process is very difficult. Therefore, the first objective pursued in the present thesis was to extend the existing fundamental knowledge of the intermittent-transitory flows encountered inside round and square billet molds, and their interactions with mold slag. The second objective was to propose improved arrangements and operating conditions that could lead to overall improvements in RTIT's continuous casting practices. For that purpose, physical and mathematical modeling of flows entering round and square billet molds were conducted, in order to explain the vortex formation, fluid flow phenomena and the possible causes of MPE in their continuous casting process. CFD was conducted using the commercial software ANSYS-FLUENT 14, while PIV and other physical measurements to study transient flows were used extensively to check CFD computations.

A general review of the physical and mathematical modeling work associated with continuous casting molds is presented in Chapter 2, while the modeling procedures are discussed in Chapter 3. Fluid flow patterns and MPE mechanisms in the round and square molds are explained in Chapter 4 and 5 respectively. At the end of both those chapters, the effects of misaligned nozzles on the resulting fluid flows within the molds are discussed. A thorough analysis on proper SEN design and operating conditions for process improvement was carried out and these are presented in Chapter 6. Finally, in Chapter 7, general conclusions and future work is discussed. At the beginning and at the end of each chapter, an introduction and summary of the results are presented.

2.0 Literature Review

2.1 Physical modeling

The difficulties that are entailed in industrial trials in the continuous casting process, for liquid steel, such as operating at high temperatures, using sophisticated equipment, etc., made the study of fluid flow in molds through low temperature physical modeling a more suitable option for tests and to improve operations and processes. In the physical model, steel is replaced by water which is readily available, much simpler to handle, and reduces the costs of material and experimental setups. This is possible owing to the fact that the kinematic viscosity of water at 20°C is very similar to that of liquid steel at 1600 °C [2, 3]. The properties are listed in Table 2.1.

Property	Water (20°C)	Steel (1600 °C)
Density, ρ, $\left(\frac{kg}{m^3}\right)$	1000	7014
Molecular viscosity ,μ, $\left(\frac{kg}{m*s}\right)$	0.001	0.0064
Kinematic viscosity, $\nu = \frac{\mu}{\rho}$, $\left(\frac{m^2}{s}\right)$	1×10^{-6}	0.913×10^{-6}
Surface tension, σ, $\left(\frac{N}{m}\right)$	0.073	1.6

Table 2.1 Properties of water and steel

The accurate construction of a water model for an actual mold operation requires the fulfillment of "similarity criteria" that correspond to constant ratios of forces and scalar quantities between the model and prototype. The diverse states of similarity include geometric, thermal, chemical, kinematic and dynamic similarity.

To obtain geometrical similarity, all dimensions must obey the following relationship:

$$L_m = \lambda L_p \qquad \text{[Eq. 2.1]}$$

The most relevant forces involved in fluid flow phenomena in the continuous casting process include: inertial, gravitational, viscous, buoyancy, and surface tension forces. Given that steel flows in molds are basically gravity driven and highly turbulent, inertial and gravitational forces are of high relevance during the process. Therefore, Reynolds and Froude similarity criteria most both be satisfied if an accurate representation of the process is to be pursued. To obtain this, the use of a full scale water model 1:1 is necessary. The ratio of inertial to viscous forces in the model and prototype is described as:

$$Re_m = Re_p \qquad \text{[Eq. 2.2]}$$

$$\left(\frac{\rho U}{\mu}\right)_m = \left(\frac{\rho U}{\mu}\right)_p \qquad \text{[Eq. 2.3]}$$

Similarly, the ratios of inertial to gravitational forces are described as:

$$Fe_m = Fe_p \qquad \text{[Eq. 2.4]}$$

$$\left(\frac{U^2}{\mathrm{gL}}\right)_m = \left(\frac{U^2}{\mathrm{gL}}\right)_p \qquad \text{[Eq. 2.5]}$$

All similarities criteria cannot be satisfied simultaneously as other properties between water and steel greatly differ, such as surface tension which is neglected when working with full scale water models. For successfully representing steel surface tension with a water model, Weber and Froude similarity criteria must be satisfied by using a 0.6-scale model [4].

$$We_m = We_p \qquad \text{[Eq. 2.6]}$$

$$\left(\frac{\rho UL}{\sigma}\right)_m = \left(\frac{\rho UL}{\sigma}\right)_p \qquad \text{[Eq. 2.7]}$$

However, other factors related to surface tension, such as multiphase flows (slag-steel-air) interactions and droplet emulsification have to be considered in addition to satisfying We similarity criteria. The incorporation of all these factors to the problem brings about very complex phenomena to be modeled with a water model. Scaled water models of continuous casting molds have successfully represented the molten steel [5]. Although it is important to mention that those models are more reliable when working with very high Reynolds numbers and are less accurate when the flows drop into the laminar regime, such as those zones observed near the bottom of the mold [6]. All these approximations are considering isothermal conditions. For modeling non-isothermal systems, holding constant ratios of heat transfer mechanisms between model and prototype is required. If the temperature changes are taken into account in a continuous casting mold system, the modified Froude Number is important for an accurate match.

$$Fr^{*}{}_{m} = Fr^{*}{}_{p} \qquad \text{[Eq. 2.8]}$$

$$\left(\frac{\rho U^2}{(\rho l-\rho)gL}\right)_m = \left(\frac{\rho U^2}{(\rho l-\rho)gL}\right)_p \qquad \text{[Eq. 2.9]}$$

The modified Froude number represents the ratio of inertial forces to buoyancy forces caused by temperature differences that induces density variations within the liquid steel when casting under superheat conditions. Various methods have been used for characterizing fluid flow in continuous casting molds. The tracer injection method is a powerful tool that provides an insight of the instantaneous velocity fields in aqueous systems by assuming the injected dye (of neutral density) is following closely the flow dynamics of water. The slag phase can be simulated by different types of oil or plastic beads in a water model. Viscosity and density ratios of slag to steel must correspond to that of oil to water so as to model the slag-steel interface. However, this similarity criteria is very difficult to satisfy and so this approach is merely qualitative but can provide a good insight to the interaction between two immiscible liquids with different densities as those systems encountered in continuous casting molds [7]. In addition to these difficulties to model an actual mold process, turbulent flows encountered in molds are transient and highly complex. Therefore, to capture the flow features, a more detailed and sophisticated method consists of using laser techniques to analyze and quantify the transient velocity fields in molds [8-10]. These include Laser Doppler Velocimetry (LDV) and PIV. These non-invasive methods differ from those where a device is positioned in the flow domain, such as hot wire/film anemometer. In the PIV, the system is seeded with neutrally buoyant particles, which are assumed to flow with the mainstream without any relative velocity. As the laser is constantly shooting a beam, the particle position is obtained in two different frames and captured by a charged-coupled device (CCD) which sends the information to the computer, allowing the instantaneous velocity fields to be computed.

2.2 Mathematical modeling

Mathematical modeling is a useful tool to predict, visualize, and analyze, velocity fields. This technique is used to solve and couple different phenomena such as heat transfer, multiphase flows, solidification, etc., that are otherwise far more difficult to analyze in water models. CFD analyses rely on computational power to run numerical algorithms. They can provide a good insight of the fluid flow problem at hand, while substantially reducing costs on experiments and facilities. As the computing power is increasing every day, mathematical modeling has become a very powerful method and an accessible tool for researchers and engineers involved in the steel industry. A common methodology usually found at the interface of any numerical software to tackle a CFD problem, consists of the following steps: i) Defining the domain and geometry of the element to be analyzed with the aid of CAD tools. To assign the number of cells, the fluid properties and proper boundary conditions need to be input. Usually, the accuracy of the solution is better when the number of control volumes is increased (i.e. a finer mesh). ii) The differential equations are discretized into algebraic form and then solved by numerical techniques. iii) Once the solution is found, post-processing tools help in understanding the solution by providing vector plots, colored contours of the property of interest, surface plots, videos, etc. Commercial software is now usually used to model transport phenomena in the continuous casting process. They include the following: CFX, FLOW 3D, ANSYS-FLUENT, ABAQUS, COMSOL, PHOENICS, etc. The motion of steel flows within continuous casting molds are governed by the instantaneous continuity and Navier-Stokes equations. This instantaneous set of partial differential equations can be calculated directly using Direct Numerical Simulation (DNS). By this method, all time and length scales of turbulence are solved, making this approach very computationally demanding. Fortunately, engineers and researchers involved in the continuous casting process are more concerned with time-averaged properties and bulk flows rather than obtaining solutions for the smaller scales. A widely used approach is to average the continuity and N-S equations for incompressible Newtonian Fluids in the 3D domain. The Reynolds Averaged Navier-Stokes (RANS) equations, bring about nine additional turbulent variables named the Reynolds Stresses ($\tau_{ij}=-\rho\overline{v_i v_j}$) that are to be solved, together with the mass conservation and momentum equations. For that purpose, turbulence models are employed so as to provide additional expressions that can incorporate turbulent stresses into the RANS equations, and thereby, model turbulence phenomena using a more simplified set of partial differential equations (PDE's). This is possible by using the Boussinesq approach, which relates Reynolds stresses with mean rates of deformation by the turbulent or eddy viscosity approach.

$$\tau_{ij} = -\rho\overline{v_i v_j} = \mu_t\left(\frac{\partial U_i}{\partial x_j} + \frac{\partial U_j}{\partial x_i}\right) \qquad \text{[Eq. 2.10]}$$

The eddy viscosity μ_t depends on the flow and varies through the domain of interest [11]. Nowadays, the two equation models of turbulence are a reliable approach used in the steel industry since they are economical and can be applied to a wide range of flows, and give reasonable accuracy. In this approach, an additional conservation equation is incorporated to solve the turbulent flow at different length scales. Some of these turbulence models are k-kl, k-ε, k-ω, etc. The most popular two equation turbulence model is the k-ε model and its different variations [12]. The k-ε turbulence model, calculates the turbulent viscosity by adding two transport equations, the conservation of turbulence kinetic energy, k, and the rate of dissipation of turbulence kinetic energy, ε ($\varepsilon = -\frac{dk}{dt}$). The importance of two equation turbulence models reside in the accurate calculation of the bulk flow velocities. However, Reynolds numbers greatly differ near the wall regions where the viscous effects are of much greater relevance than inertial forces. Thus, the k-ε models may lead to wrong predictions of k near the walls [13]. Therefore, instead of solving RANS and turbulence model equations in the laminar sublayer, alternative functions are used. One option is to use the law of the wall, which provides a logarithmic function for the mean turbulent velocity profile near a wall boundary. The law of the wall is expressed as:

$$U^+ = \frac{1}{K}\ln(Ey^+) \qquad \text{[Eq. 2.11]}$$

Furthermore,

$$\frac{\rho U_p k_p^{1/2} C_D^{1/4}}{\tau_w} = \frac{1}{K}\ln(Ey^+) \qquad \text{[Eq. 2.12]}$$

Where,

$$y^+ = \frac{y_p k_p^{1/2} C_D^{1/4}}{\upsilon} \qquad \text{[Eq. 2.13]}$$

This velocity profile connects the wall conditions to the turbulence variables outside the sublayer. A second option for solving near the wall flow is the low Reynolds turbulence model. In this model, the conservation equations are solved all the way to the confining walls. Hence, a higher number of grid points are needed for an accurate calculation of flows near the wall, and this implies more computational time. A limitation of the two equation models, such as the k-ε turbulence model, is that they cannot properly predict anisotropic normal Reynolds Stresses in secondary flows, such as those found in long non-circular ducts. This is because the model assumes isotropy of turbulence. In addition, it also can lead to wrong results when analyzing swirling and highly strained flows [11,14]. D. Hershey et al. [15] studied turbulent flows through bifurcated SEN's on a continuous casting slab system by using the standard k-ε turbulence model with the aid of commercial software for the numerical simulations. The instantaneous velocities were predicted with a hot-wire anemometer located near the ports outlet region in a full scale water model setup. The three-dimensional mathematical model described the fluid flow through the rectangular SEN's ports which consisted of swirling jets leaving the bottom half of the SEN, with a stronger momentum as compared to the recirculations with lower velocities that were found in the upper parts of the SEN ports. The standard k-ε turbulence model under steady-state conditions was found unable to predict the time-dependent fluctuations that were measured by the hot-wire anemometer in the low-velocity regions on the upper part of the discharging ports. However, the bottom part, which consisted of higher velocities, was predicted accurately. Another more accurate approach, but more intensive in terms of computing requirements, is the Large Eddy Simulation (LES) model. In this model, those eddies falling in the large scale range are solved, while the smaller eddies are modeled. The LES model can predict instantaneous flow features, similarly to the DNS model while much less computational power is required. S. Sivaramakrishnan et al. [16], simulated fluid flow in a slab mold using LES models for the numerical calculations and PIV for the measurement of instantaneous velocity fields. The LES model was able to compute high frequency variations in the flows near the top surface. Although double roll flow patterns were observed throughout the mold cavity, asymmetric flows near the lower rolls were observed in both methods, even when a full symmetry of conditions and dimensions was considered. These findings suggest that wrong results may be obtained when considering only one half of the mold by imposing a boundary condition of symmetry to simulate the other half. The interaction between these asymmetric flows can only be examined if a full domain of the mold is considered. According to Q. Yuan et al. [17], the LES model shows superior performance over two-equation turbulence models, such as standard k-ε, k-ω, etc. However, a finer mesh in regions of high gradients of velocity is needed for an accurate representation of transient phenomena. In fact, two-equation turbulence models are reliable if fluid flow under steady state conditions is only of interest. As previously discussed, the Navier-Stokes equations are very complex and difficult to solve analytically, and even numerically, in some of the cases. Therefore, the solution of the PDE's is sought using different numerical techniques. The most common approaches used are the Finite Difference Method (FDM), Finite Element Method (FEM) and the Finite Volume Method (FVM). The formulation of the FDM, consisting of a Taylors' series expansion to approximate the differential equations, provides limitations when complex geometries that require a three dimensional analysis are solved. Conversely, FEM and FVM are integral methods with more geometrical flexibility. The FVM is a widely used method for CFD purposes in which some of its embedded features such as the simplicity on the formulation for unstructured meshes required for complex geometries and the formal integration of the governing equations in each finite control volume (that ensures the conservation of a general flow variable) conform with CFD problems, where several transport equations are solved simultaneously. Commercial CFD software such as FLOW 3D, ANSYS-FLUENT, PHOENICS and Star-CD are based on this numerical approach.

Once the integration of the transport equations is performed, the discretization procedure in the FVM is carried out by the substitution of the PDE's with approximations similar to finite difference methods that transform the differential equations in to more simple set of algebraic equations.

In this research, the commercial software ANSYS-FLUENT was used for the numerical simulations. In this software, the user specifies the number of cells to be used for the calculation. Then the FVM assigns boundaries or faces at the middle point between adjacent nodal points. In this way, each node is surrounded by a control volume, or “cell”. The values of the variables are determined by the application of differencing schemes and stored on the faces and nodes. One of the variables that requires special treatment in problems related to fluid flow of incompressible fluids, such as those encountered in continuous casting molds, is the pressure field. The pressure emerges in each of the momentum equations and is strongly coupled with velocity. However, there is no extra equation available for this variable. Therefore, an iterative method to obtain the solution must be used. Algorithms such as SIMPLE, PISO, SIMPLEC, SIMPLER, etc., are iterative strategies that apply an initial pressure field, which is then used to solve the momentum equations [14]. After that, a pressure correction equation is applied from the continuity equation. The corrected pressure field is used to obtain new values of velocity and pressure fields. The algorithm iterates until the final solution is obtained by reaching the convergence criteria for all variables. The set of algebraic equations is solved by different techniques such as the Tri-Diagonal Matrix Algorithm (TDMA), Incomplete Lower Upper (ILU), Gauss-Siedel, etc.

Although it is well known that commercial software can predict very accurately different fluid flow phenomena, a combination of plant trials and physical experiments are always needed to validate and complement the solutions obtained by the mathematical models. Physical and plant experiments are still the best sources for a more detailed insight of what is happening in the real process. In the following section, the research conducted related to the continuous casting processes is reviewed. The topics reviewed include the defects in continuous casting, fluid flow modeling, and flow control via SEN design in slab, billet and bloom casting, and EMS systems in molds.

2.3 Defects in the continuous casting process

It is well known that the formation of cracks in slabs, billets and blooms, during the continuous casting of steel, is a major problem for the quality of the final product. The cracks may appear in the interior, or at the surface of the solid steel. It is common to find internal cracks in the near corner region, diagonally between opposite corners and at the centerline. On the surface, the cracks may occur in the longitudinal and transverse regions. The different types of cracks can be seen in Figure 2.1.

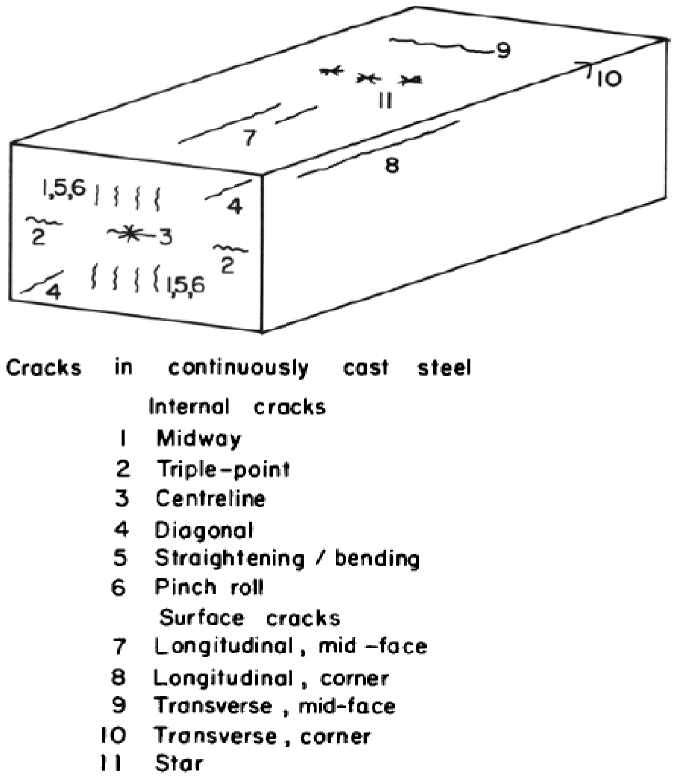

Figure 2.1 Schematic diagram of the different types of cracks found in a cast steel section [18].

The formation and propagation of the cracks are triggered by the rapid cooling of the solid shell, which results in high differences in temperature, as the surface cools down with the aid of water spray systems. The solidifying front always remains at a higher temperature compared to the surface. Variations in the external cooling result in the constant expansion and contraction of the solid shell, generating thermal strains. Other causes that are related to the formation of stresses include the friction between the shell and the oscillating mold, ferrostatic pressure, roll pressure, roll misalignment, and strand straightening operations [18].

Lankford, W. [19] discussed the different sources of stresses in the solidifying shell of the continuous casting process. Once the liquid steel comes into contact with the mold and starts to solidify, the shrinkage of the solidified shell interacts with the ferrostatic pressure of liquid steel. As a consequence, bending moments inflict tensile stresses at the surface and compressive stresses in the solidification front region. It is the transverse force exerted by the ferrostatic pressure that provokes bulging of the solidified skin as the billet, or slab, being formed, descends. In this way, the air gap between the mold and surface of the cast steel is reduced. This force is balanced after the shell comes into contact with the wall of the mold. However, as the cast steel is displaced by gravity forces aided by the oscillating mold, into the roller sections, the forces imposed by the strand may differ from those previously exerted by the mold wall [19]. These force gradients also contribute to the formation of stresses in the solidification front. B. Thomas el al. [20,21] estimated shell shrinkage by using a FEM elastic-viscoplastic thermal stress 1D mathematical model. They found that shell shrinkage depends strongly on the heat flux gradient, which is higher near the meniscus. They proposed to design mold taper according to the heat flux profile and by also considering other important factors such as casting speed, grade of steel and mold length. High casting speeds cause shell thinning, and this induces bulging below the mold exit [22]. The correct mold taper design ensures a proper contact between the solidifying shell, as it shrinks, and mold walls. This promotes a proper heat transfer through the mold cavity. In addition, the oscillating mold wall exerts a friction force on the shell surface where tensile stresses are developed in the skin. The oscillation movement of the mold causes the direction of these stresses to be constantly changing, from tensile to compressive, resulting in a cyclic stress. If the sum of these stresses is high enough, there can be a breakout from the solidifying skin. A sticking-type breakout is usually observed after a sudden increase in temperature (proof that poor lubrication is also present) at the mold walls, followed by a decrease that is less than the initial value of temperature. This type of defect is a common problem found in thin slab casting, since casting speeds are higher [23,24]. Online methods that monitor gradients of temperature in the mold walls have been developed to predict “stickers” [25,26]. During bending and straightening of the strand, axial strains are also induced in the solid shell. The partial and total fracture of the solid shell depends on the different mechanisms described above. These regions with more concentration of stresses and less ductility, together with certain mechanical properties are more likely to develop and propagate cracks.

There are different temperature ranges where the steel exhibits lower strength and ductility. This can also increase the probability of crack formation. In the high temperature zones, about ~ 1340°C, the ductility and strength decrease abruptly. The reason for this is that the inclusion particles that concentrate in the regions between the growing dendrites start freezing, once the temperature is lower than the solidus. These inclusion particles are formed by high levels of sulphur and phosphorus. There are different variables that control hot ductility such as: grain size, precipitation and inclusion content. If the sulphide particles, that precipitate in the free zones along the grain boundaries, are very fine and numerous, they can connect each other better, and as consequence, crack propagation is enhanced [27,28].

The deleterious effects of S and P can be mitigated by elements such as Mn [29]. It has been shown that an increase in Mn satisfactorily decreases the FeS content, and increases MnS content. The Mn raises the solidification temperature of the sulphide in the interdendritic region, so that the liquid sulphides of MnS are solidified in the same range of temperatures as steel [30]. It is also well known that in this range of temperatures, steels with a content of more than 0.2% wt C, are less ductile than a 0.1% wt carbon steel. By increasing the content of C in the steel (beyond 1.5% wt C approximately) the primary phase to solidify is switched from delta-ferrite to austenite. This influences the microsegregation of elements such as S and P when the solidification of carbon steel is taking place in the mold [31]. In the intermediate temperature zone from 800 to 1200 °C, the ductility is strongly related to the Mn/S ratio. Steels with a higher ratio of Mn/S are not embrittled. This zone is less responsible for crack formation than the higher temperature zone. The lower temperature zone (from 700 to 900 °C) is commonly associated with Al solubility, and it has effects only on the formation of surface and subsurface cracks [18]. The different internal cracks found in the continuous casting process are: midway cracks, triple point cracks, centerline cracks, diagonal cracks, bending/straightening cracks and pinch roll cracks. Midway cracks are formed by excessive cooling in the mold and the subsequent reheating. The surface is subjected to tensile stress as it expands when reheated, thus forming a crack perpendicular to the surface. This crack can be inhibited if the reheating of the surface is decreased or if the ductility and strength are increased in the high temperature zone. Local reductions of cooling should be avoided. Triple point cracks appear more often in slab casting. They are oriented perpendicular to the narrow face, within the region where the three solidification fronts meet. The cracks can be found between 3 to 10 cms. from the surface, inside the slab. These cracks are formed by bulging of the wide faces combined with a weak shell. This defect can be avoided if the rolls are adjusted properly. Center line cracks develop in the center position of a cast. Their formation is strongly influenced by spray water intensity, roll alignment and casting speed. Thus, bulging of the cast has to be prevented. Increasing the spray cooling and reducing the casting speed are measures that can be taken to reduce the manifestation of this kind of cracks. The diagonal cracks are more commonly seen in billets, and they are associated with rhomboidity. This crack arises when two adjacent faces are cooled faster than the others. To avoid these types of cracks, equal cooling and good alignment of the roller cages must be attained. Other types of cracks are formed when a straightening or bending operation takes place while the core of the cast is still in the liquid state. The casting conditions have to be considered to avoid this cracks formation. The pinch roll cracks are generated when a high pressure is exerted from the rolls, while the center is still liquid, or near the solidus temperature. These cracks can be avoided by adjusting the rolls properly. Surface cracks are more problematic than the internal cracks because they oxidize and cannot be treated during rolling. The surface cracks include the following: longitudinal midface and corner cracks, transverse midface and corner cracks, and star cracks. It has been shown that the composition of the steel plays an important role in the formation of longitudinal midface cracks. Steel with carbon levels of around 0.12 % and a low ratio of Mn/S can contribute to the crack formation. Some elements such as Nb, have a detrimental effect and additions as low as 0.01 % can increase the cracking development. There are other factors that can increase the size of the cracks such as casting velocity, casting with a high superheat temperature, alignment between mold and rolls, and over-cooling by spray systems. Non-uniform cooling in the mold can develop low ductility hot spots, with a temperature of around 1340°C, which can promote crack formation. The non-uniform cooling can be caused by uneven distribution and feeding of mold powder, local air gaps, or irregular growth of the shell caused by a strong impact of liquid metal flow onto the shell. The formation of longitudinal corner types of cracks are highly influenced by tapping, using a high tundish working temperature, a high casting speed, and steel containing 0.17 to 0.25 pct. C, S > 0.035, P > 0.025 pct. Reverse tapping together with the thermal shrinkage, increase the distance between the copper mold walls and steel shell surface. These two conditions decrease the heat extraction. In such case, the surface reheats reaching the low ductility temperature range, in which the cracks are more susceptible to develop [32].

Transverse, midface and corner cracks appear at the base of the oscillation marks and are developed during the straightening of strand. The steel composition plays an important role in the formation of these cracks. Steel containing vanadium, aluminum, niobium are more prone to develop cracks. By lowering the cooling rates, more uniform temperatures are achieved in the surface. In the billet casting, these cracks are formed if high levels of S and P are present. Adequate feeding of powder and mold lubrication has to be considered too. Star cracks are formed with the scraping of copper from the mold walls. The formation of this type of crack can be reduced by plating the mold walls with chromium.

Many researchers have developed models to study crack formation. Sorimachi K. and Brimacombe [33] developed the first finite element thermal stress computational model of solidification. They showed that the surface of the steel cast would be reheated in those zones where the sprays were either inexistent or insufficient. A distribution of stresses of the solidifying shell was obtained as a function of temperature. A transient, thermal-elastic-visco-plastic finite element model was applied by Chunsheng Li et B. Thomas [34,35], using COND2. The stress, strain, temperature, and deformation were simulated in a 2D section of a square billet. They showed that by increasing the casting velocity, the shell becomes thinner and that bulging increases below the mold. The corner of the billets cooled faster, causing an increased level of tensile stresses.

J.E. Kelly et al. [36] developed a 2D mathematical model to simulate the thermo-mechanical behavior of the shell in a continuous casting round billet. The effects of the steel carbon content, mold taper in stress, displacement, and thermal fields, were studied. They found that with a high taper, the heat flux increases towards the last part of the mold, while with a low taper, heat fluxes decrease slowly. The steels with approximately 0.1% wt C were more susceptible to develop longitudinal cracks, in comparison to others. The convective terms in the momentum equation were not considered in this model. Chun Xiao-bin Li et al.[37] also investigated the formation of cracks in steel. They introduced a 3D coupled thermomechanical model to calculate temperature, stress and strain distributions in blooms during soft reduction, using the Finite Element Method based on the commercial software MSC-MARC. They proposed that a decrease in the soft reduction can lower the stress below the critical values, and thereby reduce the formation of internal cracks. An optimum soft reduction process can be developed for the real production.

2.3.1 Defects related to fluid flow in continuous casting

In the final stage of the continuous casting process, prior to complete solidification, the quality of the final product depends highly on appropriate fluid flow controls within the continuous casting molds. There are several conditions to be accomplished in order to improve the quality of steel. These are: minimize the exposure of the liquid steel to the air, avoid the entrainment of mold powder, achieve a fluid flow pattern inside the mold that can promote a uniform temperature distribution and solidification, and reduce surface-level fluctuations. The fluid flow in the mold is controlled by SEN designs and operational parameters. The nozzle design comprises bore size, ports sizes and angles, port shape (ellipse, round, square), number of ports, nozzle thickness and bottom design. The operational parameters involve the injection of argon gas, electromagnetic stirring practices, nozzle submergence depth and casting velocity. Other fixed parameters are sliding gate, stopper rod, strand width and thickness. It is the unsteady nature of the fluid flow in the mold that makes it very difficult to control all these parameters together. The appropriate design and operation is of paramount importance in order to achieve a high quality steel casting [38]. The details of the mold can be seen in Figure 2.2.

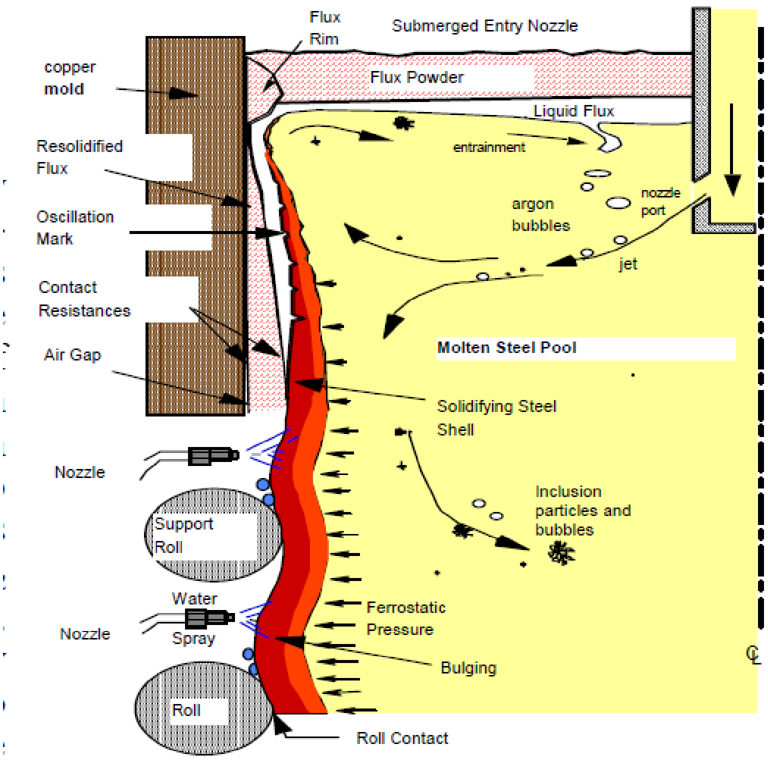

Figure 2.2 Schematic of the complex phenomena occurring inside the mold [39].

As the liquid steel is transported through the SEN into the mold cavity, argon gas is sometimes injected to prevent nozzle clogging with solid inclusions. The influence of a clogged nozzle on the entrapment of inclusions was studied by L. Zhang et al. [40]. This research was conducted with the aid of the commercial software FLUENT for a 3D single-phase turbulent flow in a continuous casting slab mold. The trajectory of each inclusion particle was computed by using the Lagrangian-Lagrangian approach. The governing equation considers the balance between drag and buoyancy forces.

$$\frac{du_{pi}}{dt} = \frac{18\mu}{\rho_p d_p^2}\frac{C_D Re_p}{24}\left(u_i - u_{pi}\right) + \frac{\rho_p - \rho}{\rho}\ g_i + \frac{1}{2}\frac{\rho}{\rho_p}\frac{d}{d_t}\left(u_i - u_{pi}\right) + \frac{\rho}{\rho_p}u_i\frac{du_i}{dx_i} \qquad \text{[Eq. 2.14]}$$

The drag coefficient is given by:

$$C_D = \frac{24}{Re_p}\left(1 + 0.186{Re_p}^{0.6529}\right) \qquad \text{[Eq. 2.15]}$$

Clogging on one port of a bifurcated nozzle develops asymmetric flows throughout the mold. It was observed that the non-clogged side accumulated a higher number of particles than the clogged side, given that a higher number of particles were transported through the non-clogged port. Accordingly, the authors observed a lower quality on the non-clogged side of the mold. It was also found that inclusions larger than 200 µm are more prone to be entrained when casting with a clogged nozzle than is the case of a SEN with no clogging at all. The argon injection has been also successfully applied for the removal of inclusions [41,42]. However, the inert gas bubbles provide buoyancy forces which may alter the fluid motion of the incoming jet. C. Pfeiler et al. [43] used a Eulerian-Lagrangian approach to model 3D turbulent flow in a continuous casting slab. In this research, liquid steel was considered as the continuous phase and gas bubbles as the dispersed phase. They found that large bubbles of argon disturbed the downward melt velocity in the center of the SEN. This disturbance to the jet provoked the dispersion of bubbles to a greater extent in the melt pool as compared to an operation without gas injection. A 0.6 scaled water model study was conducted by L. Zhang et al. [44] for a slab casting operation. A combination of high flow rate of gas, shallow SEN depth and low casting speed promoted the formation of a single roll flow pattern through the mold cavity. A double roll flow pattern, which is usually more stable, was maintained by keeping the gas flow rate below critical levels. The transient behavior of fluid flow can lead to bubble entrainment in the solidified regions [4]. The inclusions brought from the previous stages of steelmaking, together with the injected bubbles, can get entrapped into the solidifying shell causing slivers, blisters and other defects [45]. The slivers are created by alumina clusters and mold slag. The blowhole defects (pencil pipe blister) are formed by argon bubbles in combination with slag entrainment. These types of defect are seen as surface defects after the rolling process [46].

Superheat control in continuous casting molds is very important to attain a high quality steel product. Deficient superheat removal can lead to breakouts if temperatures remain too high and a long air gap between mold walls and surface has developed. The high temperature impinging jets on mold faces can cause thinning of the solidified shell. Santillana B. et al. [47] related shell thickness of thin slab samples that suffered from breakouts with thermocouple readings of temperature that monitored the mold walls. The shell thickness was measured by a 3D digitizer (ATOS) and an optical coordinate measuring machine (TRITOP), shown in Figure 2.3.

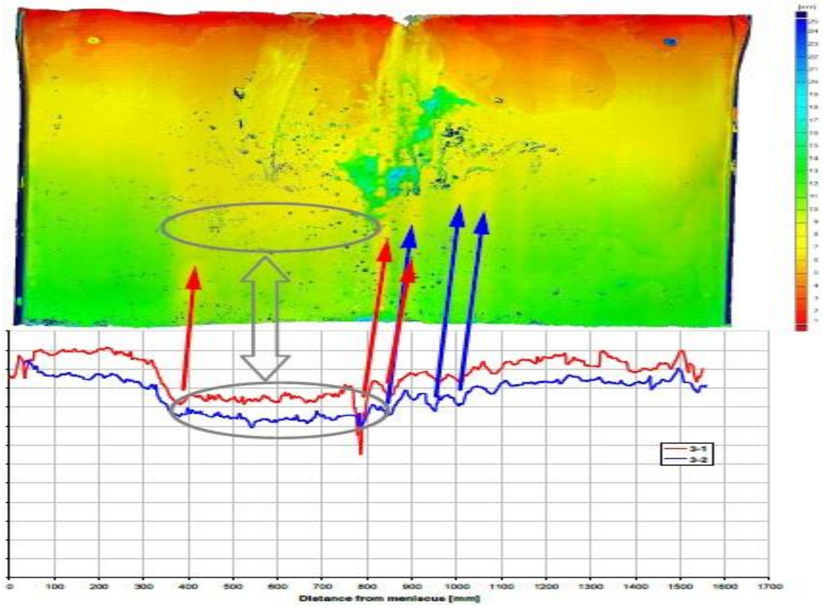

Figure 2.3 Shell thickness contours and along horizontal lines [47].

They reported that regions with thinner shell registered lower temperatures, while a thicker shell showed the opposite. Therefore, the authors attributed the shell thinning and breakouts to a lack of heat extraction caused by the development of a thin layer of air. However, the thickness of the air gap was not reported. The superheat dissipation and the solidifying shell temperature distribution on continuous casting molds are modeled by a turbulent convection diffusion equation. This transport equation is written as follows:

$$\frac{\partial}{\partial t}(\rho H) + \frac{\partial}{\partial x_i}(\rho u_i H) = \frac{\partial}{\partial x_i}\left(k_{eff}\right)\frac{\partial T}{\partial x_i} + \mathrm{Q} \qquad \text{[Eq. 2.16]}$$

Saul G. et al. [48] predicted temperature distribution and shell growth in a continuous casting slab mold by using the k-ε turbulence model. The Volume of Fluid (VOF) technique was used to solve the multiphase system air-slag-steel and the temperature distribution was computed by the porosity-enthalpy method. The mathematical model predicted a more irregular shell growth along the inner radius wall of the mold curvature as compared to the outer radius wall. The authors attributed the irregular growth to the high temperature convective steel flows impinging on the mold walls. If the superheat temperature and liquid metal velocities near the surface are too low, associated oscillation marks are formed, and the meniscus freezes to form "hooks" which can entrap inclusions in the solidifying regions. The superheat influences the growth of equi-axed grains, and can lead to centerline segregation [49]. The fluid flow along the mold walls can disturb the upper level, and create non-uniform heat fluxes at the meniscus and longitudinal cracks. High turbulence near the surface can produce unstable solidification at the meniscus, surface depressions, deep oscillations marks, surface cracks and slag entrapment. The oscillation marks are formed by pressure variations generated in the molten flux channel. The hooks are formed during negative strip, when the mold oscillates downwards at a slightly faster velocity than the casting velocity. During the upstroke (positive strip), liquid steel overflows the hook and solidifies right after filling the channel, thereby creating the oscillation marks. The formation mechanism of oscillation marks takes place with rigid or semi-rigid skins at the meniscus. If the skin is rigid, the hook is formed. Conversely, if the hook is semi-rigid, a deep oscillation as a surface depression is formed [50].

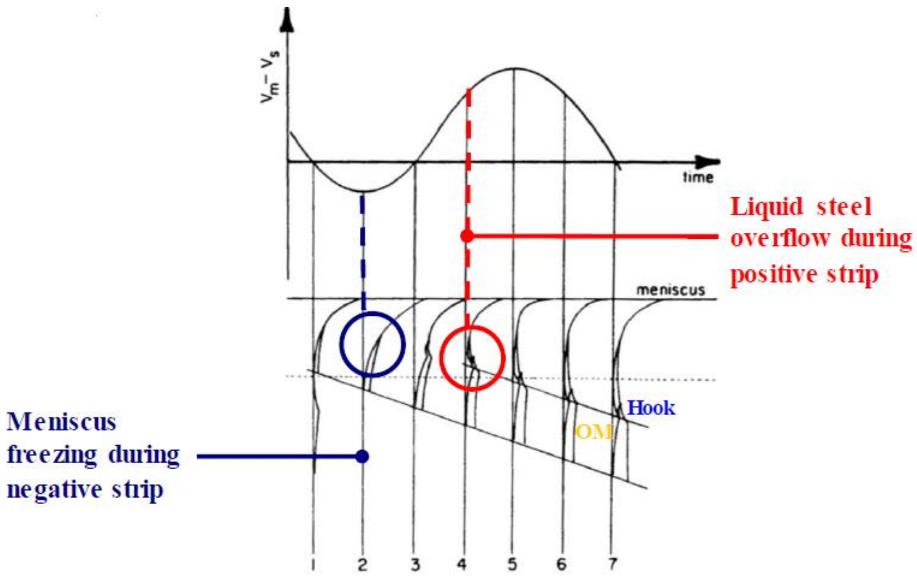

Figure 2.4 Scheme of oscillation marks mechanism showing that the meniscus freezes during negative strip and overflows during positive strip [51].

2.4 Mold powders in continuous casting

In the continuous casting process of slabs, blooms and billets, mold powders with different compositions are fed over the liquid steel surface by automatic feeders.

The main components of mold powders are the following: CaO, SiO_2, MgO, Al_2O_3, Na_2O, Li_2O, Na_2O, CaF_2 and MnO. Carbon particles in the form of coke breeze are added to control the melting rate. They are employed to accomplish the following tasks to: protect steel from re-oxidation, avoid large heat losses from the surface, absorb inclusions into the liquid slag, and to ensure a good lubrication between the steel strand and the oscillating mold.

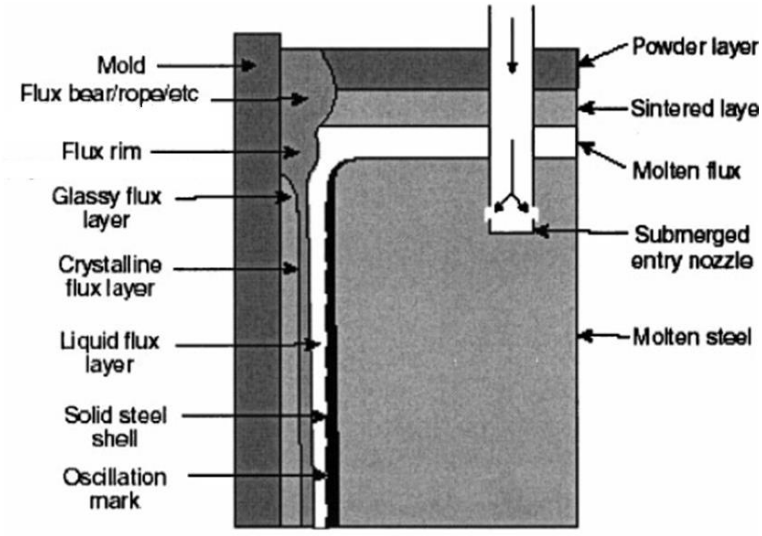

Figure 2.5 Scheme representing the different layers of liquid and solid slag [52].

As the synthetic powder increases in temperature, carbon particles that float up to the top surface are released and react with the oxides found in the mold powder. This reaction forms a reducing atmosphere of CO(g) that protects liquid steel from re-oxidation. These oxide components form a sintered slag layer that melts and infiltrates between the solidifying steel shell and mold walls. One portion of the liquid slag layer solidifies against the mold walls cooled by water and forms a glassy, solid slag film which subsequently crystallizes near the high temperature regions. The remaining liquid slag acts as a lubricant to the solidifying steel shell. A slag rim is usually formed near the metal/slag interface that reduces the space between the shell and mold walls. This lack of space hampers the filtering of liquid slag causing an inadequate lubrication [53]. The different slag layers are observed in Figure 2.5. The physical properties of mold powders can help in preventing a number of different defects that are found in the final steel product. Viscosity plays an important role since it determines the powder consumption and proper lubrication. The solid layer of slag and hence horizontal heat transfer, are affected by the breaking temperature or $T_{br.}$ The breaking temperature determines the thickness of the solid and liquid layers of slag. The interfacial tension is also an important factor, since higher values minimize slag entrainment and the depth of oscillation marks [54]. Previous studies have demonstrated the benefits of casting steel with the appropriate mold powder compared with the opencast practices using oil as lubricant [55,56].

2.4.1 Mold powder entrainment mechanisms

The mold powder is a better lubricant that reduces the friction between mold walls and the solidifying shell, and also allows for lower superheat practices [57]. However, the unsteady nature of convective steel flows encountered near the meniscus region can entrain mold powder, forming non-metallic inclusions that decrease the quality of the cast steel. A proper design and selection of a mold flux can reduce MPE and other defects. The properties of mold powders have been studied in the past through physical modeling. In this approach, the slag phase is usually substituted by oil, while steel is simulated by water. It has been reported on these studies, that an increase of; oil or slag viscosity, density difference and interfacial tension between oil-water or slag-steel systems, will increase critical velocities and therefore reduce MPE incidence [58]. J. Savolainen et al. [59] studied emulsification of slag by using a water model. It was found that the increase in oil viscosity, interfacial tension, density difference and oil layer thickness increased the critical fluid flow velocity magnitude required for oil emulsification. They concluded that emulsification cannot be fully described by the Capillary and Weber numbers given that they do not account for all the variables that interact together. The chemical reactions that occur at the steel-slag interface lower the interfacial tension and promote slag entrainment [60]. The mechanisms leading to MPE found in the literature can be divided into nine different categories. Those are: top surface level fluctuations, meniscus freezing, vortex formation, shear-layer instability, upward flow impinging upon the top surface, argon bubble interactions, slag crawling down the SEN, instability of the top-surface standing wave, and top surface balding. Only the main MPE mechanisms pertaining to the current research are discussed in the following section. A detailed description of all existing mechanisms can be found elsewhere [61,62]. Transient fluid flow patterns throughout molds cause large level fluctuations. These meniscus fluctuations are enhanced when higher casting speeds and shallow SEN immersion depths are used. If the dendritic interface is exposed to liquid slag, this would cause MPE as shown in Figure 2.6.

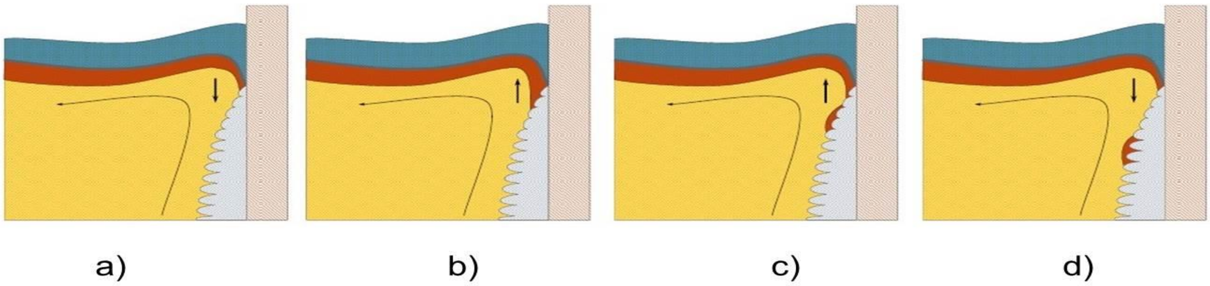

Figure 2.6 Mold powder entrainment by meniscus level fluctuations [63]. a) Start of level fluctuation, b) Slag-shell contact, c) Level rise and entrained slag, d) End of level fluctuation.

The unsteady nature of the upper single roll flow that surrounds the SEN body creates asymmetric flows resulting in the periodic formation of vortexes in the wake of the SEN as observed in Figure 2.7a. The vortexes of slag formed on both sides of the nozzle can get in contact with the dendritic interface or in a worse case, being strong enough as to develop a long funnel from which the tip can detach when it collides with the discharging jets, thereby, propitiating the transport of slag droplets to all the volume of steel in the mold, as shown in Figure 2.7b.

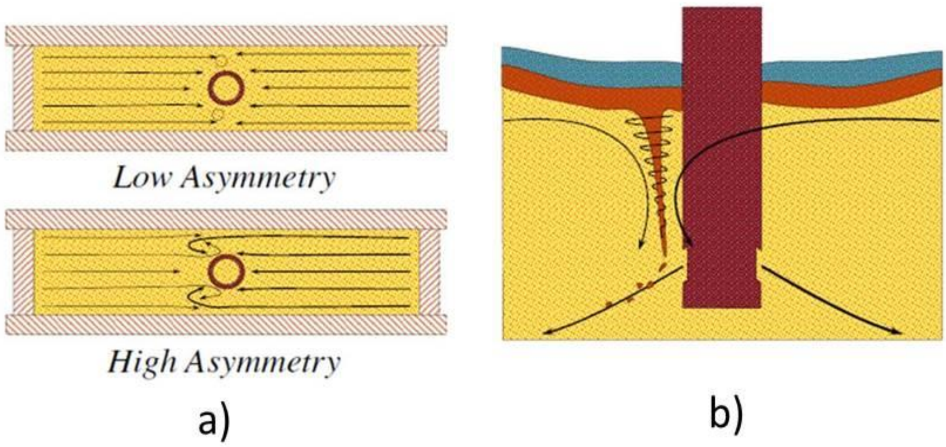

Figure 2.7 Mold powder entrainment by von Kármán vortex formation [63] a) Vortexing from asymmetric flows, b) Entrainment by a deep vortex.

The upwardly directed flow impinging upon the top surface is another mechanism for slag entrainment. Usually found in a double roll flow pattern, it causes shear layer instabilities that can drag or cut liquid slag droplets as shown in Figure 2.8. The critical velocities for this MPE mechanism, ranges from V_{cr} = 0.26 m/s to 0.38 m/s, as reported by different authors [64,65].

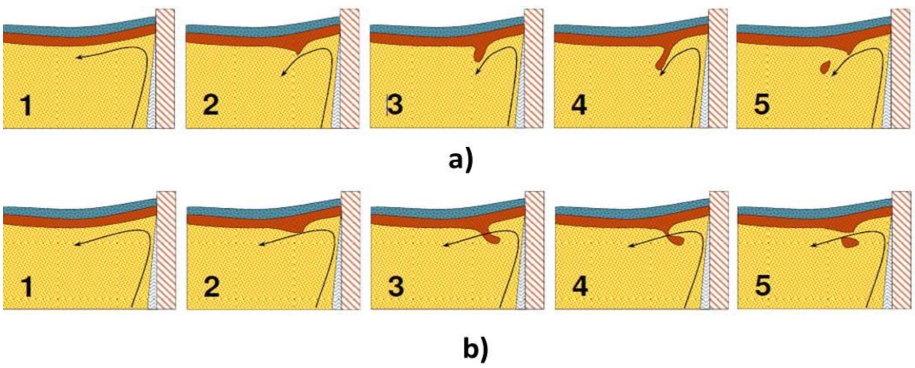

Figure 2.8 Mold powder entrainment by upward flow impinging upon the top surface. a) Sequence followed for entrainment by dragging mode [63]. b) Sequence followed for entrainment by the “cutting mode”.

Top surface balding occurs when strong upper flows distort the level surface and expose the liquid steel to the sintered and solid powder layers, or in a worse case, to the atmosphere as shown in Figure 2.9.

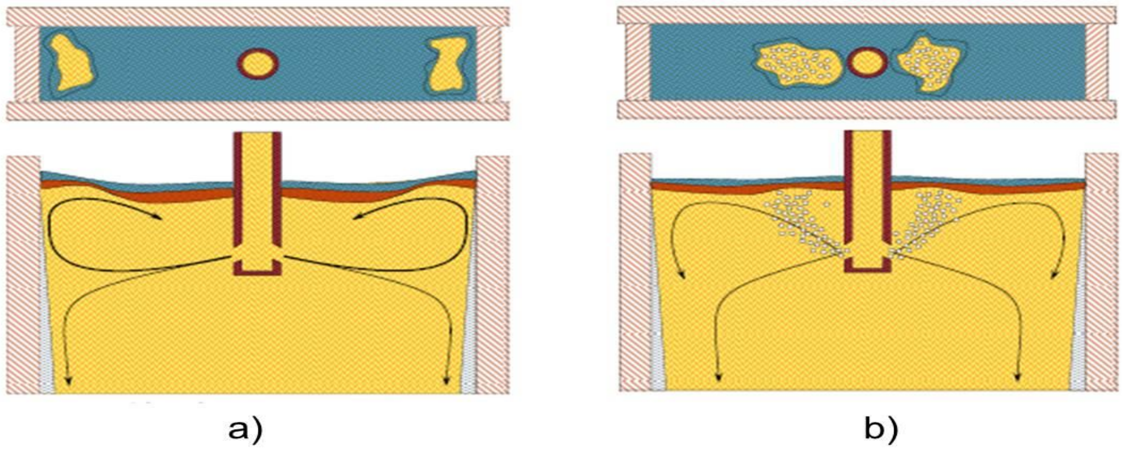

Figure 2.9 Mold powder entrainment by top surface balding. a) Balding by excessive impingement in the narrow faces [63]. b) Balding by excessive argon flow rate.

J. Sengupta et al. [66] studied the effect of liquid level fluctuations and thermal distortion on the solidifying shell for different grades of steel including; ULC steels (%C<0.01%), peritectic steels (0.09-0.17%C) and low carbon steels (%C<0.3%). The 2-D mathematical model solves the energy equation and incorporates latent heat through spatial average of the enthalpy and temperature gradients. The governing equations for the mechanical equilibrium are obtained from the interpolation of thermal loads by first solving the temperature distribution. Although level fluctuations observed in a well-controlled casting operation are less than 10 mm, in this mathematical simulation, a level drop of 16 mm with duration of 0.4s was considered. During this time, the inner side of the shell is exposed to the liquid slag. The heat is extracted faster as the shell is no longer in contact with the hot liquid steel. This extra heat extraction caused peritectic steels to suffer from a higher shrinkage as compared to ULC steels. The transformation from delta-ferrite to austenite in the peritectic steels induces an extra shrinking that causes deeper surface depressions. The larger mushy zone found in low carbon steels causes a less pronounced shrinkage than that of the previous steel grades mentioned. A study of solid slag rim's influence on slag infiltration was conducted by Claudio O. et al. [67]. A 2D mathematical model of a multiphase system, consisting of liquid steel, slag and air, including a solid slag rim, was employed for this research. The governing equations were solved with the aid of the commercial software FLUENT in which the Volume of Fluid model was used to track the shape of the interfaces. The calculations were performed for two mold oscillation cycles. It was found that during PST, the liquid slag is pulled up, opposite to the casting direction, causing negative slag consumption. The positive liquid slag consumption starts just before NST when molten metal overflows the top edge of the solid shell. The reduced space between solid shell and slag rim while the mold is moving downward prevents the absolute infiltration of overflowed slag into the gap. The surplus of slag is therefore pushed into the liquid steel pool in an opposite direction to the meniscus surface. The sequence of this process is depicted in Figure 2.10.

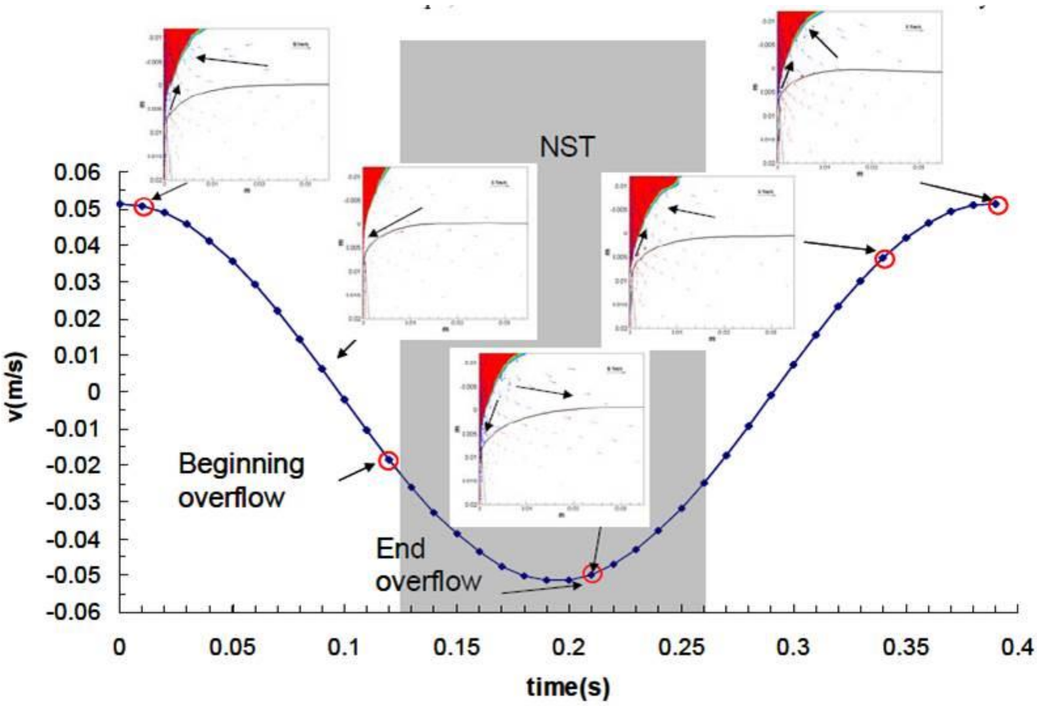

Figure 2.10 Scheme showing the evolution of the interface during one oscillation cycle. The red area represents the slag rim [67].

Different fluid flow phenomena that could act together, such as, a more distorted slag rim, level fluctuations, mold oscillations and incoming transient fluid flow of liquid steel, could expose the solidifying shell to larger volumes of slag. These combined variables could give rise to mold powder entrainment. The interaction of these different factors is an area that needs further exploration. However, it was not considered by the authors in this research. B. Li et al. [68] conducted water modeling experiments to observe the vortex formation that causes slag entrainment in a slab caster. A video was recorded where the flow patterns were observed by injecting black sesame seeds into the water. They found that vortex flows were generated near the SEN discharge region. In their numerical simulation, it was observed that the magnitude of the vortexes increased when using higher casting speeds. The authors suggested the use of Electromagnetic forces and argon injection practices in order to suppress the vortex formation.

2.5 SEN design in continuous casting molds

The effects such as jet impingement and meniscus stagnation, that are caused by the fluid flowing into a CC mold, have to be considered when designing an appropriate SEN for delivering liquid steel into the mold cavity. Meniscus stagnation is caused by low levels of fluctuation at the steel/slag interface. If the jet is mainly directed towards the axial direction, and driven by gravity forces, such as flows encountered in a single port SEN, the liquid steel has less motion at the surface, leading to a temperature loss in the meniscus region due to the decrease of convective flows that enhance heat transfer from liquid steel to slag during superheat operations. This can cause inadequate melting of the powder, which can lower slag lubrication and promote surface defects. Conversely, if the entry jet has a high level of superheat, and impinges strongly on the solidifying steel shell, such as those seen in multiple-ports or bifurcated SEN's, then, together with a low heat extraction, these can cause breakouts as the shell shrinks and an air gap is developed between the liquid steel and mold walls [69].

Many efforts have been carried out to design proper SEN's that can deliver a uniform fluid flow in the mold cavity so as to improve liquid steel cleanliness. As mentioned in the previous sections, port angle, nozzle wall thickness, number of ports and port shape are very important parameters to control the jet or jets entering the mold. An appropriate size and number of ports has to be selected with the aid of physical and mathematical modeling. Oversized ports are used to increase tolerance of inclusions buildup before creating axisymmetric flows. However, the direction of the jet cannot be controlled as expected and stagnant zones in the upper part of the nozzle ports may accumulate inclusions leading to nozzle clogging [70]. This problem can be solved with a decrease of the port area in relation to the bore area, and by increasing the nozzle wall thickness. This is so, since by changing these two parameters, it has been observed that the angle of the nozzle ports has a larger influence on the direction of the discharged jet [71-73]. By increasing the number of ports, the jet momentum is decreased and directed in different directions within the mold cavity. The addition of an extra port in the bottom of the nozzle may be beneficial to reduce nozzle clogging and to improve the stability near the surface level. Other attempts to control fluid flow in molds with a single port nozzle has been carried out by Yokoya et al.[74,75] by placing a swirl blade in the upper part of a diverging SEN, so as to develop swirling motions in a round billet mold (Figure 2.11). They measured the tangential, radial and axial velocities by a using laser doppler velocimeter (LDV) fixed at different positions.

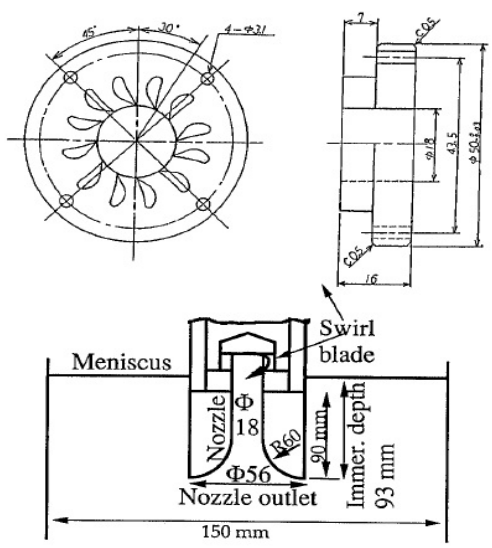

Figure 2.11 Scheme of the water model setup, including immersion depth, nozzle, nozzle outlet, swirl blade and meniscus.

They found that a uniform pattern of fluid flow can be attained within a short distance from the SEN outlet. Heat and mass transfer was enhanced in comparison with conventional SEN. The swirling motion was shown to greatly influence the dissipation of superheat and create a more uniform temperature distribution. The swirling motion creates a bubble curtain through all the jet discharge area that would help to remove inclusions during Ar injection practices. The half vertical angle of the bubble curtain tends to increase by increasing swirling motion [76].

The swirling flow combined with a gradually diverging nozzle was shown to have a positive effect on the bulk flow, by turning the flow outward without the need for placing an opposing face at the end of the nozzle. The velocity at the outlet can be reduced and more stable flow patterns were observed in a slab mold [77]. A considerable stable bulk mold flow was obtained with a higher throughput with the diverging nozzle compared to the two ports nozzle case [78]. Swirling flows were also shown to have positive effects in the Uphill Teeming Process[79] [80].

The effect of a swirling flow in square and circular billet molds for the continuous casting process of steel was studied by S. Yokoya et al. [81]. The two nozzles shown in Figure 2.12 were compared by performing numerical simulations with the commercial software FLUENT and water modeling for the measurement of instantaneous velocities with a Laser Doppler Velocimetry Device (LDV).

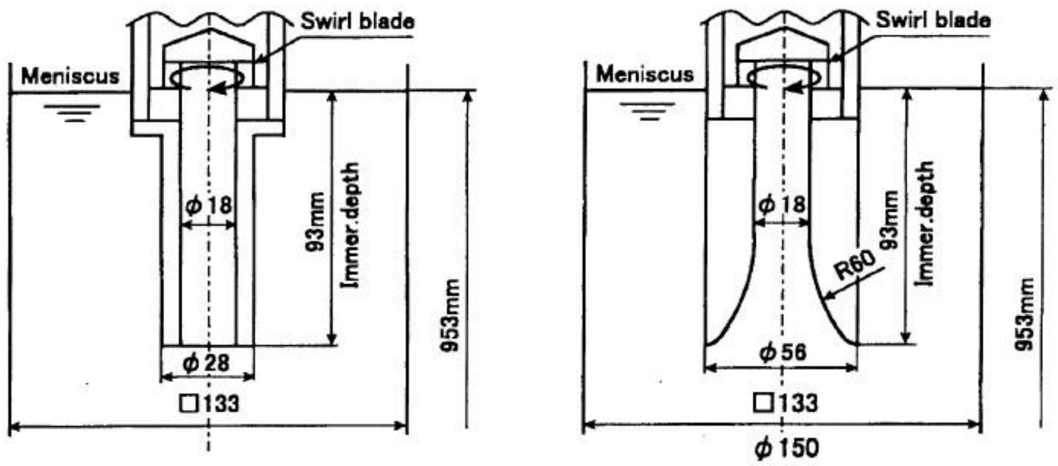

Figure 2.12 Scheme showing the straight and divergent nozzles.

They found that by applying a swirling motion, very different flow patterns are developed in the mold. The velocity gradients are less steep in the divergent nozzle compared to the straight nozzle. Higher temperatures are also observed near the meniscus area in this case. This would enhance the melting of the slag layer and improve lubrication of the mold walls. Heat and mass transfer are more active than in the straight nozzle case, and superior superheat dissipation was also observed.

S. Kholmatov et al. [82] investigated the effect of different divergent angles between 0 and 160° on the flow field and temperature distributions. The swirl flow was created with a swirl blade in the SEN for a square continuous casting billet mold. They found that a more uniform velocity and a better temperature distribution was attained with the divergent angles of 100° or greater, since the upper recirculations were then created near the nozzle area. Higher temperature profiles were found near the meniscus area.

A comparison of two straight nozzles at different heights and their influence on the quality of a square billet was studied by E. Torres et al. [83]. The experiments were carried out in a full scale water model, placing a layer of oil to simulate flux entrainment. The two SEN's had the same inner, but different outer, diameters. They found that the complex interaction of turbulent streams, leading to transient flows near the meniscus region, was the main reason that caused flux entrainment in the actual caster. The sudden changes in the surface were monitored by level sensors identifying sporadic spikes that disturbed the surface and were responsible for oil entrainment in the water model. These spikes were not observed in the mathematical simulations using the Volume of Fluid (VOF) model. The energy of the recirculatory flows increased as the distance from the mold face to the SEN wall decreased.

Three different SEN designs, as shown in Figure 2.13, were mathematically tested in a bloom caster by H. Sun et al. [84] in terms of fluid flow, temperature distribution, and solidification.

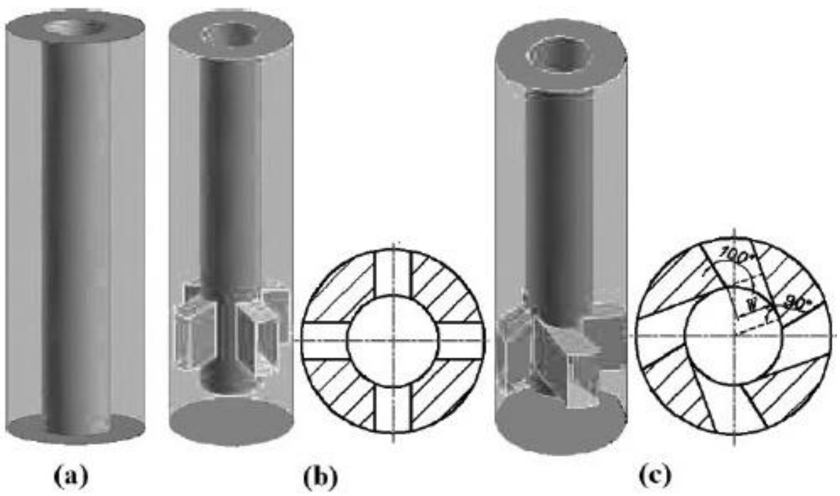

Figure 2.13 Scheme showing the three SEN designs. a) A-type SEN b) B-type SEN c) C-type SEN.

The C-type SEN was shown to have a superior performance over the other two designs. The simulation results showed that the temperature near the free surface can be increased by 2.6 K to 4.4 K as compared with the other two designs. This will improve the dissipation of superheat. The shell thinning caused by the impinging jets coming from the ports was decreased by the C-type SEN as compared with the B-type. The A-type SEN preserved constant the thickness of the growing shell better since no flow collides directly with the mold walls. Unfortunately, the C-type SEN still collides strongly on the mold walls, endangering uniform growth of the steel shell. A similar concept of a multiport nozzle has been proposed by C. Capurro et al. [85], as observed in Figure 2.14. The plant trials and mathematical models that were conducted to study the inclusions distribution in round bars with diameters of 310 mm, demonstrated that a lower density of inclusions with large sizes were found in bars cast with the multiport nozzle than that of a perfectly straight nozzle.

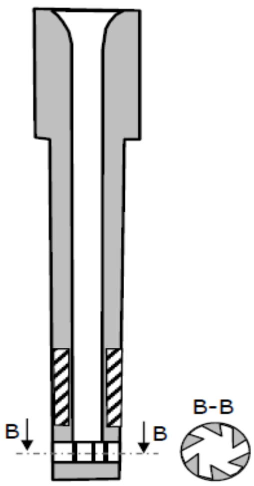

Figure 2.14 Scheme of the six-ported nozzle.

However, the high number of ports in this nozzle obliges the liquid metal to flow through small transverse areas and increase the magnitude of velocity. This could erode the shell in round molds with smaller volumes. In addition, the occasional nozzle clogging could further reduce the discharging area and cause an uneven flow rate distribution among the discharging ports.

2.6 Electromagnetic stirring practices in molds

In the final stage of the continuous casting process, electromagnetic stirrers (EMS) are commonly used to improve the quality of the solidified steel. There are three different types of EMS. The first, is the mold EMS (M-EMS), that is positioned around the mold, and is used to improve quality problems such as internal cracks, columnar structure, center porosities, V-segregations, centerline segregation, surface slag, pinholes, blowholes, subsurface slag and breakouts. The second is the Strand EMS (S-EMS), which can be found around the strand in the cooling chamber, and is used to improve mainly segregation and the columnar structure. The third one is the Final EMS (F-EMS), that is located in the final stages of solidification, and is mainly used to reduce centerline segregation and center porosities[69].

The Electromagnetic stirring phenomena is described by the Maxwell equations. These can be written as follows:

Ampere's Law $$\nabla \times \vec{\mathrm{H}} = \overrightarrow{\mathrm{J_C}} + \frac{\partial \vec{\mathrm{D}}}{\partial \mathrm{t}}$$ [Eq. 2.17]

Faraday's Law $$\nabla \times \vec{\mathrm{E}} = -\frac{\partial \vec{\mathrm{B}}}{\partial \mathrm{t}}$$ [Eq. 2.18]

Gauss's Law $$\nabla \cdot \vec{D} = \rho$$ [Eq. 2.19]

non-existence of monopole $$\nabla \cdot \vec{B} = 0$$ [Eq. 2.20]

In the free space case, where there are no charges and conduction currents applied, $(\rho = 0 \text{ and } \mathrm{Jc} = 0)$, equations 2.17 and 2.18 show that E and H cannot exist independently. If $\frac{\partial \vec{E}}{\partial t} \neq 0$, then $\vec{D} = \mathcal{E}\frac{\partial \vec{E}}{\partial t}$, has a value different than zero. As a consequence, $\nabla \times \vec{H}$ is nonzero so that an H must exist. Similarly, if we consider first that H is changing in time, then E must be also varying [86].

In non-relativistic magnetohydrodynamics (MHD) flows, Ohm's takes the form:

$$\vec{J} = k(\vec{E} + \vec{v} \times \vec{B}) \qquad \text{[Eq. 2.21]}$$

By taking the curl of equation 2.21 and substituting with 2.18 we have:

$$\frac{\partial \vec{B}}{\partial t} = \nabla \times (\vec{v} \times \vec{B}) - \nabla \times (\eta \vec{J}) \qquad \text{[Eq. 2.22]}$$

The differential form of Ampere's Law in free space can be written as:

$$\vec{J} = \frac{1}{\mu_o} \nabla \times \vec{B} \qquad \text{[Eq. 2.23]}$$

Equating 2.23 with 2.22 we can obtain the induction equation which describes the temporal evolution of the magnetic field:

$$\frac{\partial \vec{B}}{\partial t} = \nabla \times (\vec{v} \times \vec{B}) - \frac{1}{\mu_o} \nabla \times (\eta \nabla \times \vec{B}) \qquad \text{[Eq. 2.24]}$$

To model fluid flow in molds with the effect of electromagnetic forces, the external applied magnetic field $\overrightarrow{B_o}$ must be known. This variable, imposed by the EMS coils, can be estimated with a magnetometer. Then $\vec{B} = \overrightarrow{B_o} + \vec{b}$, where $\vec{b}$, represents the induced magnetic field. Since $\overrightarrow{B_o}$ is known, only $\vec{b}$ is calculated from equation 2.24. This is the magnetic induction method. In here, the Lorentz force is:

$$\vec{F} = \vec{J} \times \vec{B} \qquad \text{[Eq. 2.25]}$$

If the Magnetic Reynolds Number, $R_m = vL(\mu_o k) < 1$, $\vec{b}$ is orders of magnitude lower than the applied $\overrightarrow{B_o}$ and can be neglected. In this case the electric potential method can be applied.

$$\nabla^2\varphi = \nabla \cdot (\vec{v} \times \overrightarrow{B_o}) \qquad \text{[Eq. 2.26]}$$

The electric field is written as:

$$\vec{E} = \nabla \varphi - \frac{\partial \vec{A}}{\partial t} \qquad \text{[Eq. 2.27]}$$

Equation 2.26 is solved by considering the electric field, expressed as the gradient of a scalar potential φ, minus the time dependent magnetic vector potential $\frac{\partial \vec{A}}{\partial t}$, as shown in equation 2.27.

In time independent calculations, the Lorentz force in this method can be written as:

$$\vec{F} = k(-\nabla \varphi + \vec{v} \times \overrightarrow{B_o}) \times \overrightarrow{B_o} \qquad \text{[Eq. 2.28]}$$

The Lorentz force is added to the RANS equations as a source term [87].

Water modeling is widely used to simulate fluid flow in continuous casting processes. However, its electrical conductivity is very low to represent electromagnetic forces properly. As the physical modeling of mold fluid flow with low melting point metals and proper electrical conductivity, such as Ga or Sn, is very expensive, researchers rather use mathematical modeling as a tool for understanding the electromagnetic forces so as to improve the design and configuration of EMS. In any case, it is always better to complement the output obtained from numerical simulations with plant trials.

Yu Haiqi and Zhu Miaoyang [88] simulated a 3D combined Finite Element Method (FEM) and Finite Volume Method (FVM), for a Magnetohydrodynamics (MHD) model in which the flow field, heat transfer and of inclusions trajectory have been coupled, so as to investigate the fluid flow in a copper round billet mold. In their model, the M-EMS was positioned at 0.8 m from the top surface of the billet and the space between the stirrer and the mold wall was considered as an air gap. By the interaction of the applied Alternate Current (AC) and the time dependent rotational magnetic fields, the Lorentz force is activated through the molten steel in the direction of the rotating field. The distribution of the magnetic field is first calculated through the mold domain, and after that the Lorentz force is predicted as a momentum source term. The governing equations were solved by the commercial software ANSYS-FLUENT. The model has been validated by measuring the magnetic flux density in an empty mold, using a SHT-III Digital Teslameter. They found that with the use of M-EMS, the velocity vectors are directed in a rotational and upward directions, which greatly differs with the mold flow case where no EMS is applied. In this case, the velocity vectors are mainly directed towards the bottom of the mold. The superheat is better dissipated by the M-EMS case, for which a more uniform gradient in temperatures was predicted. As the fluid flow is directed upwards, higher temperatures were observed near the meniscus area as compared to the no EMS case, as shown in Figure 2.15. Therefore, the solidification rate and the superheat are both reduced with the use of M-EMS, and this will enhance the formation of equiaxed grains. A rotational motion of the inclusion particles is promoted by the M-EMS, so that they have a longer time to float out into the surface of the liquid steel.

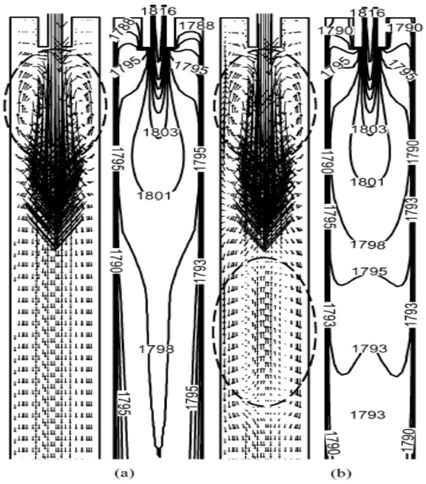

Figure 2.15 Velocity and temperature fields in the mold. a) Without M-EMS. b) With M-EMS.

Other authors have considered the use of dual-in M-EMS [89]. By arranging two M-EMS systems, in series, along the billet mould axial direction, a higher tangential velocity inside the mold, and lower fluctuations, are expected in the surface. By having these velocity patterns in different zones of the mold, an improvement of the inner and surface quality of the steel billet is anticipated. The MHD model was calculated, applying a FEM to a square billet mold. They found that with the dual-in M-EMS system, it was very difficult to mantain a stable level in the meniscus region.

Hua-jie Wu et al. [90] investigated the effect of M-EMS on the solidification structure in a square billet. The electromagnetic torques for different M-EMS parameters were measured using a torque meter. The equiaxed crystal zone was analyzed by applying hydrochloric acid, and heated to 60-80 °C for 25-30 min. As the macrostructure of the billets emerges after washing and drying, the equiaxed crystal ratio is revealed and can be calculated. Similarly, after applying hydrochloric acid and heating, different samples were studied by an optical microscope for dendrite arm spacing analysis. They found that the frequency has no effect on the electromagnetic torque. However, when the current intensity is increased, the torque also increases. The equi-axed crystal ratio increased by increasing the electromagnetic torque. When a higher electromagnetic stirring intensity was applied, the cooling rate increases. The cooling rate is higher near the walls of the mold, where the electromagnetic stirring effect is higher, and reduces near the central area of the mold. The segregation and porosity of billets is reduced by increasing stirring intensity.

M. Javurek et al. [91] conducted Particle Image Velocimetry (PIV) experiments using a full scale round mould, neglecting the curvature (which may influence the fluid flow significantly) and the effect that the solidifying shell has in the reduction of the liquid core. The plastic round mold was surrounded by a rectangular box filled with water, in order to have a plane surface so that the reflections caused by a cylindrical shape, when shooting the PIV laser, are avoided. The MHD model, coupled with fluid flow and inclusion behavior, was solved with the commercial software FLUENT. The PIV experiments and the mathematical models were in good agreement. However, PIV modeling showed that the flow has larger turbulent fluctuations, which were not observed in the mathematical model. The authors affirmed that the FLUENT MHD module may over-predict the magnetic forces. Therefore, an alternative method by coupling the ANSYS EMAG solver for solving the electromagnetic and Lorentz forces, and FLUENT for fluid flow was proposed [92]. The two models have their own mesh and the matching between the two solvers is arranged by MpCCI, a commercial code coupling interface that also performs the interpolation. The results obtained from simulations with full coupling and simplified coupling turned out to be very similar. The fully coupled method represents a higher cost but a higher accuracy is expected.

B.A. Zivak et al. [93] affirmed that the main index to follow a satisfactory EMS practice is to record the highest linear velocity attained due to the stirring. EMS practices become less effective when v_{max} < 0.3 m/s, where surface effects and macrostructure problems arise. The maximum velocities for bloom casters are 0.3m/s< v_{max}<0.6 m/s. Pores and negative segregation are formed when v_{max} > 1 m/s. Different parameters have to be taken into account when choosing and selecting the magnitude of flow velocity, such as casting speed, superheat and the grade of steel. J.K. Yoon reviewed the methods for numerical simulations used for the different electromagnetic practices in the continuous casting process [94]. Similarly, B. Thomas and Rajneesh Chaudhary [95] reviewed the electromagnetic systems and computational methods related to steel processing.

S. Kobayashi et al. [96,97] conducted experiments in a round mold filled with liquid steel by casting a number of ingots stirred by a magnetic field. Different parameters such as wall shear stress, flow velocity and degree of mixing were calculated by the k-ω turbulence model. They found that the equiaxed zone ratio (EQRT) increases by increasing the wall shear stress. By operating with a v_{max} > 0.15 m/s and a shear stress τ_w> 3 N/m^2, the electromagnetic stirring results were more effective. The appearance of TrEMS (Trace of electromagnetic stirring), defined as a fine dendrite zone in a ring shape, occurred when τ_w> 10 N/m^2 or v_{max} > 0.35 m/s. The re-melting of dendrite arms needs fluctuating temperatures at the solid-liquid interface. The fluctuations are represented by turbulent kinetic energy K. This energy is uniform near the liquid-solid interface and can be written as $K = 3.3\ \frac{\tau_w}{\rho}$ [98]. The area of equiaxed zones were shown to have a good correlation with the shear stress, but no there was correlation with electromagnetic forces or turbulence mixing. This is in agreement with equation of K for fluid flow near a solid-liquid interface.

H. Mizukami et al. [99] simulated solidification of liquid steel in a refractory lined square mold operating under EMS. Thermocouples were installed at the stirred level located at the mid height of the mould where two types (Linear and rotary type) of EMS were positioned alternatively. This height is mentioned to be the optimal position for the stirrers, since the stirring should start once the precipitation of the crystals has started. These two types of stirrers were used so as to compute the influence of the stirring direction. When the linear system was used, two stirrers were installed, so that a vertical force was induced in the vertical direction. Similarly, the rotary system was also installed at the same height, inducing rotational forces. In order to analyze the linear system, the forces were induced upwards and downwards. It was found that the downward flow at the solidification front enhanced the formation of V-segregation streaks in earlier stages of solidification. Conversely, the upward flows tend to retard the formation of V-segregation streaks. In addition, the short stirring times are enough to eliminate V-segregation streaks. Larger areas of equi-axed crystals were observed by the combination of stirring during the first and final stages of the strand, when working with the rotary EMS system. To attain the desirable output from the Electromagnetic forces was more complex in this case. If the stirring time is too long, the interdendritic liquid flows in the solid-liquid interface region lead to V-segregation. Alternating flow patterns are also suggested to avoid undesirable downward motions near the solidification front. Optimal conditions were found when velocities were in the order of v_{max} > 0.1 to 0.2 m/s. Other researchers suggested that natural convection can also influence the growth of size and extent of equi-axed grain zones[100].

Industrial experiments were conducted by Zhou Shu-cai et al. [101], so as to investigate the effect of low frequency EMS practices on the solidification structure of austenitic stainless steel. They found that by applying low frequencies, the rotary forces enhanced convection flow in the melt and reduced the temperature gradients near the solidification front. Therefore, maintaining a more uniform shell growth by improving the heat transfer. The adequate EMS operating conditions reduces shrinkage cavity, improves the width of equi-axed grains zones and segregation.

An improvement in surface quality of billets has been reported by H. Nakata et al. [102] using a M-EMS system. The inclusions and pinholes in the subsurface were significantly reduced by electromagnetic stirring. The upward flowing of liquid steel induced by the application of M-EMS imposes Saffman forces on non-metallic inclusions. These forces prevent the entrapment of inclusions in the growing shell. If the velocity of the liquid steel generated by EMS is larger than the solidification front velocity of the initial solid shell, the inclusions are not expected to be entrapped [103] [104]. A 100 µm inclusion is considered to be washed out at a flow velocity of 0.3 m/s, while inclusions sizes of 40-50 µm would be removed from the solidification front, if the velocity is in the range of 0.5 to 0.6 m/s, as shown in Figure 2.16.

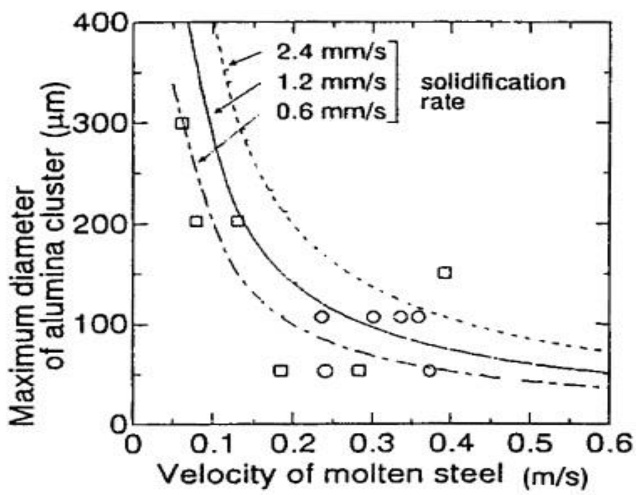

Figure 2.16 Scheme showing the steel velocity and particle size of alumina cluster.

Y. Tsukaguchi et al. [105] studied "the swirling flow formation" in the SEN by conducting experiments in a round billet mold. The working liquid for the experiments was Wood's Metal and an impeller was positioned in the upper part of the SEN which triggered the swirling motion. The impeller was combined with a M-EMS system so as to observe the interaction of rotational components. They found that the M-EMS increases more the energy for the wood metal rotation in the mold than the impeller rotation in the SEN. In addition, the impeller rotation in the nozzle is limited to the area near the meniscus. When the M-EMS system and the impeller are combined, the M-EMS cancels the effect of the impeller, since it has a stronger effect on the fluid flow. The impeller acting alone, activates a low magnitude centrifugal force, capable of creating an upward flow. K. Stranksy et al. [106] found that the EMS systems suppress columnar crystal growth of billets as well as the cracking during casting at low temperatures. The greatest benefits were observed when M-EMS and S-EMS were simultaneously used. K. Ayata et al. [107] conducted plant trials with different arrangements of electromagnetic systems. Different configurations have been used including M-EMS and F-EMS for continuous casting of bloom and billets as shown in Figure 2.17.

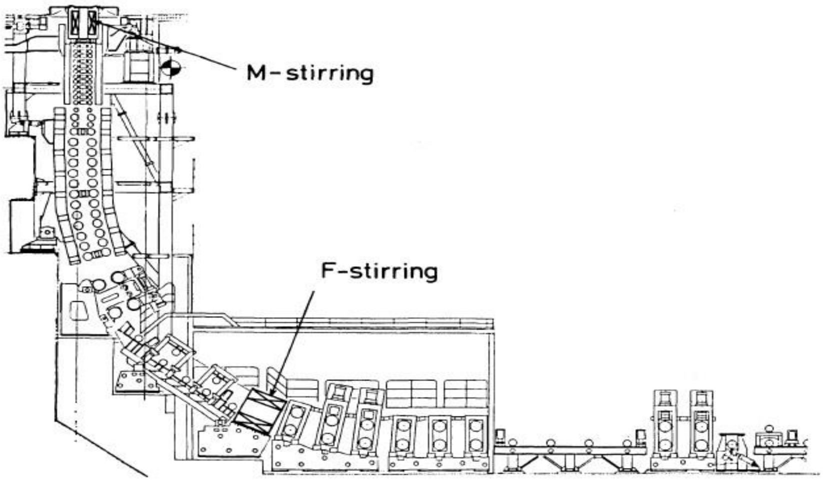

Figure 2.17 Scheme of a Continuous Casting Machine for a bloom arranged with a (M-EMS + F-EMS).

Low, medium and high carbon steel were tested at different frequencies. They found that medium carbon steel formed wider equiaxed crystal zones compared to low and high carbon steels when using M-EMS or M-EMS + S-EMS systems. Therefore a combination of stirrers (M-EMS + F-EMS) becomes necessary so as to decrease centerline segregation. The centerline segregation of low and high carbon steel, is greatly improved by the combination of a (M-EMS + F-EMS) system.

2.7 Final remarks

From this review, it is observed that physical and mathematical modeling, are both very useful tools in helping to understand the transport phenomena taking place within the molds, and to thereby be able to improve the process itself and operations. Complex mathematical models to simulate EMS systems in the continuous casting process, to provide insights on the process for casting blooms and billets, are strongly emerging in this field of research. Plant experiments are also used to validate and complement these models. However, a reliable model that includes all involved transport phenomena is very difficult to produce for a given operation. In addition, plants usually select the configuration of the EMS systems on a trial and error basis, mainly because the interaction of electromagnetic forces with the liquid steel is very complex and still not fully understood. The assessment of the effects of SEN design, coupled with EMS forces, on the fluid flow is an area that needs further exploration.

A common trend to use a single port nozzle in the continuous casting of blooms and billets has been observed in the literature. However, a comparison of the performance between a single nozzle and multiport nozzles operation is not readily found. A blade in the SEN has been proposed to improve the process. Although the fluid flow is highly improved with a swirl blade, the geometry of it could be hard to maintain due to erosion with constant impingement of molten steel. Similarly, the swirl blade can act as a site for the agglomeration of inclusions that could lead to nozzle clogging. Other innovative alternatives to control the fluid flow by SEN design have not been proposed yet. Therefore, this is an area that needs further exploration. A large amount of papers are found in the literature related to fluid flow control in continuous casting molds. In here, major efforts have been carried out to design proper SEN's that can deliver a uniform fluid flow in the mold cavity so as to improve liquid steel cleanliness. However, a vast percentage of these efforts are found to be conducted toward slab casting and less attention has been devoted in understanding fluid flow phenomena and vortex generation in round and square billet casters.

3.0 General Procedures for Physical and Mathematical Modeling

3.1 Water Modeling Procedures

Physical modeling was carried out using a full-scale water model of both the round, and, square billet, molds. They are fed from a twelve tonne, delta-shaped, four strand tundish. In the present setup, the level of water in the model tundish exactly matched the level of steel in the plant tundish. The water supply was obtained using a recirculating flow system that consisted of a flow meter and a pump that feeds the tundish. The water level of the tundish was maintained at a height of 0.5 m to match the steady state operation in the real caster. The water from the tundish passed through a reducing pipe that connects the tundish outlet with the selected SEN according to the type of mold used for the experiments. The mold was filled with water and reached a steady state free surface level corresponding to that in the plant. The bottom of the mold was connected to the recirculating pump and the cycle starts again. The first setup consisted of a syringe located in the upper part of the SEN, in order to inject the dye. A high speed camera was positioned in front of the mold, so as to record the evolution of the pulse of dye colored water mixing with the clear water inside the mold. The flows were recorded until the dye was completely mixed throughout the volume of the mold. The second setup focused on the fluid dynamics behavior using the corresponding SEN design. For that purpose, a Particle Image Velocimeter (PIV) from DANTEC® was employed, consisting of a laser gun with a power of 20 mJ, a Coupled Charged Device (CCD) to record the motion of seeding particles in the flow, and software to perform the Fast Fourier Transform analysis of the velocity signals transferred to a computer. The round mold was physically surrounded by a rectangular box which was filled with water so as to avoid laser light reflection problems from the round geometry that would lead to wrong results. The interrogation area involved the SEN discharge, and the near wall and meniscus regions. A mirror, set at an angle of about 45^0 with respect the vertical plane, was placed on one side of the mold, while the laser gun was located in its front. The laser light sheet from the gun was reflected on the mirror so as to form another vertical laser sheet that coincided exactly with the central axis of the SEN and other selected planes. At a selected time, a slurry of seeding particles (polyamide particles with a size of 20 microns and density of 1.04 g/cm^3) were injected into the entry water flow, using the syringe. The recording time started to follow the flow dynamics. Figure 3.1 and 3.2 show snapshots of the experimental setups. In addition, water-oil experiments were conducted so as to observe the interface dynamics. The thickness of the vegetable oil layer simulating the slag layer was 0.015 m (density equivalent to ρ_{oil} = 850 kg/m^3, and viscosity μ_{oil} = 0.399 kg/m*s).

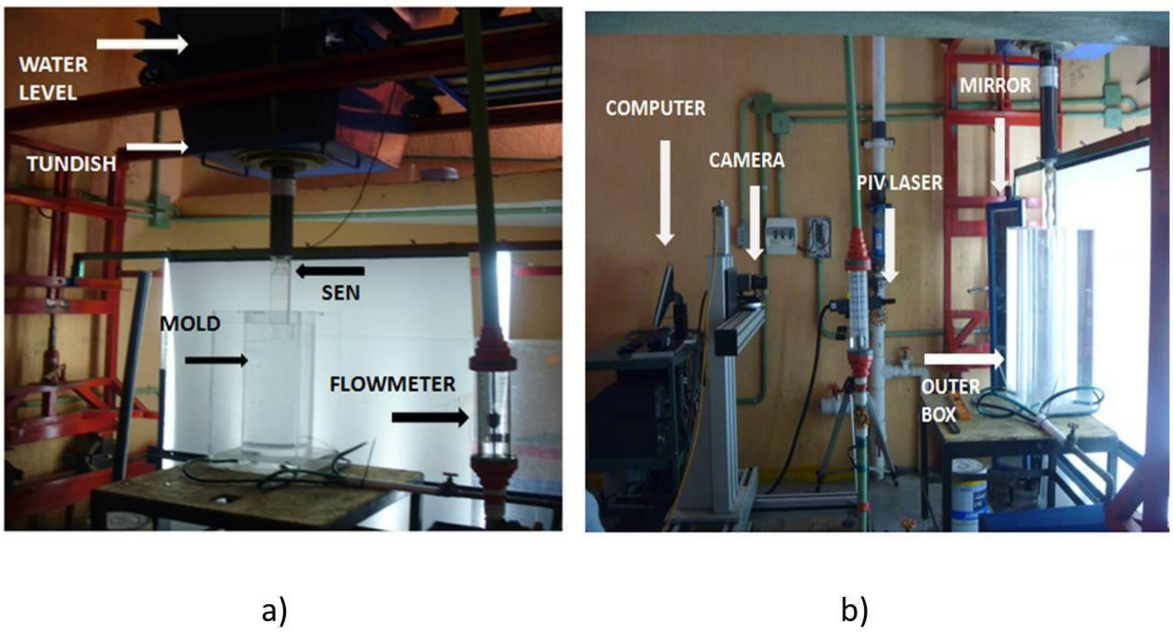

Figure 3.1 Round mold experimental setup. a) Photo showing tundish and round mold setup b) Photo of PIV and camera setup.

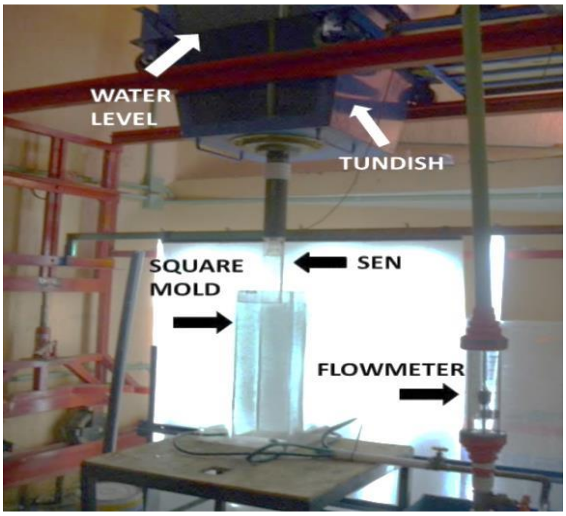

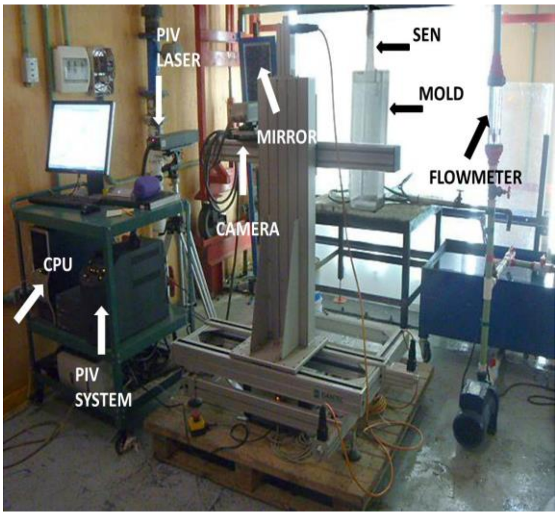

a) **b)**

Figure 3.2 Square mold experimental setup. a) Photo showing tundish and square mold setup b) Photo of PIV and camera setup.

3.2 Mathematical modeling procedures

The general convection-diffusion equation that is applied for solving problems related to transport phenomena is described below.

$$\frac{\partial(\rho\phi)}{\partial t} + \nabla \cdot \rho u \phi = \nabla \cdot (\Gamma \nabla \phi) + S \quad \text{[Eq. 3.1]}$$

In this equation, the variable of interest ϕ represents (u, v, w, c, T, k, ε, etc.). Subsequently, S is the volumetric generation rate or source term, and Γ is the diffusion coefficient corresponding to ϕ. From the above equation, the mass, momentum and energy conservation equations are derived.

A central objective of this work was to detect disturbances to the fluid flow, in order to understand the occurrence of mold powder particle entrainment in round and square billet casters. It was decided to use the Realizable k-ε model [108] which has a better capability to predict vortex flows [109]. The key to that turbulence model is the combination of the Boussinesq relationship with the classical eddy-viscosity definition [110] to obtain the following expression for the normal Reynolds stresses in an incompressible strained flow,

$$\bar{u}_i^2 = \frac{2}{3}k - 2\nu_t \frac{\partial u}{\partial x} \qquad \text{[Eq. 3.2]}$$

Where, $\nu_t = \mu_t/\rho$, when the strain is large enough to satisfy

$$\frac{k}{\varepsilon}\frac{\partial u}{\partial x} > \frac{1}{3C_\mu} \approx 3.7 \qquad \text{[Eq. 3.3]}$$

The normal Reynolds stress becomes “non-realizable” because, by definition this amount should be positive, i.e., “realizable”. To ensure realizable normal Reynolds stresses, this model makes the constant C_μ, which is the same as in the typical k-ε model, a variable and dependent on vorticity and strain rates in addition to being a function of k and ε. Additionally, a new equation for the dissipation rate of the turbulent kinetic energy is proposed [110]. Therefore, the equations of continuity and momentum transfer must be solved simultaneously together with the following equations for the turbulent kinetic energy and its dissipation rate;

Continuity:

$$\frac{\partial \rho}{\partial t} + \frac{\partial}{\partial x_j}\left(\rho u_j\right) = 0 \qquad \text{[Eq. 3.4]}$$

Momentum:

$$\frac{\partial}{\partial t}(\rho u_i) + \frac{\partial}{\partial x_j}\left(\rho u_i u_j\right) = -\frac{\partial P}{\partial x_i} + \frac{\partial}{\partial x_j}\left[\mu_{eff}\left(\frac{\partial u_i}{\partial x_j} + \frac{\partial u_j}{\partial x_i}\right)\right] + \rho g \qquad \text{[Eq. 3.5]}$$

Transport of kinetic energy of turbulence:

$$\frac{\partial(\rho k)}{\partial t} + \frac{\partial(\rho k u_j)}{\partial x_j} = \frac{\partial}{\partial x_j}\left[\left(\mu + \frac{\mu_t}{\sigma_k}\right)\frac{\partial k}{\partial x_j}\right] + G_k - \rho\varepsilon \qquad \text{[Eq. 3.6]}$$

Rate of dissipation of the kinetic energy of turbulence:

$$\frac{\partial(\rho\varepsilon)}{\partial t}+\frac{\partial(\rho\varepsilon u_j)}{\partial x_j}=\frac{\partial}{\partial x_j}\left[\left(\mu+\frac{\mu_t}{\sigma_\varepsilon}\right)\frac{\partial\varepsilon}{\partial x_j}\right]+\rho C_1 S\varepsilon-\rho C_2\frac{\varepsilon^2}{k+\sqrt{\nu\varepsilon}} \qquad \text{[Eq. 3.7]}$$

The effective viscosity is the sum of laminar and turbulent viscosities:

$$\mu_{eff}=\mu+\mu_t \qquad \text{[Eq. 3.8]}$$

The pseudo constant C_1 is maximized among the following set,

$$C_1=max\ \left[0.43,\frac{\eta}{\eta+5}\right],\eta=S\frac{k}{\varepsilon},\ S=\sqrt{2S_{ij}S_{ij}} \qquad \text{[Eq. 3.9]}$$

Where the production of turbulence kinetic energy is described as:

$$G_k=\mu_t\frac{\partial u_i}{\partial x_i}\left(\frac{\partial u_i}{\partial x_i}+\frac{\partial u_i}{\partial x_j}\right) \qquad \text{[Eq. 3.10]}$$

Other parameters and constants of this model are provided in Table 3.1.

Variable	Equation
Turbulent viscosity	$\mu_t=\rho C_\mu\frac{k^2}{\varepsilon}$
Constant of turbulence	$C_\mu=\frac{1}{A_0+A_s\frac{kU^*}{\varepsilon}}$
Global deformation	$U^*=\sqrt{S_{ij}S_{ij}+\tilde{\Omega}_{ij}\tilde{\Omega}_{ij}}$
Mean rotational	$\tilde{\Omega}_{ij}=\Omega_{ij}-2\epsilon_{ijk}\omega_k$
Rotational deformation rate	$\Omega_{ij}=\frac{1}{2}\left(\frac{\partial u_j}{\partial x_i}-\frac{\partial u_i}{\partial x_j}\right)$
Constants of viscosity	$A_0=4.04,\quad A_s=\sqrt{6}\cos\phi$
Model parameters and tensor of deformation rates	$\phi=\frac{1}{3}\cos(\sqrt{6}W),\quad W=\frac{S_{ij}S_{jk}S_{ki}}{\tilde{S}^3},\quad \tilde{S}=\sqrt{S_{ij}S_{ij}},$ $S_{ij}=\frac{1}{2}\left(\frac{\partial u_i}{\partial x_j}+\frac{\partial u_j}{\partial x_i}\right)$
Other model constants	$C_{1\varepsilon}=1.44,\quad C_2=1.9,\quad \sigma_k=1.0,$ $\sigma_\varepsilon=1.2$

Table 3.1 Complementary Equations of the Mathematical Model

3.2.1 Modeling of tracer injection and multiphase flows

For simulating the dispersion of the tracer, the velocity field is calculated from the preceding equations and used in the next mass transfer equation,

$$\frac{\partial C}{\partial t} + u \cdot \nabla C = D_{eff} \nabla^2 C \qquad \text{[Eq. 3.11]}$$

In this equation, D_{eff} is the effective diffusivity, which is the sum of molecular and turbulent diffusivities, according to;

$$D_{eff} = D_0 + \frac{\mu_t}{\rho Sc_t} \qquad \text{[Eq. 3.12]}$$

where D_0 is the molecular diffusivity and Sc_t is the turbulent Schmidt Number. Because turbulent flows generally carry mass over an equivalent Schmidt mixing length, this coefficient was assumed equal to one.

In the Volume of Fluid multiphase model, a single set of momentum equations are solved for all the fluids in the domain. This method employs a tracking technique between two or more immiscible fluids in which the interface position is of interest. The volume fraction of each fluid is calculated throughout the domain. For any additional phase added to the model, a new variable is introduced as a volume fraction of the new phase in the computational cell. Mass conservation is ensured by equating the volume fractions of all phases to unity in each control volume. The properties and fields for all variables are shared by the phases and represent volume-averaged values. Thus, the variables and properties in any given cell are either entirely representative of one of the phases, or representative of a mixture of the phases, depending upon the volume fraction values [109].

This can be explained as if the q^{th} fluid's volume fraction in the cell is denoted as α_q, then the following three conditions are possible:

$\alpha_q = 0$: The cell is empty (of the q^{th} fluid).

$\alpha_q = 1$: The cell is full (of the q^{th} fluid).

$0 < \alpha_q < 1$: The cell contains the interface between the q^{th} fluid and one or more other fluids.

Based on the local value of α_q, the appropriate properties and variables will be assigned to each control volume that is part of the domain. The tracking of the interfaces between phases is obtained by the solution of continuity equations for the volume fractions of one or more phases present in the domain.

$$\frac{1}{\rho_q}\left[\frac{\partial}{\partial t}\left(\alpha_q\rho_q\right) + \nabla\cdot\left(\alpha_q\rho_q\vec{v_q}\right)\right] = S_{\alpha_q} \qquad \text{[Eq. 3.13]}$$

The volume fraction for the primary phase is not solved. Rather, it is computed based on the following equation:

$$\sum_{q=1}^{n}\alpha_q = 1 \qquad \text{[Eq. 3.14]}$$

For modeling the steel, slag and air interface, the Volume of Fluid (VOF) approach was used in this research.

3.2.2 Solution Methods and boundary conditions

For solving the set of partial differential equations, together with its parameters and constants, the commercial software ANSYS-FLUENT 14 was used. The working fluid for the single phase simulations was either water or steel, under isothermal conditions. The properties of water and liquid steel were: ρ_w= 1000 kg/m^3, μ_w =

0.001 Pa-s, ρ_s = 7050 kg/m^3 and μ_s = 0.0062 kg/m-s, respectively. To simplify the computations, the free surface of the fluid in the mold was assumed to be flat, where a zero shear stress boundary condition was imposed. The confining walls of the mold and nozzles were subjected to a non-slip condition. At the inlet in the top of the SEN, a flat velocity profile is assumed. The inlet velocity is calculated to maintain the desired casting speed at the outlet by the following equation:

$$U_{in} = {}^{Q}\!/_{A_{in}} \qquad \text{[Eq. 3.15]}$$

The values of k and ε at the SEN inlet were computed from the following equations:

$$k_{in} = 0.01U_{in}^{2} \qquad \text{[Eq. 3.16]}$$

$$\varepsilon_{in} = 2k_{in}^{\frac{3}{2}} / D_{in} \qquad \text{[Eq. 3.17]}$$

Based on these assumptions, the flow field was obtained by the solution of the continuity, turbulence and momentum conservation equations in the three-dimensional domain. The set of partial differential equations were discretized using the Finite Volume Method in the previously mentioned commercial software by using a segregated solver through the implicit scheme for time discretization. The second order upwind scheme was established for the k, momentum, ε and species equations; and PRESTO (Pressure Staggering Option) for the pressure. The PISO (Pressure-Implicit with Splitting of Operators) [111] algorithm was used to solve the pressure–velocity coupling in the momentum equation. Default values of the under relaxation factor were used for all the variables. Near wall treatment was carried out using the standard wall function approach. Grid refinement near the walls was applied for each case for the proper implementation of the wall function. The time dependent solution was observed to not have significant changes after approximately 200 s of computational time, in which a time step of $1x10^{-3}$ s was applied. Therefore, each of the cases was run for 300 s to further ensure time independence of the final solution. Grid independency tests were also performed and the mesh was finally refined to around 1000000 cells (hybrid grid) for each one of the cases studied. Figure 3.3 shows the mesh on some of the planes used for analyzing fluid flow in this study. The converged solution was assumed to be obtained when the residuals were in the order of 1×10^{-4}, for each one of the turbulent flow variables. At this point, the species transport equation was enabled in the simulator, and a time independent boundary condition was applied by imposing a fixed mass fraction equivalent to 1 at the inlet, assuming that the injected tracer fully occupies the SEN volume as the only fluid coming into the domain. The numerical calculation was stopped once the incoming fluid was completely mixed throughout the mold cavity. The mass fraction of the tracer inside the mold was computed in different planes.

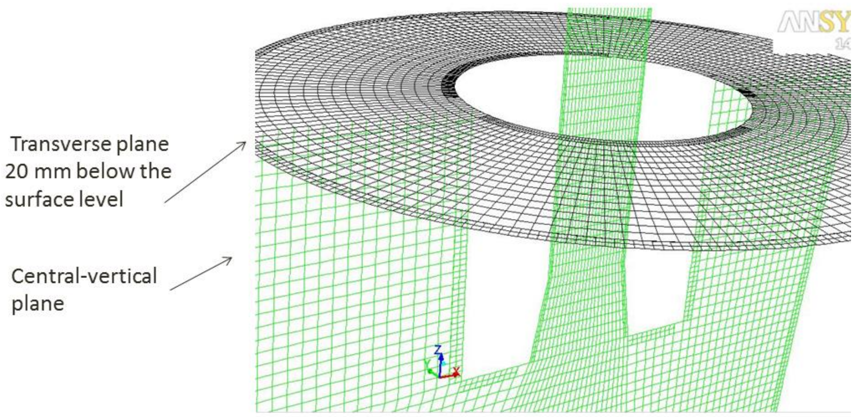

Figure 3.3 Scheme showing the mesh, the central-vertical and transverse planes

The behaviour of the slag layer was studied through the VOF method, and by considering constant interfacial tensions between the three phases. The complex interactions between the slag, air and steel, require a finer mesh so as to obtain a higher accuracy on the results. A refined mesh near the interface region with a total of 3,500,000 cells in the whole domain was used for the multiphase calculations. These simulations were conducted with the aid of a recently acquired HPC (High Performance Computer) by the MMPC.

4.0 Mold Powder Entrainment in a Round Billet Mold

4.1 Introduction

In current plant operations at Rio Tinto (RTFT), MPE defects have been detected in a round billet mold caster at different casting speeds. A bell shaped straight SEN, is currently used to pour the liquid steel coming from the tundish, while EMS practices are available but not necessarily used in the current arrangements. These surface and sub-surface defects are usually detected after the hot rolling process. These inclusions specifically formed by MPE are detrimental for the current quality requirements. In the present work, physical and mathematical modeling have been conducted using a full scale water model of a round billet caster, in order to explain the vortex formations, fluid flow phenomena and the possible causes for MPE occurring in the plant. At the end of this chapter, the effects of a misaligned nozzle on the fluid flow are also discussed.

4.2 Experimental and mathematical modeling procedures

As explained in the previous chapter, physical modeling consisted of PIV measurements, dye injection videography and water-oil simulations. Two casting speeds were considered for the experiments on this section, while the submergence depth was taken from the level surface, down to the tip of the straight nozzle. The properties of the fluid and operating conditions used to conduct the experiments are shown in Table 4.1. The laser of the PIV was positioned at the middle point of the round mold, to shoot the laser sheet at the central-vertical plane. The interrogation area encompassed the plane that goes from the inner radius to the outer mold radius in the horizontal axis and a distance of 0.26 m from the meniscus level, downward in the vertical direction. The instantaneous velocities were computed from the PIV measurements in two lines located at the inner and outer radius, as observed in Figure 4.1.

Properties and conditions	**Water (20°C)**
Molecular viscosity (μ), kg/m*s	0.001
Density (ρ), kg/m3	1000
Kinematic viscosity (v = μ / ρ), $\frac{m^2}{s}$	1.0 x 10^{-6}
Casting speed (m/min)	1.15,1.6
Immersion depth (mm)	123
Flow rate (L/min)	51,72
Steel throughput (tons/min)	0.363,0.505

Table 4.1 Properties of the water and operating conditions.

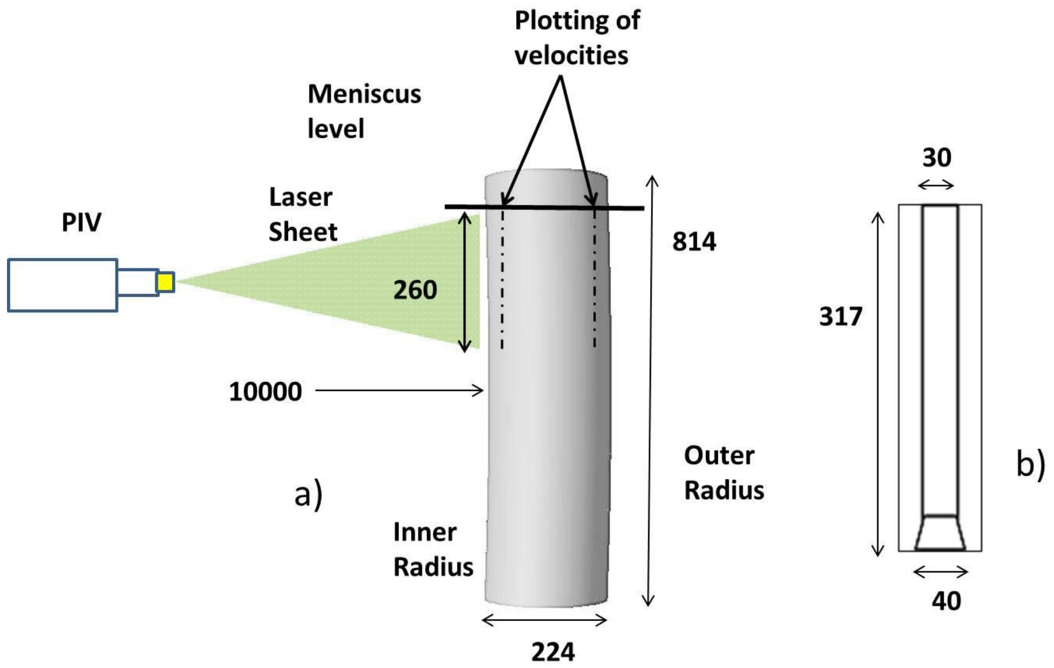

Figure 4.1 Physical dimensions of round mold and SEN used at RTFT. Figure 4.1a shows the geometric dimensions of the round mold and Figure 4.1b shows those corresponding to the straight nozzle.

Single phase mathematical models were considered in this section with the procedures explained in the previous chapter for such cases. The properties of water and the same conditions observed in Table 4.1 were applied in the mathematical simulations. The velocity fields and mass fraction of the tracer inside the mold were computed in two planes for the fluid flow analysis. The first plane is the vertical-central plane of the mold and the second one is a transverse plane located 20 mm below the meniscus as observed in Figure 4.2.

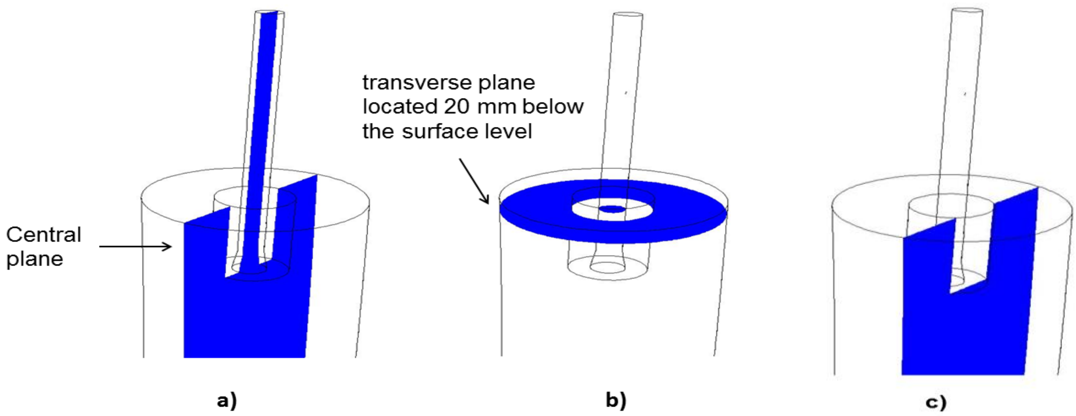

Figure 4.2 Scheme showing studied planes, a) the central-vertical plane, b) the transverse plane located 20 mm below the surface level; c) the vertical plane located 30 mm from the central axis.

4.3 Results and Discussion

4.3.1 Flow patterns and mathematical simulation

The fluid flow patterns provided by the dye injection at a casting speed of 1.15 m/min are shown in Figure 4.3 at different times after injection. The centrally located, vertical jet approaches closer to the internal mold radius, owing to the effects of the mould curvature, and penetrates close to the end of the mold. The incoming pulse of dye intermixes with the clear water, and is finally transported upwards along the outer mold radius, to reach the meniscus. Immediately afterwards, the colored fluid at the top continues to mix in with the remaining clear water, towards the inner mold radius. Evidently, the last mixing region is a band located in the upper left side in this 2D view of the mold. Besides, two regions remain unmixed even after relatively long mixing times, as indicated by the arrows.

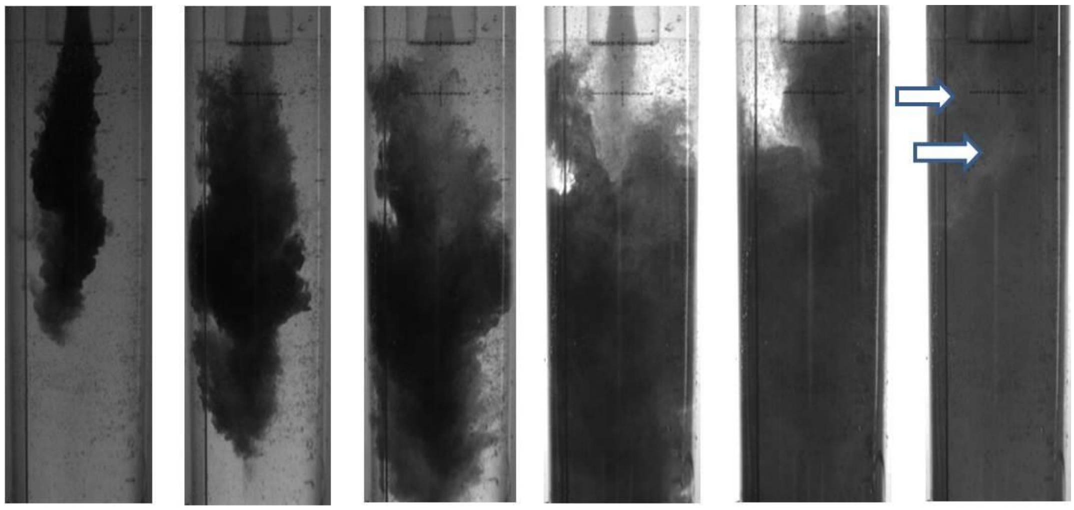

Figure 4.3 Snapshots showing the dye mixing at different times after the dye injection at a casting speed of 1.15 m/min.

The corresponding fluid flow patterns in the vertical central plane simulated by the mathematical model can be seen in Figure 4.4 at corresponding times. There is qualitatively good agreement as the results in Figure 4.3 correspond to a 3D view while those of Figure 4.4 correspond to a plane located at the center of the mold. Furthermore, it is observed that the same stagnant regions detected during the tracer injection experiments, marked with arrows in Figure 4.3, are also found in the mathematical simulations of Figure 4.4.

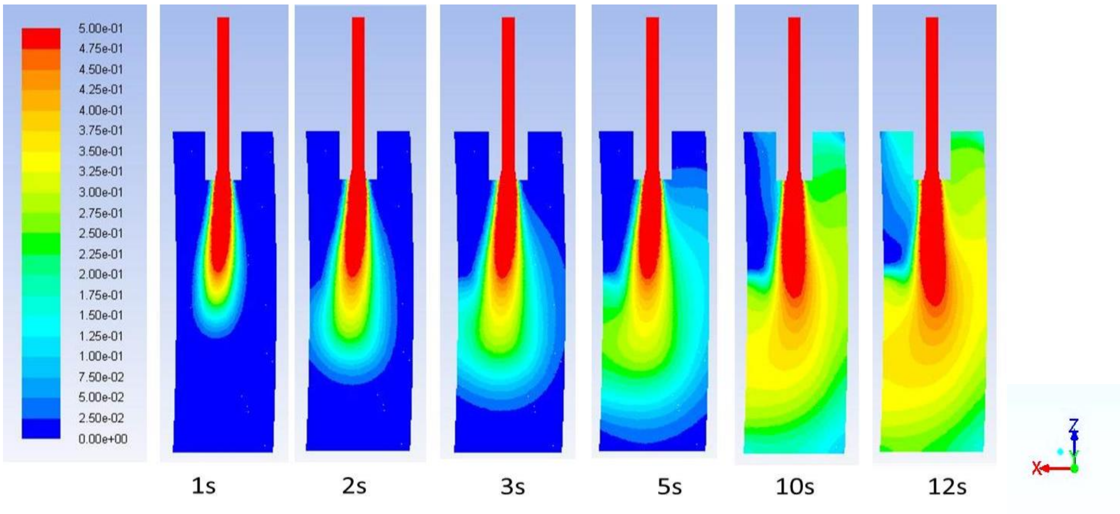

Figure 4.4 Scheme showing the mass fraction at different times predicted by the mathematical model at a casting speed of 1.15 m/min. The darkest region represents a mass fraction of 0.5 to 1.

Since the dye mixing pattern at a casting speed of 1.6 m/min was similar to that presented in Figure 4.3, here, only the mathematical simulations are presented in Figure 4.5 for different times following the pulse input of colored water. At a higher casting speed, the flow patterns remain similar and the difference between low (1.15 m/min) and high casting speed (1.6 m/min) is only the magnitudes of velocity vectors.

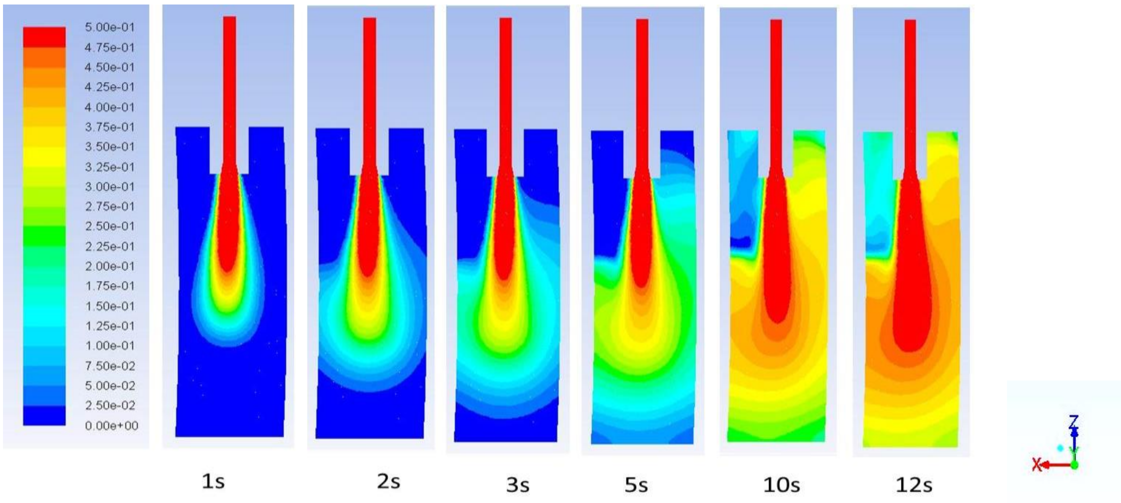

Figure 4.5 Scheme showing the mass fractions at different times predicted by the mathematical model at a casting speed of 1.6 m/min. The darkest region represents a mass fraction of 0.5 to 1.

This is evident from the predicted velocity vector fields for the central vertical plane in Figures 4.6a and 4.6b. Higher flowrates naturally brings about shorter mixing time, as seen. The more interesting of these two flow patterns is the existence of recirculating flows in the inner radius side of the mold induced, by shearing effects of the jet. These flows are sheared from the upper mold side by the upwards flow coming from the outer mold radius side which later flows downwards, after reaching the meniscus, along the inner mold side surrounding first the body of the SEN.

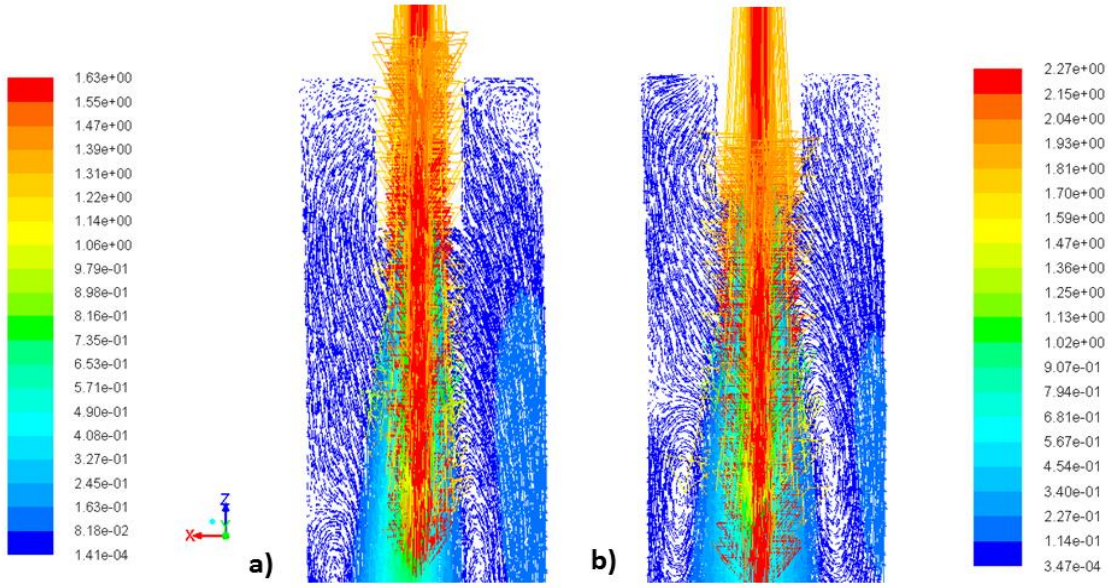

Figure 4.6 Velocity field on the vertical central plane of the mold (m/s). a) At a casting velocity of 1.15 m/min. b) At casting velocity of 1.6 m/min

At the confluence of both flows in the mold and specifically on the inner mold radius side, there is a stagnant region formed that corresponds to the longest intermixing time. This was observed in Figures 4.4 and 4.5 and is indicated by the arrows in Figure 4.3. Figures 4.7a and 4.7b show the flows in a horizontal plane located 20 mm below the bath surface with a difference, between both figures, of 13 s of flow time. In Figure 4.7a, it is clear that the velocities are quite small with the flow from the outer mold radius emerging as indicated by the arrow and the number “1”. After this, flow emerges along the outer radius of the mold dividing into two main streams that surround the nozzle body. There is a weak vortex flow indicated by the enlarged figure on the right that shows the region where these two streams meet. Since the flow is very turbulent, 13 seconds later, the velocities on this plane increase as seen in Figure 4.7b. Here, the emerging stream toward the bath surface is displaced to a lower position indicated by the arrow and the number “2”. A stronger vortex flow, enlarged in the figure on the right, is also developed and displaced to an upper position, versus that in Figure 4.7a. However, it must be noticed that whilst even stronger than in the preceding case, this vortex is still weak. As such, it is difficult to conclude that it has enough strength to induce MPE defects by suction.

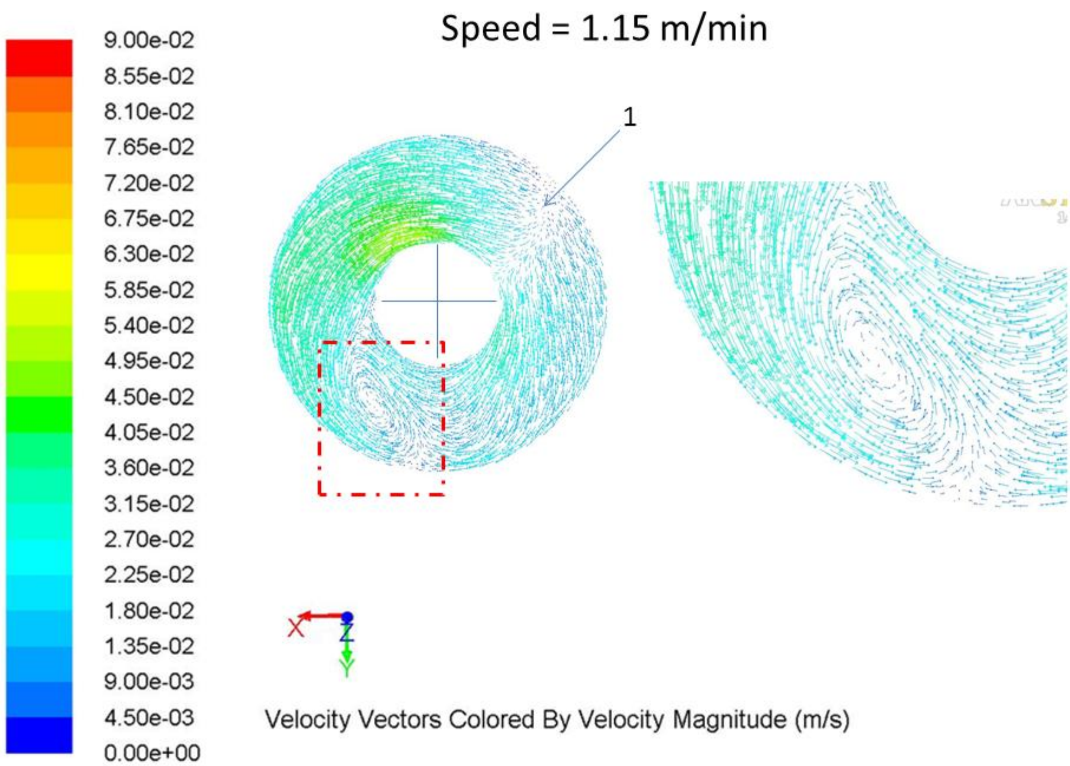

a)

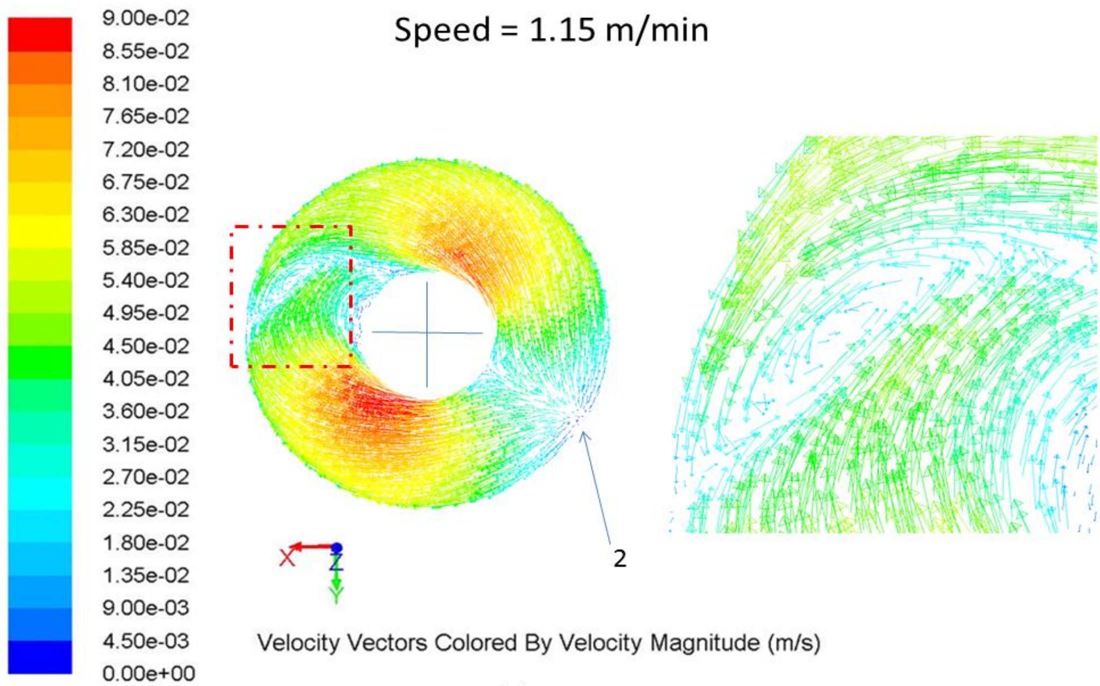

b)

Figure 4.7 Velocity field on a transverse plane of the mold (m/s) located 20 mm below the meniscus at a casting speed of 1.15 m/min. a) First vortex formation from low velocity magnitudes. b) Second vortex formation with higher velocity magnitudes.

Figures 4.8a and 4.8b show the same type of information for a casting speed of 1.6 m/min, in the first case the arrow and number “3” indicated the emerging flow coming from the outer mold radius. It is divided into two streams that also surround the nozzle. In the enlarged figure at the right side, three vortex flows can be identified. Some seconds later, due to the higher turbulence, the velocities increase as seen in Figure 4.8b and the emerging flow is now displaced upwards as indicated by the arrow and the number “4”. The three original vortex flows now merged into one with a larger strength, as seen in the enlarged figure at the right side, occupying a similar position to that in Figure 4.8a.

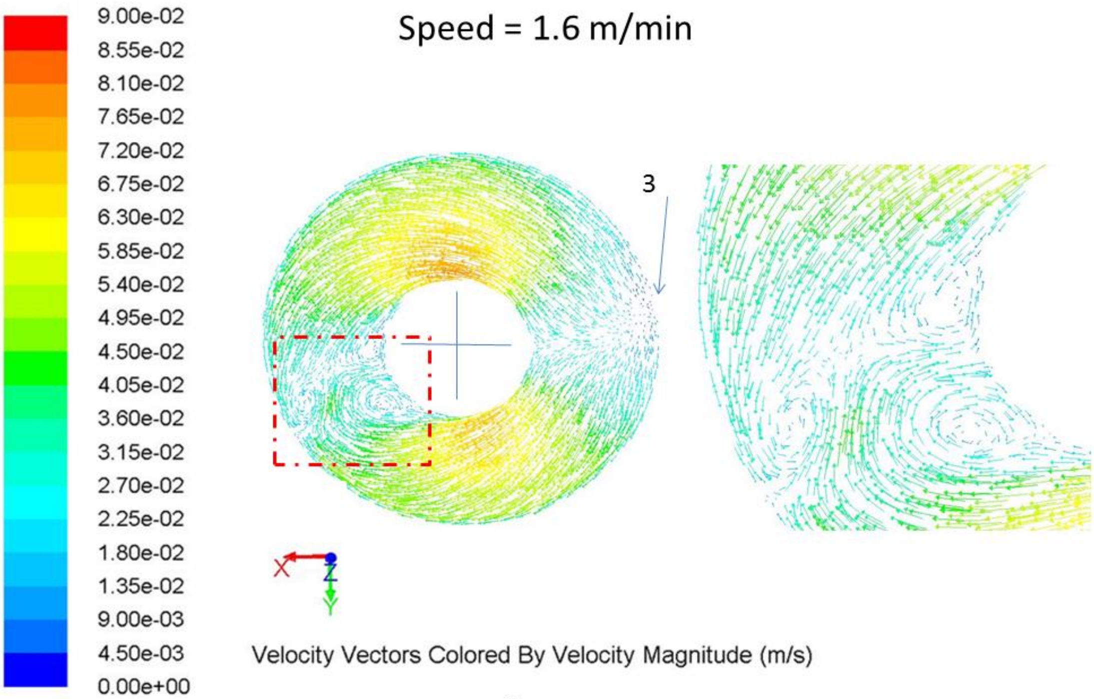

a)

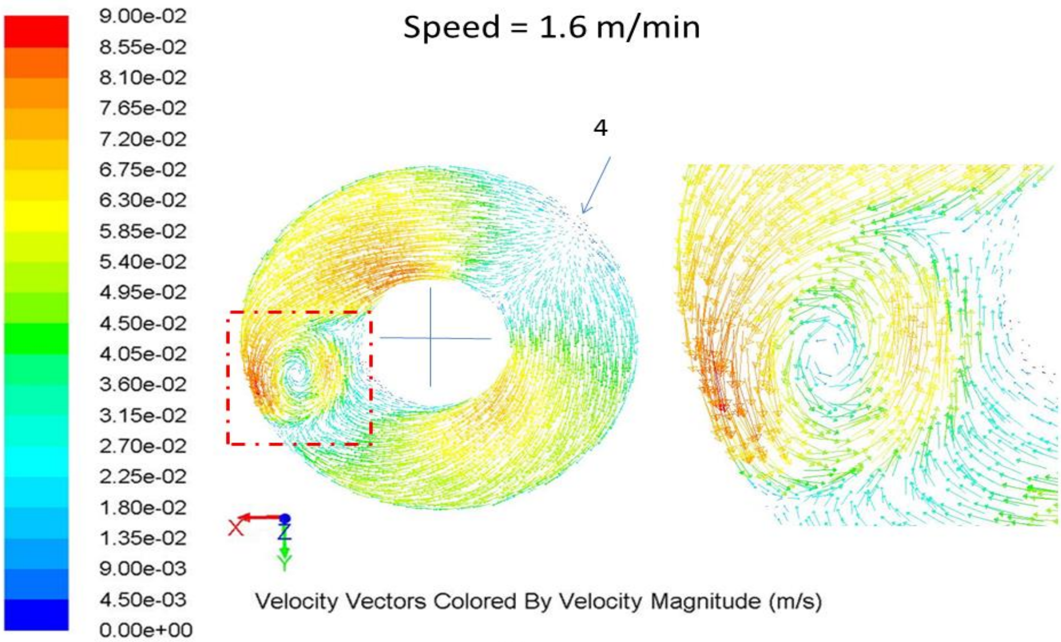

b)

Figure 4.8 Velocity field on a transverse plane of the mold (m/s) located 20 mm below the meniscus at a casting speed of 1.6 m/min. a) First vortex formation from low velocity magnitudes. b) Second vortex formation with higher velocity magnitudes.

The following Figures 4.9a and 4.9b, which correspond to Figures 4.7b and 4.8b, show the vortex flows in the vertical plane at casting speeds of 1.15 and 1.6 m/min, respectively. This figure shows the upper left region on the inner radius side. Inside the line dotted box, velocity vectors are observed to have different directions, which further sustain the three dimensional nature of vortex flows. The location of this plane can also be observed in Figure 4.2.

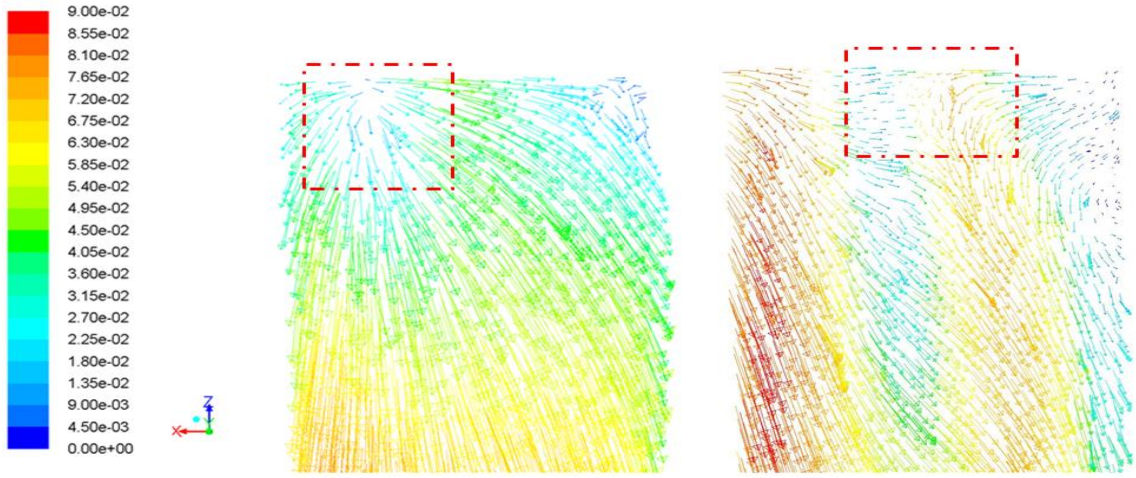

a) b)

Figure 4.9 Velocity field on a vertical plane located 30 mm from the central plane of symmetry m/s. a) Vortex formation at a casting speed of 1.15 m/min b) Vortex formation at a casting speed of 1.6 m/min.

Even though the vortex strength, as would be expected, increases at a higher casting speed, the velocities in the vortex flows observed in Figures 4.7-4.9 can hardly form MPE defects, since the velocities required for that are considerably higher, according to other researchers [112-114]. If that is the case, there must be an alternative mechanism that could describe the prevalence of this type of defect. In the following sections, it is intended to explain a mechanism that leads to Mold Powder Entrainment in round billet molds.

4.3.2 PIV measurements

It is a fundamental principle that turbulence produces vorticity flows whose magnitudes become larger as the kinetic energy of the entry jet increases. Vorticity is defined as:

$$\zeta = \nabla \times u \qquad \text{Eq. [4.1]}$$

which has a direct relation with the rotation rate of the fluid in a two-dimensional field, as provided by the 2D PIV measurements, ω through

$$\zeta_z = \left(\frac{\partial v}{\partial x} - \frac{\partial u}{\partial y}\right) = 2\,\omega \qquad \text{Eq. [4.2]}$$

Thus, angular velocity is half of the vorticity and, by convention, positive vorticity means a counter-clockwise rotation and a negative one corresponds to a clockwise rotation. Figures 4.10a and 4.10b show the vorticity and velocity fields measured by PIV techniques in a central vertical plane that goes from the inner to the outer mold radii, for a casting speed of 1.15 m/min. Figure 4.10a demonstrates the existence of a vortex in the bath surface that deepens down inside the bath, and this is also observed in the velocity field in Figure 4.10b. The arrows indicate these flow characteristics. On this vertical plane of the round mold, complex free shear flows are forming and recirculating vector fields can be observed.

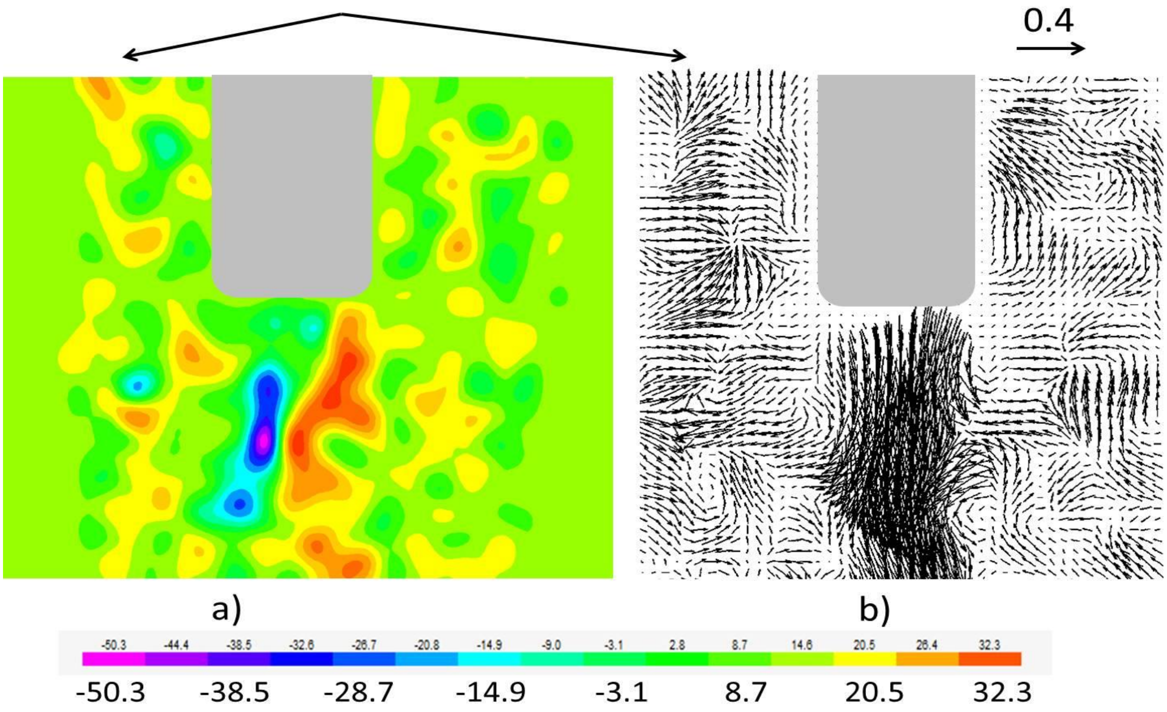

Figure 4.10 Vorticity and PIV results obtained in a central vertical plane at a casting speed of 1.15 m/min. a) vorticity contours (1/s) b) velocity field (m/s)

Figure 4.11a and 4.11b show the corresponding vorticity and velocity fields for a casting speed of 1.6 m/min, and similar comments to those preceding, are also applicable. The arrows indicate the position of the vorticity at the bath surface and its corresponding velocity field. The most important thing to notice from these experimental results is the presence of vortex flows in the bath surface, for both casting speeds, just as predicted by the mathematical simulations. It is also clear that the velocity vectors follow a vertical direction toward the free surface on the outer radius side of the mold, while the velocity vectors on the other side follow different directions. Similar fluid flow patterns were observed in Figures 4.6 and 4.9 by the mathematical model, although, of course, a more detailed velocity field is delivered by the PIV measurements.

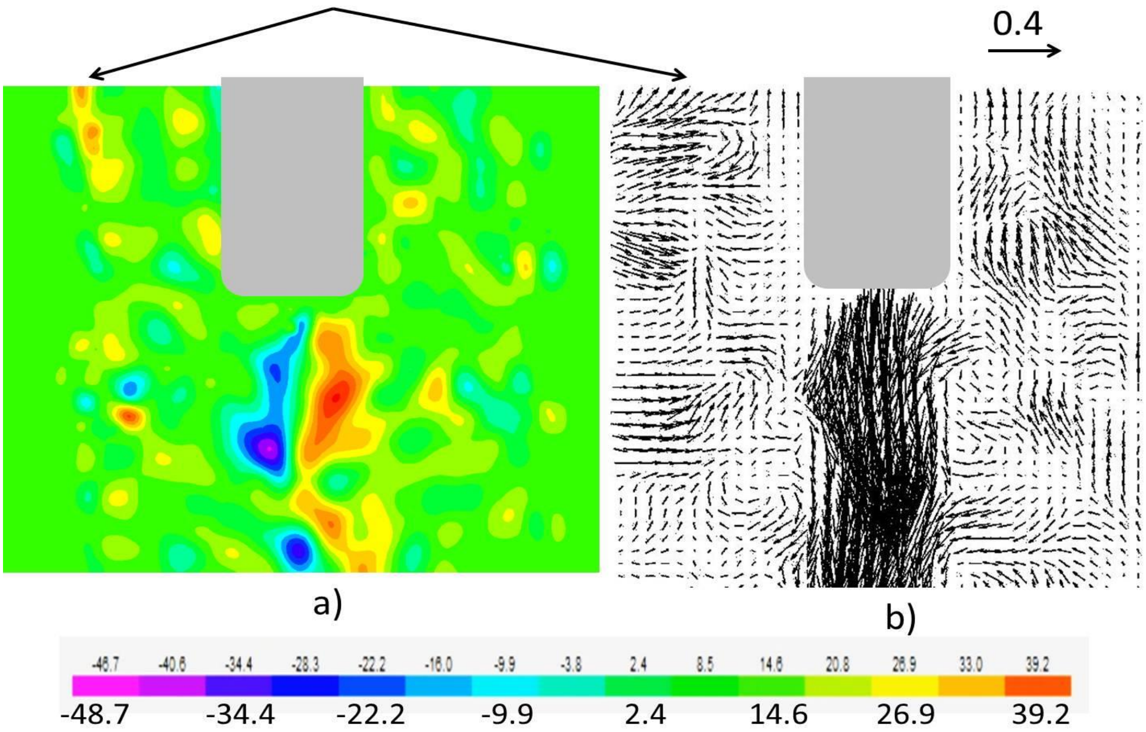

Figure 4.11 Vorticity and PIV results obtained in a central vertical plane at a casting speed of 1.6 m/min. a) Vorticity contours (1/s) b) Velocity field (m/s)

Figures 4.12a and 4.12b show the velocity magnitudes ($\left[(v_x{}^2)+(v_y^2)\right]^{1/2}$) down the internal (inner mold radius side) and external lines (outer mold radius side) respectively, for a casting speed of 1.15 m/min. These were determined from the analysis of a sequence of 300 images, where the numerical data of the velocity magnitudes corresponding to these two lines was imported from the PIV data sheet. The length of the two lines is 0.26 m., starting from zero at the meniscus level (see Figure 4.1), on down into the liquid pool. The existence of various velocity peaks indicate the recirculating nature of the free shear flows located on both sides of the jet. The largest peaks correspond to the largest free shear flows and maintain fixed positions.

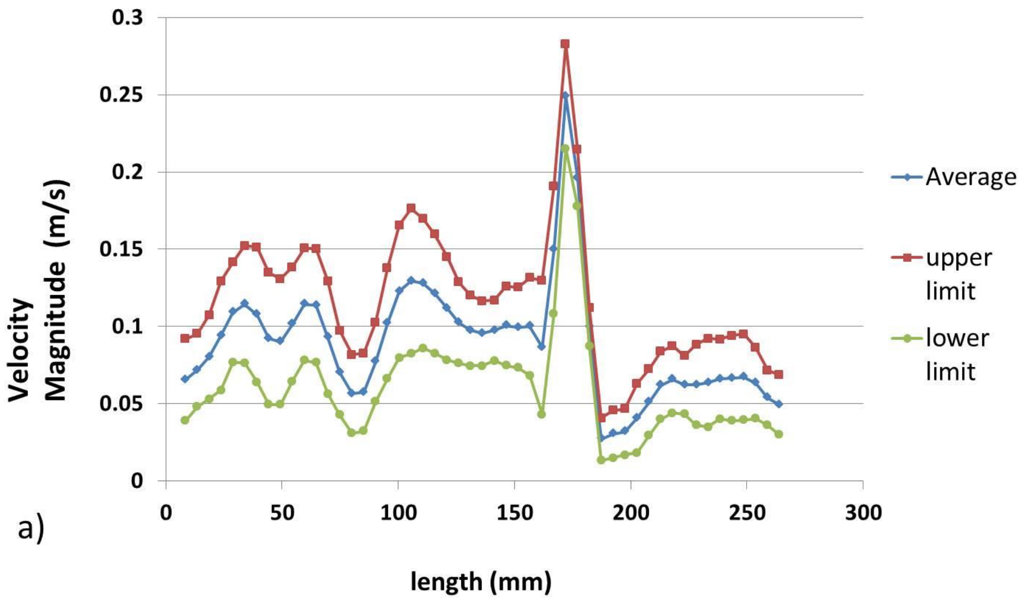

a)

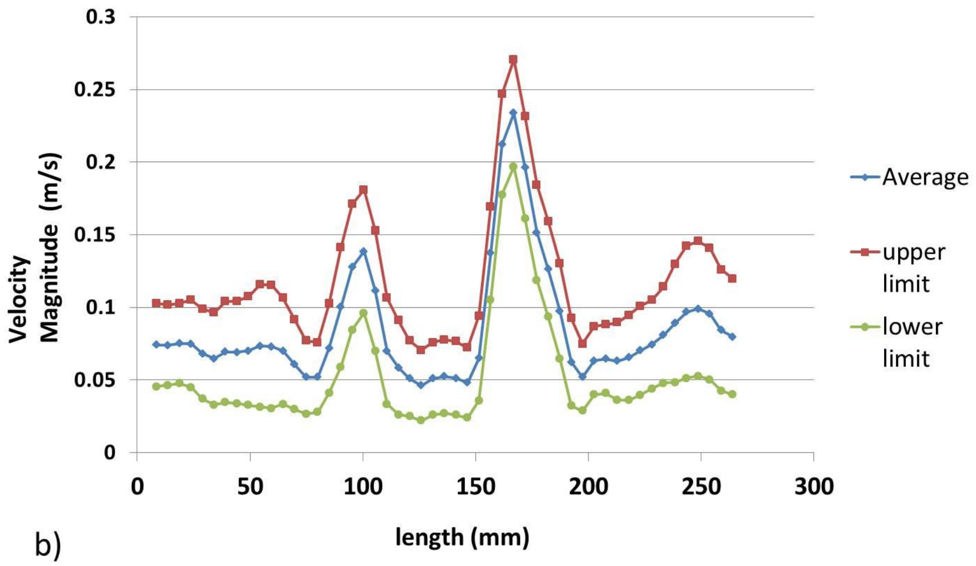

b)

Figure 4.12 Horizontal velocity magnitudes derived from PIV measurements, down the internal and external radii of the mold, at a casting speed of 1.15 m/min, where the upper and lower limits are based on a calculation of the standard deviation. a) Velocity magnitude down the internal radius of the mold. b) Velocity magnitude down the external radius of the mold (meniscus level = 0).

The maximum surface velocities at the bath surface vary from 0.05 to 0.1 m/min approximately, on either the inner or outer vertical lines. Therefore, during the maximum flow distortions, a maximum velocity of 0.1 m/min can be expected in the vortex flows. Figures 4.13a and 4.13b show the velocity magnitudes along the internal and external lines respectively, for a casting speed of 1.6 m/min. Along the inner line, only one large peak is observed, but along the outer vertical line there are three peaks, indicating the complex nature of this flow. However, different to the preceding case, the maximum surface velocities in the inner and outer lines are 0.18 and 0.07 m/s, respectively. The higher casting speed induces a larger number of recirculating free shear flows and acceleration of the fluid coming from the emerging flow located in the outer mold radius side.

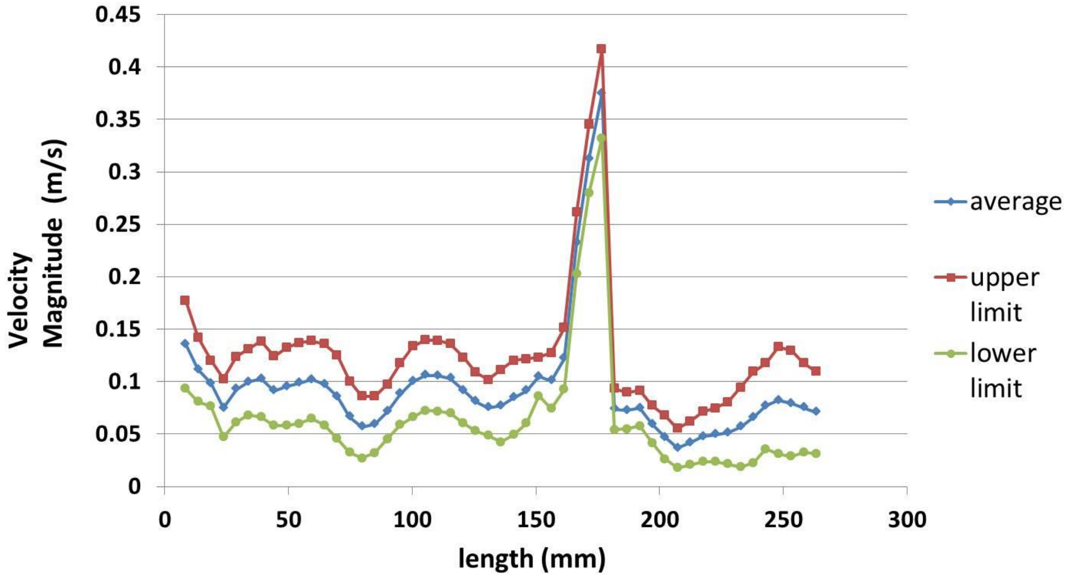

a)

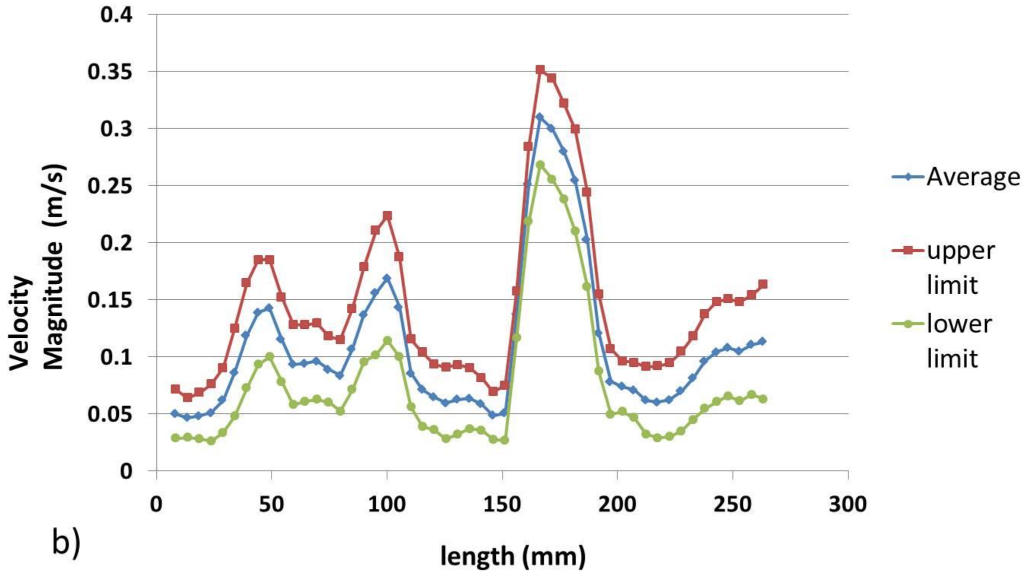

b)

Figure 4.13 Velocity magnitudes from PIV data computed down vertical lines along the internal and external radii of the mold, at a casting speed of 1.6 m/min. The upper and lower limits are based on a calculation of the standard deviations. a) Velocity magnitude down the internal radius of the mold. b) Velocity magnitude down the external radius of the mold (meniscus level = 0).

However, according to the mathematical simulations and the PIV measurements reported up until here, it seems that slag cannot be sucked into the steel, or water, by these rather weak vortex flows, to form MPE defects, as has been observed in the case of slab molds. Nevertheless, these vortex flows do have the ability to shear-strain the metal-slag interface, and to thicken the slag layer in some regions of the mold, at the expense of making the slag layer thinner elsewhere. The thicker slag regions in contact with a dead, or quiet, region of liquid steel below the meniscus, where mushy steel droplets form by freezing, could be expected to entrap mold powder.

4.3.3 Water-oil Experiments

In order to prove, indirectly and qualitatively, this hypothesis, a video of the dynamic water-oil interface motions were recorded with the aid of a fast video camera. A disturbance sequence of the water-oil interface can be observed in Figures 4.14a-4.14e, for different snapshots of the water model, working at a casting speed of 1.6 m/min. Figure 4.14a shows a stable water oil interface at 25.32 s of recording time; at 26.62 s, Figure 4.14b, a disturbance appears in the interface located on the left side, i.e., on the inner mould radius side (as is indicated by the arrow). Fifty milliseconds later, at 26.67 s, in Figure 4.14c, the tail of this disturbance is observed to be in complete contact with the mold surface. Some 130 ms later, Figure 14d and 180 ms later, Figure 4.14e (i.e. at times of 26.80 s and 26.85 s), the oil remains in contact with the mold wall surface, and finally, at 27.12 s (Figure 4.14f) the interface recovers its stability.

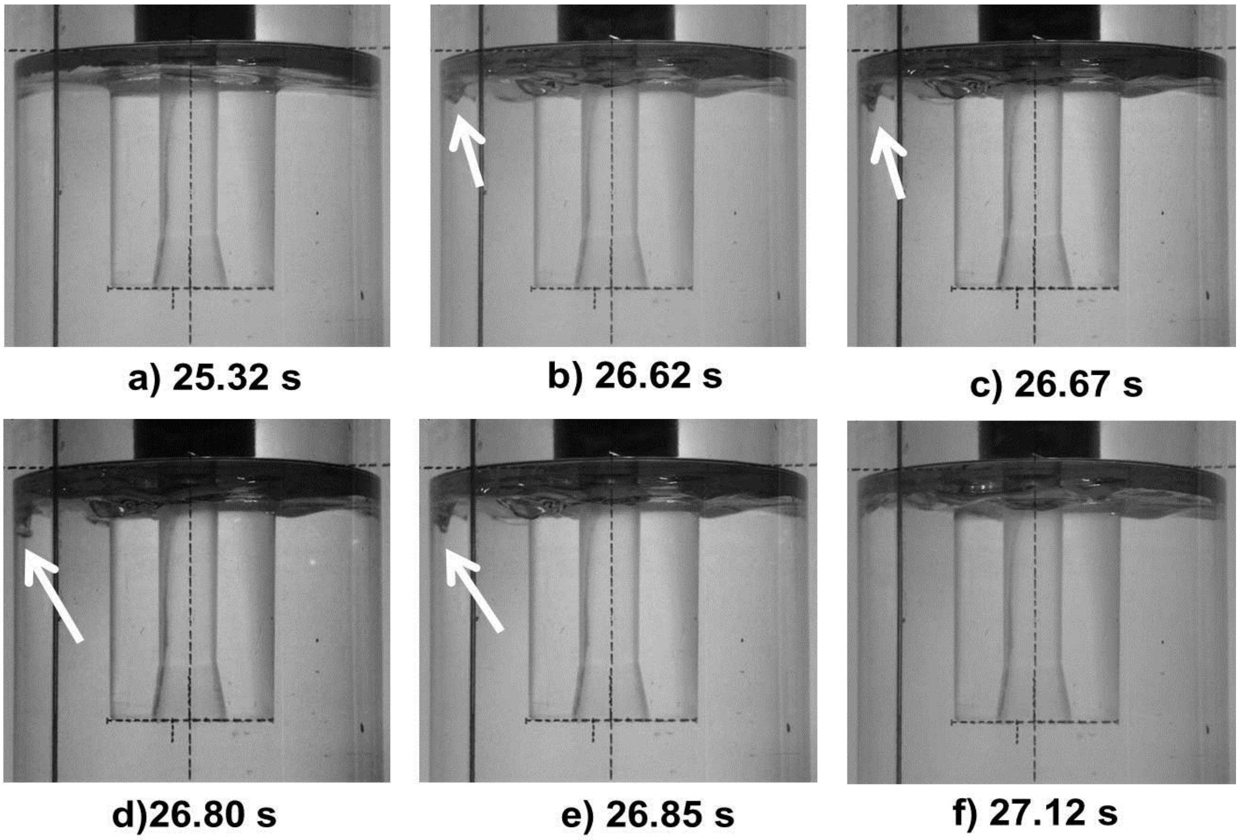

Figure 4.14 Sequence of snapshots showing the interaction between the water and oil in the physical model

An example of a second disturbance can be seen in Figure 4.15a at a time of 53.27 s, when the oil layer becomes thinner in front of the mold and thickens on the right side (indicated by the arrows and numbers 1 and 2 respectively). At an elapsed time of 70.70 s, two vortexes disturb the interface, as seen in Figure 4.15b (indicated by the arrows marked with number “2”). In other regions, the oil layer is thinned (the arrow marked with number “1”). During most of the recording time, the interface looks stable and when those disturbances occur, their lifetimes are less than a second (in this case, approximately 0.5 s). They make intermittent appearances during the entire casting time.

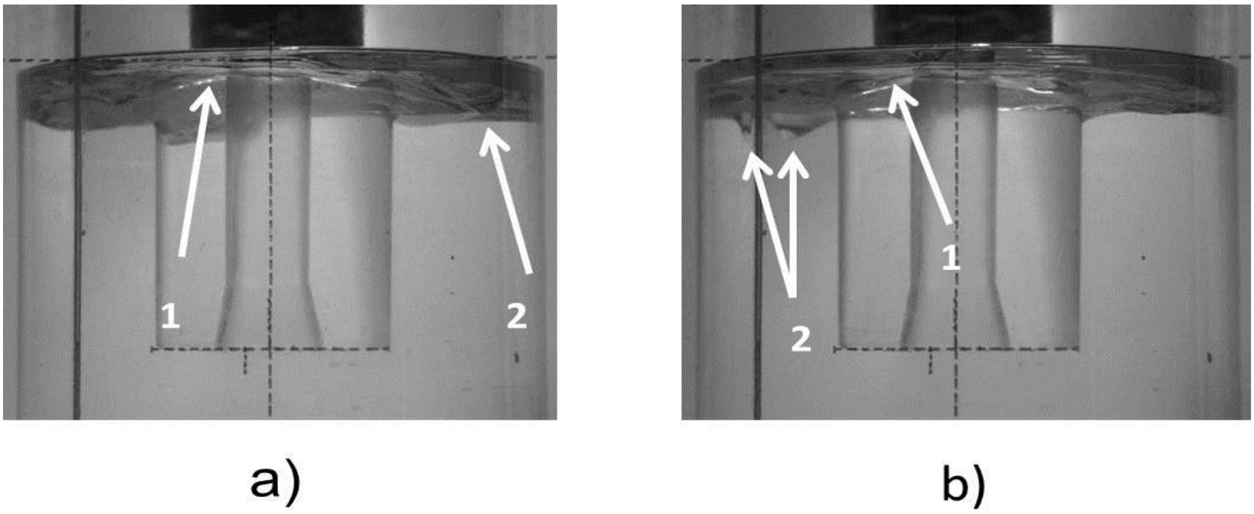

Figure 4.15 Sequence of snapshots showing the interaction between the water and oil in the physical model. a) The oil layer gets thinner on one side (number 1) by thickening the other (number 2). b) A second disturbance showing the thinning of the oil layer on one side (number 1) and two lump formations on the other side (number 2).

It is important to notice that the oil is never entrapped by the direct action of the vortexes since, according to the current results, it is the thickening effects of the oil layer initiated by vortexes which gives origin to the elongated lumps of oil that attach to the mold surface, as previously observed in Figures 4.14a-4.14f. Based on these considerations, it can probably be asserted that slag entrapment mechanisms by steel melts in billet molds, such as shear layer instability, von Karman vortex, a meniscus standing wave, and others [112-114], are not applicable to round billet molds, owing to the very small confined volumes and to the very small surface velocities observed (under 0.10 m/s) at the meniscus level. Rather, complex flows at the metal-slag interface can induce instabilities, including vortices that can lead to regions where the slag layer is very thin, while other regions will have a much thicker slag layer. This thicker layer of slag will penetrate into the liquid steel. Parts can be sheared off, and become entrapped into the forming shell [118].

Beyond these factors, however, lies the question of operating variations in meniscus height during practical casting operations. This has been recognised as a key factor in slab casting operations, and is an issue that remains for further modeling work for billet casting operations.

4.3.4 Multiphase modeling

The VOF method was used in this section to consider the actual multiphase system consisting of steel, slag and air. The properties of liquid steel and the operating conditions for the round mold are summarized in Table 4.2. The details of the VOF modeling procedures were previously discussed in section 3.2.1.

Properties and conditions	Steel (1600°C)
Casting speed (m/min)	1.6
Immersion depth (mm)	123
Steel throughput (ton/min)	0.505
Steel density (ρ_s), $\mathrm{kg/m^3}$	7050
Slag density (ρ_m), $\mathrm{kg/m^3}$	2600
Air density (ρ_a), $\mathrm{kg/m^3}$	1.79e-05
Interfacial tension, (N/m), steel / slag	1.3
Interfacial tension, (N/m), air / slag	0.075
Interfacial tension, (N/m), air / steel	1.6

Table 4.2 Parameters used for the mathematical modeling conditions.

The velocity fields and volume fraction of the phases inside the mold were computed in two vertical planes and one transverse plane for the fluid flow analysis as observed in Figure 4.16.

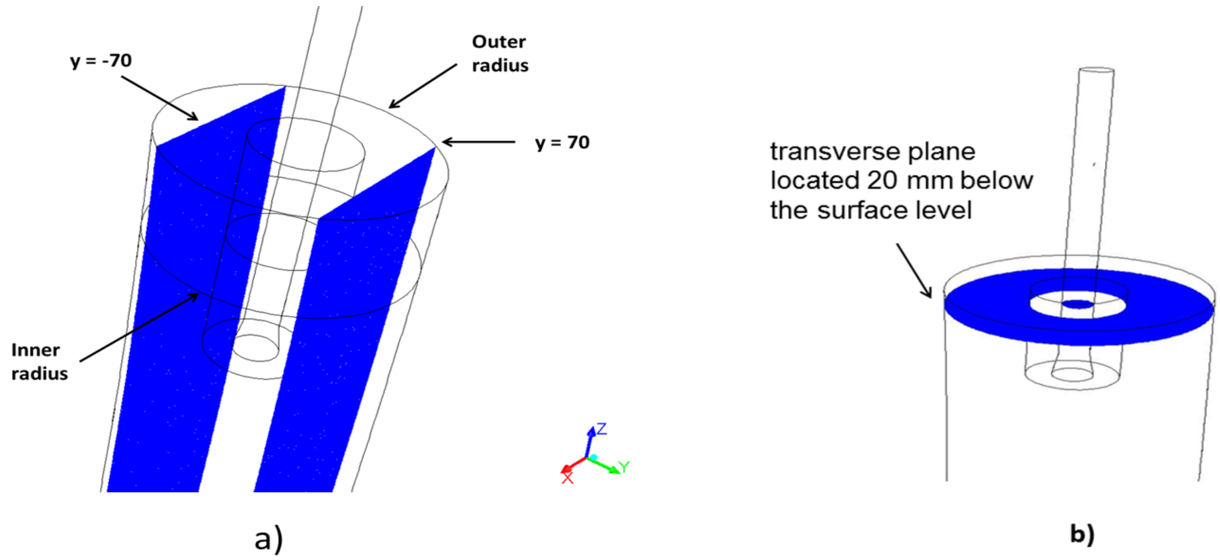

Figure 4.16 a) two vertical planes b) transverse plane located 20 mm below the surface level.

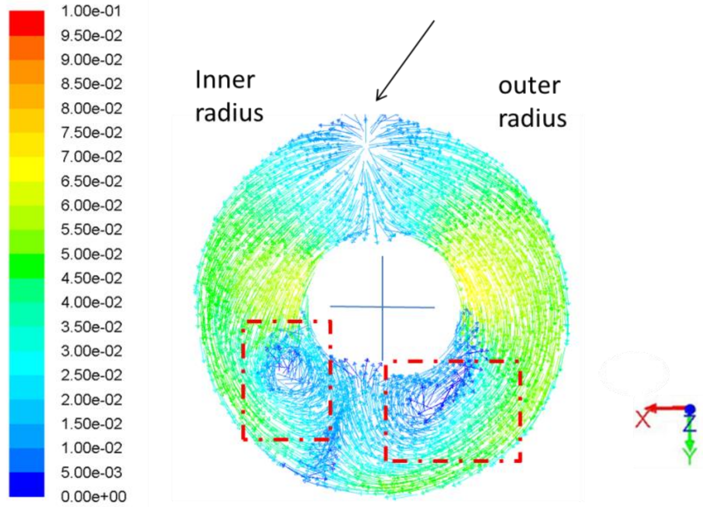

Figure 4.17 Velocity field on a transverse plane of the mold (m/s) located 20 mm below the meniscus at a casting speed of 1.6 m/min.

A similar fluid flow pattern as discussed before for Figures 4.7 and 4.8 is observed in Figure 4.17. However in this case, the multiphase system was considered. At an arbitrary time during the simulation, the emerging flow of liquid steel (in this case, marked by the arrow) takes place at the upper part near the middle point between the inner and outer radii. In the lower part, two low strength vortexes are formed on the opposite side of the emerging flow, similar to the previous cases discussed.

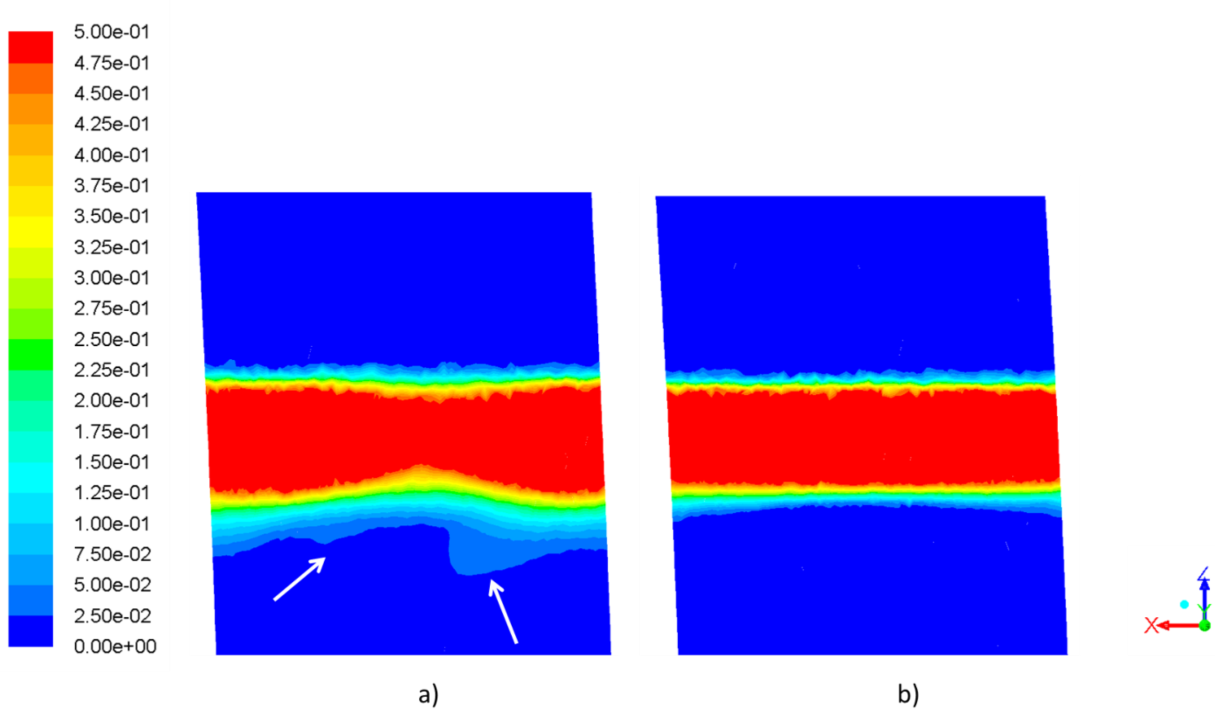

Figure 4.18 Contours of volume fraction of slag computed at vertical planes operating with the straight nozzle. a) Volume fractions from 0 to 0.5 at y = 70. b) Volume fractions from 0 to 0.5 at y = -70.

A distortion in the meniscus is observed in Figure 4.18a. The zones where the slag is dispersed into the liquid steel, marked by the arrows, correspond to the vortexes observed in Figure 4.17. It is observed that the vortex on the right is pulling slag deeper into the liquid steel. On the opposite side of the vortexes, at y= - 70 (Figure 4.18b), a stable steel-slag interface is observed. This stability of the meniscus is provided by zones that lack any vortexes. As explained in the previous sections, the vortexes are not strong enough to detach slag into the liquid steel. However, vortexes that are at a state of constant fluctuation, emerging, vanishing and reappearing in different locations near the walls, can cause MPE if the pulled small particles of slag come into contact with the solidifying steel shell. Moreover, different fluid flow phenomena that interact together with vortex flows in the actual process such as slag rim formation, possible level fluctuations and mold oscillations of liquid steel could expose the solidifying shell to larger volumes of slag. These variables synchronize to give origin to defects related to MPE [67]. The results of the multiphase (steel/slag/air) mathematical model qualitatively match the water-oil experiments.

4.3.5 Mold powder entrainment mechanisms

According to the preceding discussion, the following mechanism for MPE can be proposed; the entry jet forms a distorted toroidal-like vortex, as manifested by the two main recirculating flows existing for the longitudinal plane intersecting the vertical mold as observed in Figures 4.6 and 4.9. The fluid flowing in the outer mold radius side emerges into the bath surface region, and is divided into two flows that surround the nozzle, as observed in Figures 4.7 and 4.8 (by looking at the cross section of the mold, the inner and outer mold radii are located at the left and right sides respectively). Both flows collide somewhere on the inner mold radius side, creating vortex flows in the region of encounter. Depending on the casting speed (i.e., the level of turbulence), the upper flows displace the emerging region of the outer radius flow, and the region where the vortex flows are formed on the inner radius side. This flow pattern leaves a stagnant region in the upper left side of the mold, as can be seen by the mathematical simulations and the tracer mixing experiments. The vortex flows follow an intermittent pattern, but at the moment of their formation, they displace the slag toward the mold wall, thickening the slag layer. The thickened slag layer is unable to infiltrate completely into the gap between the strand and the mold hot face. In this way, the excess flux is entrapped by the mushy steel shell. This mechanism may explain the irregular incidence of flux particles that are found entrapped in the sub-surface of the billet. This MPE mechanism is described in Figure 4.19.

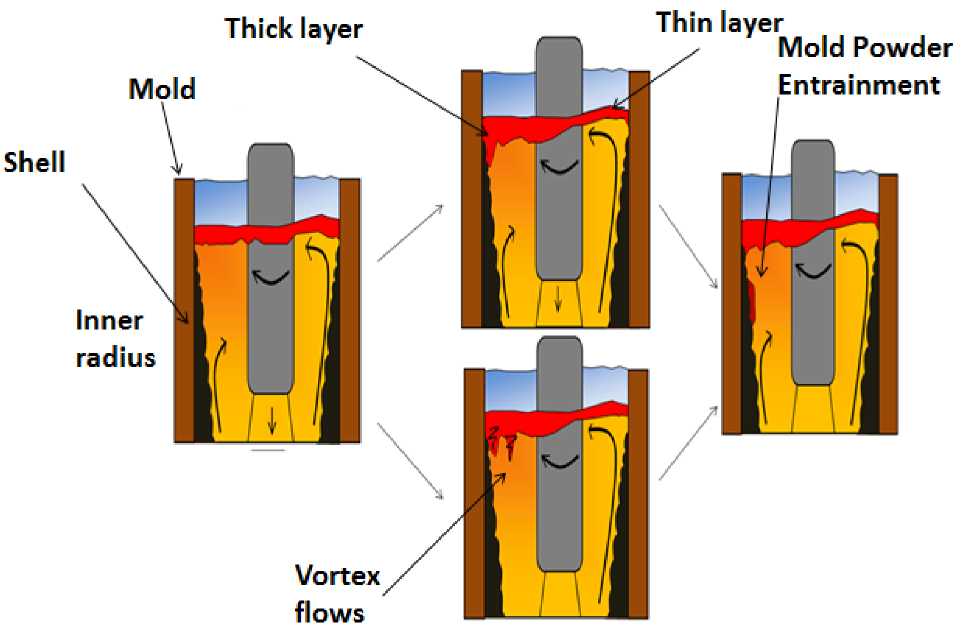

Figure 4.19 Scheme showing the Mold Powder Entrainment mechanisms found in billet molds.

4.3.6 SEN alignment

A misalignment of 2° from the top of the SEN was considered in the following section. Despite the fact that a SEN misalignment toward the inner radius will slightly decrease the mixing time as compared to a perfectly aligned nozzle, the fluid flow patterns predicted remain very similar as can be observed by comparing Figure 4.5 with Figure 4.20a. A very non-uniform mixing of liquid steel is predicted when the nozzle is biased towards the outer radius in Figure 4.20b.

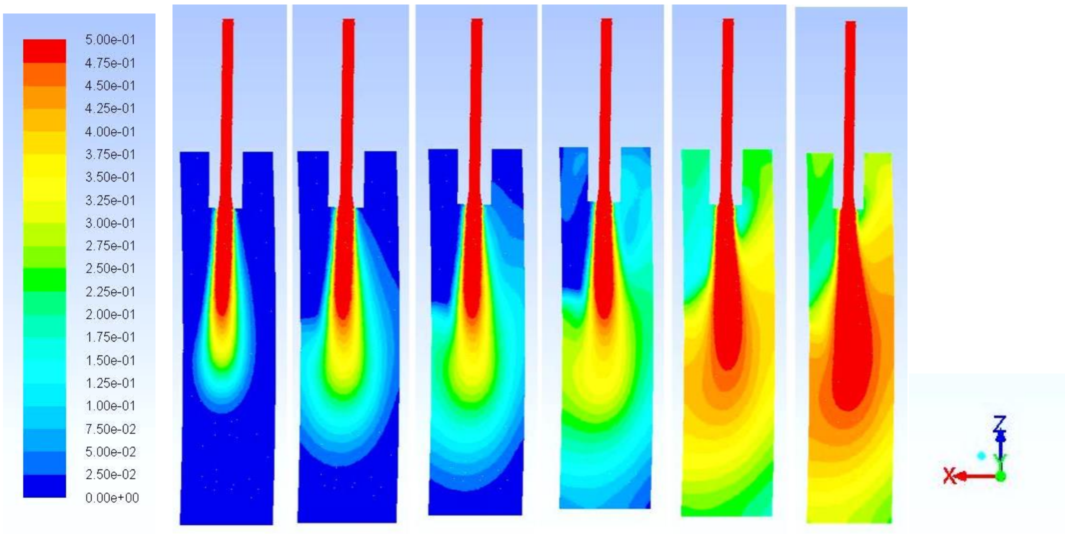

1s 2s 3s 5s 10s 12s

a)

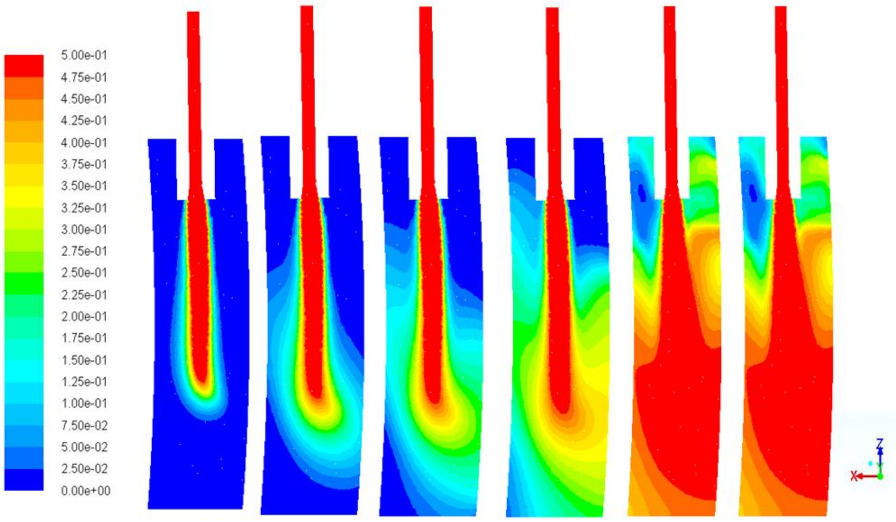

1s **2s** **3s** **5s** **10s** **12s**

b)

Figure 4.20 Scheme showing the mass fraction of tracer at different times predicted by the mathematical model at a casting speed of 1.6 m/min. The darkest region represents a mass fraction of 0.5 to 1. a) Misalignment towards the inner radius by

2° from the top of the SEN. b) Misalignment towards the outer radius by 2° from the top of the SEN.

Thus, the increased distance between the discharging port and the inner radius wall allows for a more even development of upper and lower flows on both sides of the molds when operating with a nozzle biased toward the outer radius. This differs from the previous cases where the emerging flows surround the body of the nozzle. The emerging flows observed along the outer radius in the previous cases are not as strong in this case. The development of large recirculations on both sides of the SEN provides a non-uniform fluid flow throughout the mold cavity. As such, the tracer is not able to reach the free surface rapidly. This leads to larger mixing times near the meniscus region.

4.4 Summary of results

Mathematical simulations and physical measurements to characterize and understand the fluid dynamics of steel entering a round billet mold and its influence on problems related to MPE have been performed. From the present results, the following conclusions can be drawn:

1. The flow pattern inside the mold is asymmetric owing to the slight curvature of the mold, which leads to a stagnant region near the bath surface on the inner radius side.

2. The emerging flow coming from the outer mold radius is divided by the nozzle body near the bath surface. These two flows surround the nozzle and meet in the inner mold radius side, forming complex vortex flows.

3. Based on the present work, the positions of the emerging and vortex flows depend on the casting speed. High casting speeds activate free shear flows acting on both sides of the SEN (as observed from the PIV results) and increase the intensity of the sub-surface vortex flows.

4. The appearance of these vortex flows is intermittent, but their frequency increases with the casting speed.

5. The strength of these vortex flows is not high enough to draw down slag from the molten powder and this is not the entrapment mechanism. Instead, the vortex flows thicken the slag layer (oil layer in the water model) near the mold wall, which produces a penetrating lump of excess slag that can become entrapped by the forming steel shell in an actual mold.

6. The SEN misalignment towards the inner radius slightly improves the mixing patterns. However, asymmetric flows near the meniscus region are not mitigated. The worst mixing was predicted when the nozzle is misaligned towards the outer radius.

5.0 Mold Powder Entrainment in a Square Billet Mold

5.1 Introduction

The aim of this section was to determine the existence of transitory-intermittent flows and to gauge their influence on the generation of mold powder entrapment (MPE); such defects are usually found in the casting operation of square billets at RTFT. For that purpose, in the present work, fluid flow characterization was performed in a square billet mold, using a five ported nozzle consisting of 4 lateral ports and a single port located at the bottom of the SEN, while EMS practices are not employed in the current arrangement. The four ports of the SEN direct flows towards the corners of the square mold. Physical models and mathematical simulations were used, as explained in the following sections. At the end of this chapter, the effects of a misaligned nozzle on the fluid flow are discussed.

5.2 Experimental and mathematical modeling procedures

As explained in the previous chapter, physical modeling consisted of PIV measurements, dye injection videography and water-oil simulations. Two casting speeds were considered for the experiments on this section, while the different submergence depths were taken from the level surface, down to the five ported nozzle tip. The properties of the fluid and operating conditions used to conduct the experiments are shown in Table 5.1. The area of interrogation extended from the meniscus down the mold to a depth of 300 mm (see Figure 5.1a). A mirror, set at an angle of about 45° with respect to the vertical plane, was placed on one side of the mold, while the laser gun was located at its front. The laser light sheet from the gun is reflected on the mirror so as to form another vertical laser sheet that coincides exactly with the central axis (y=82.5 mm) of the SEN. Another vertical axis is located 15 mm from the front face of the mold (y=150 mm). The two vertical planes are hereinafter named the central and frontal planes respectively (see Figure 5.1). These two laser sheet planes were used in order to obtain the corresponding instantaneous velocity fields and to analyze the fluid flow at different sections of the mold. At time zero, a slurry of seeding particles (polyamide particles of 20 microns and density of 1.04 g/cm3) were injected into the entry water flow, through the syringe, and the recording time starts to follow the flow dynamics.

Properties and conditions	Water (20°C)
Molecular viscosity (μ), kg/m*s	0.001
Density (ρ), $\mathrm{kg/m^3}$	1000
Kinematic viscosity (v= $^{\mu}/_{\rho}$), $\frac{m^2}{s}$	1.0 x 10^{-6}
Flow rate at steady state (L/min)	39, 59
Casting speed (m/min)	1.3, 2.0
Immersion depth (mm)	133, 200, 220
Steel throughput (ton/min)	0.269, 0.413

Table 5.1 Properties of the water and operating conditions.

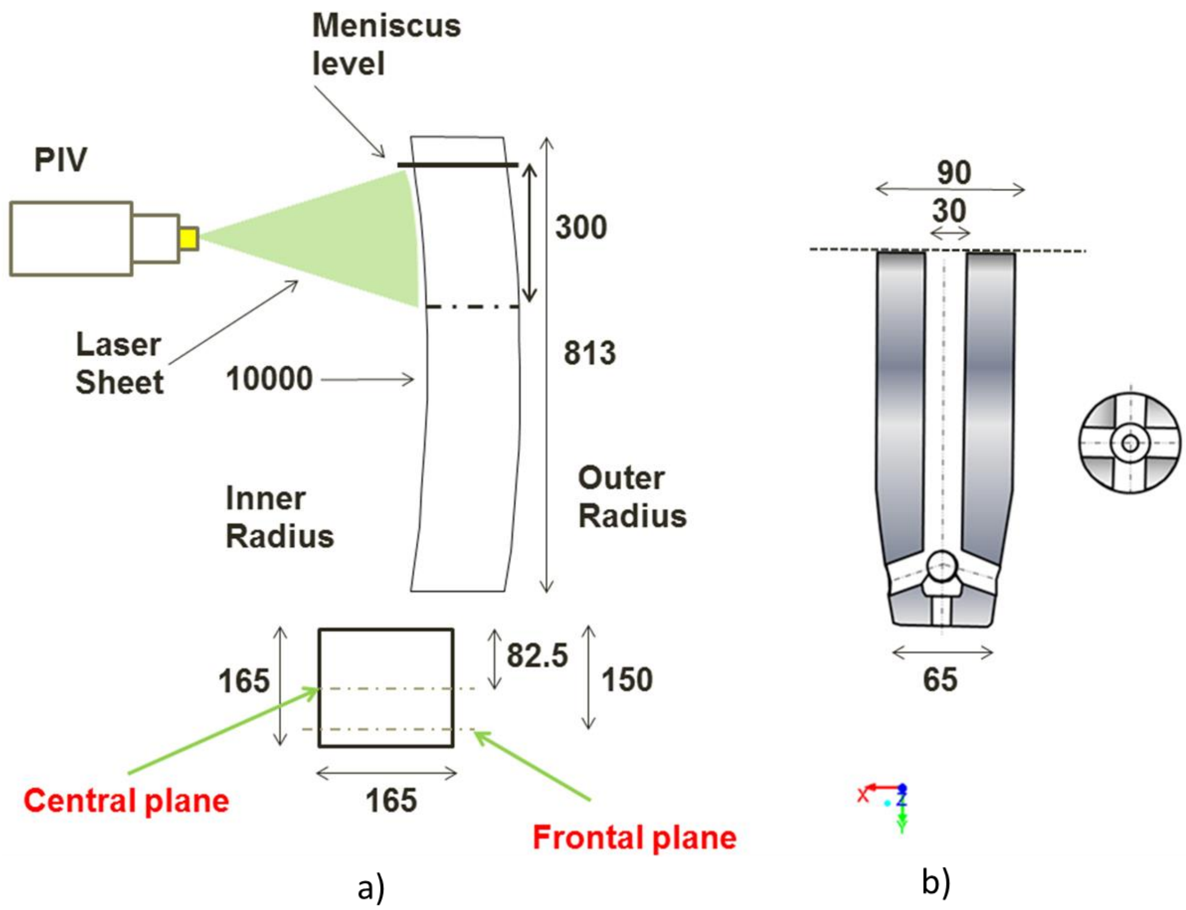

Figure 5.1 Scheme of the square mold and SEN dimensions (mm). a) PIV shooting the laser sheet at two different planes of the mold, in order to compute instantaneous velocities. b) The SEN design.

Single phase mathematical models were considered in this section with the procedures explained in the previous chapter for such cases. The properties of water and same conditions observed in Table 5.1 were applied in the mathematical simulations. The mass fraction changes of tracer and velocity fields inside the mold are computed in the central and frontal planes. The position of the SEN in the mold for the simulations and during the experiments, together with a transverse plane located 20 mm from the meniscus, were all used to compute velocity fields, as can be observed in Figure 5.2.

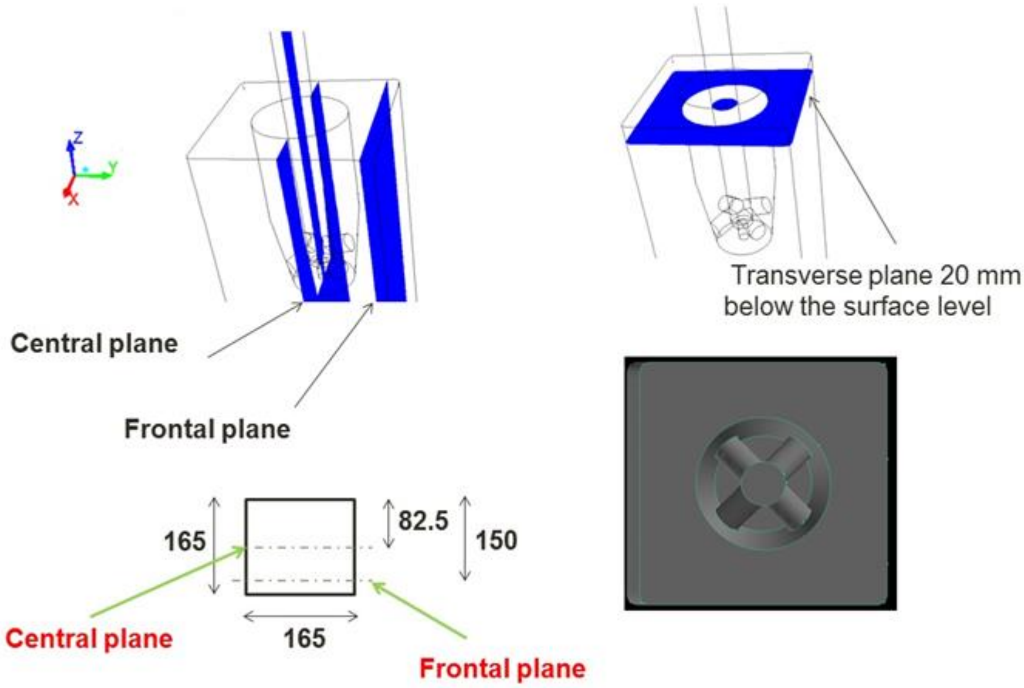

Figure 5.2 Scheme of the square mold and transverse view of the ports' direction. Three different planes are analyzed in the mathematical model.

5.3 Results and Discussion

5.3.1 Flow patterns and mathematical simulation

Figures 5.3a and 5.3b show sequences of tracer mixing at 1, 2 and 3 seconds following dye injection, for a casting speed of 1.3 m/min and for immersion nozzle depths of 133 and 200 mm respectively.

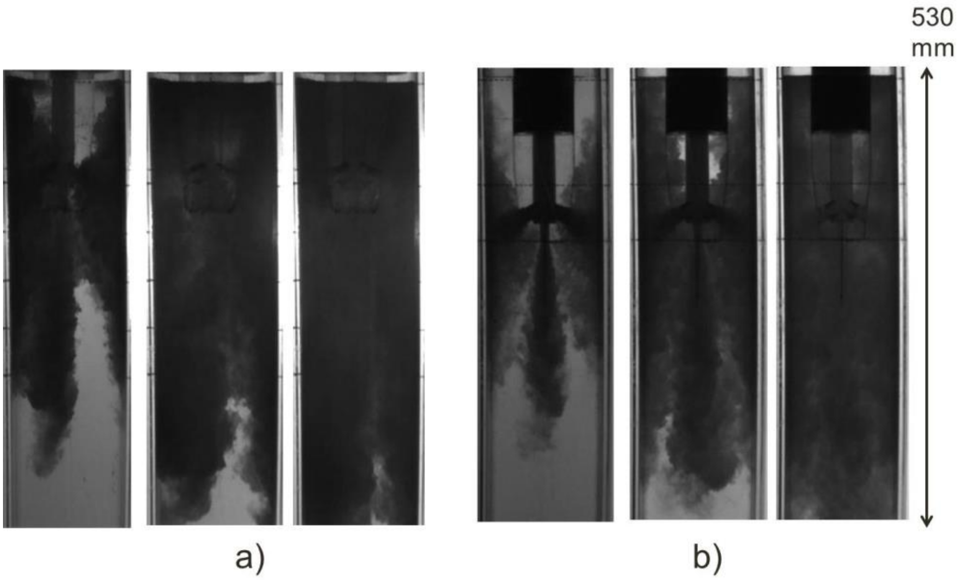

Figure 5.3 Scheme showing the dye mixing patterns at different times after injection at a casting speed of 1.3 m/min. a) at an immersion depth of 133 mm. b) at an immersion depth of 200 mm.

Figures 5.4a and 5.4b show a qualitative comparison between the mathematical and water models where the tracer mixing patterns are computed at 0.4, 0.8 and 1.3 seconds after tracer injection. It is readily apparent that the shallow depth of nozzle immersion induces faster tracer mixing near the meniscus region, than would a deeper position have produced, owing to the larger trajectories in the latter case. As the jets rise along the corners, the mixing is faster near the frontal and back walls than near the center region.

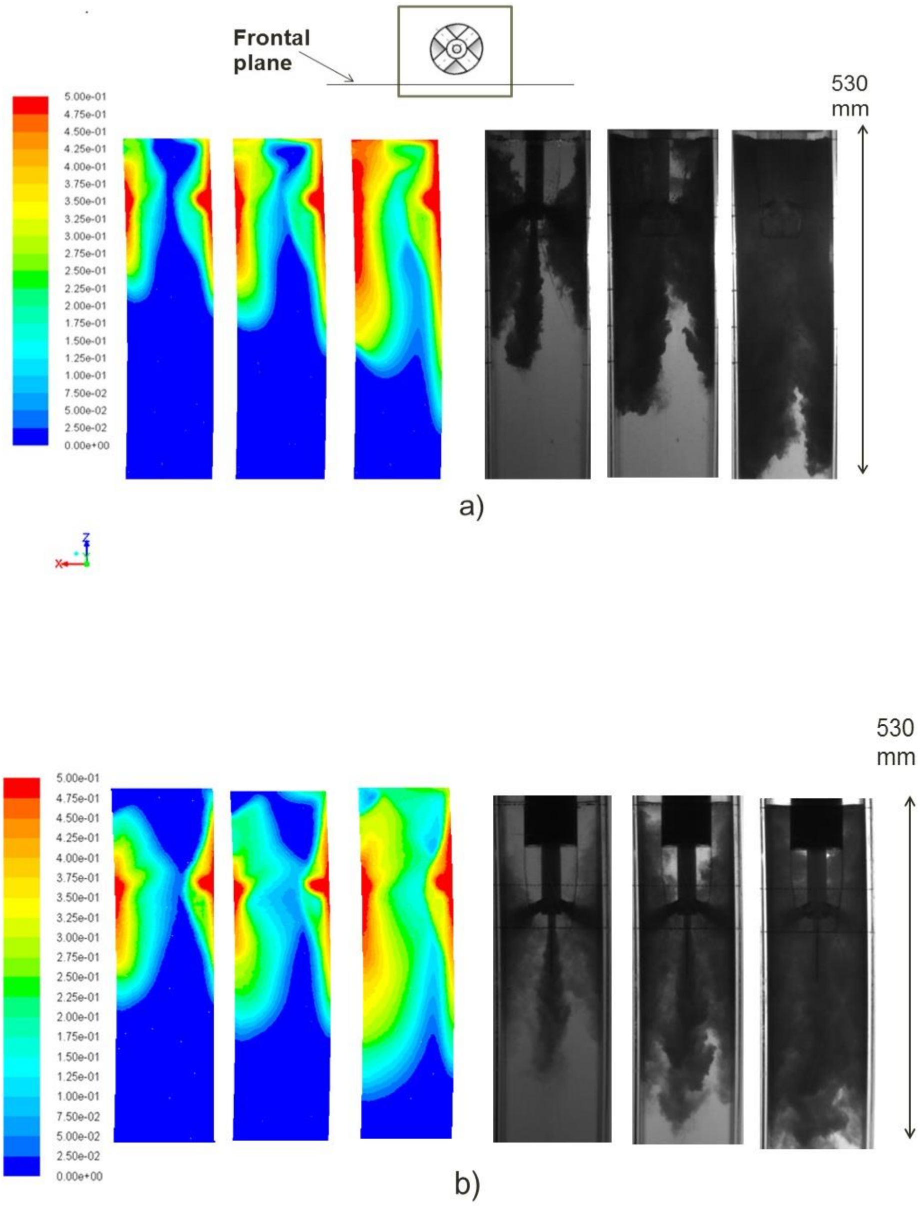

Figure 5.4 Scheme showing the dye mixing at the frontal plane at different times following dye injection at a casting speed of 2.0 m/min. a) at an immersion depth of 133 mm. b) at an immersion depth of 200 mm.

Evidently, the time scale is reduced here compared to the previous case (see Figure 5.3) due to a higher casting speed. Although complete agreement is not observed, considering the mixing characteristics of the tracer between the calculated and physically modeled results, a qualitative similarity is certainly observed among both types of data. It is important to note that the mixing patterns on the experiments correspond to a 2D view of a 3D phenomenon, while the mathematical model was computed for the frontal plane located at a position near the wall of the mold. At a deeper SEN position, the mixing is slightly slower near the meniscus region. Given the fast mixing times, it is assumed that in all cases the meniscus remains hot enough to melt the mold flux properly and to achieve good infiltration between the solidifying steel and the walls of the oscillating mold. The curvature of the mold does not have a strong influence on the fluid flow patterns since a relatively symmetrical view can be observed in the mixing dynamics. Hence, it can be assumed that the heat transfer is relatively uniform near the meniscus region and throughout the mold cavity.

Velocity fields in the frontal plane simulated mathematically under a casting speed of 2.0 m/min and at nozzle immersion depths of 133 and 200 mm are shown in Figures 5.5 and 5.6 respectively at three arbitrary times of 0, 6 and 13 seconds.

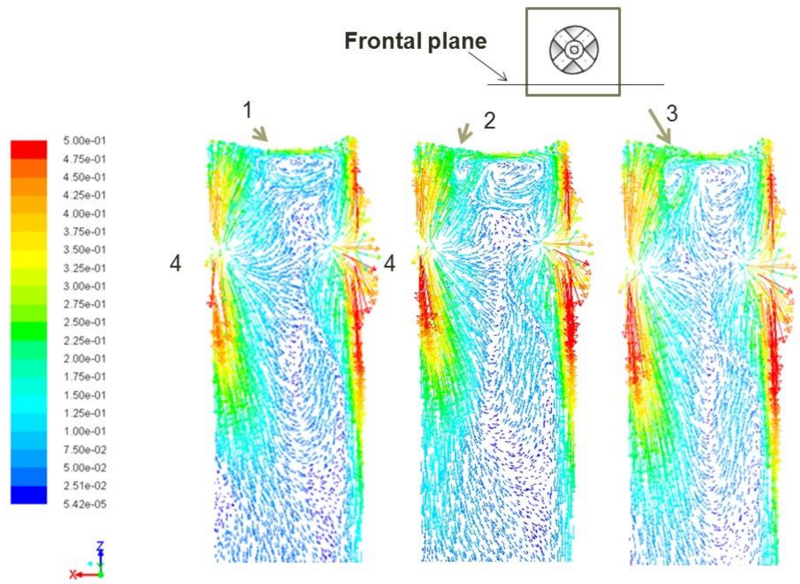

Figure 5.5 Velocity fields on the frontal plane of the mold (m/s) at an immersion depth of 133 mm, and a casting speed of 2.0 m/min.

In Figure 5.5, the numbers 1, 2 and 3 mark the positions of a vortex flow near the bath surface that causes meniscus instability. Meniscus instability is caused by the impingement of the issuing jets impacting on the mold's sidewalls. They enter through the four lateral ports that are directed towards positions near the mold corners. After impinging, marked by number 4, the jets divide into upper and lower streams, in which the first provides momentum to the upper fluid, inducing the previously mentioned meniscus instability. The result of this flow pattern is a permanently unsteady flow of steel inside the mold that can alter the shape of the meniscus at any time. In a deeper nozzle position, shown in Figure 5.6, the meniscus becomes more stable, although, vortex flows remain just below the surface, as indicated by numbers 5, 6 and 7. These conditions provide a flow inside the mold that is slightly less dependent on time. It is also important to mention that the four jets impinge strongly onto the forming steel shell on the walls of the mold. This could erode the shell causing a non-uniform shell growth.

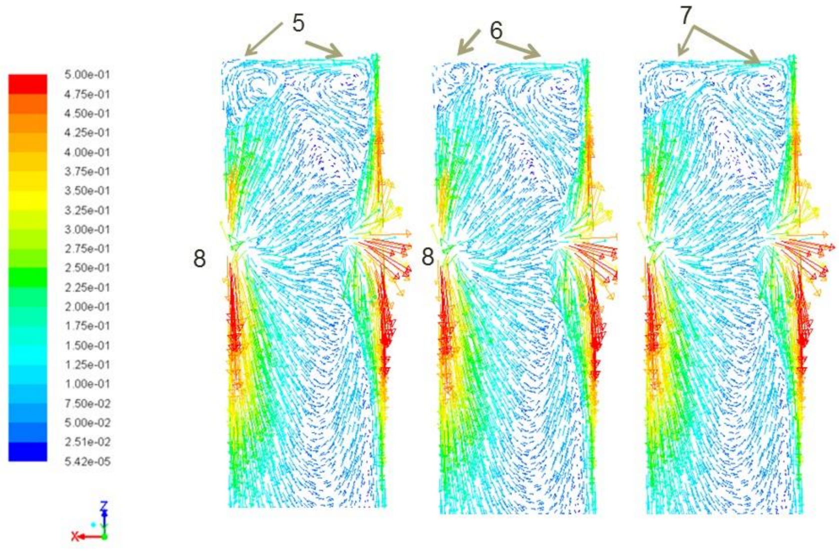

Figure 5.6 Velocity fields on the frontal plane of the mold (m/s) at an immersion depth of 200 mm, and a casting speed of 2.0 m/min.

These two cases are also analyzed through studying the transverse flows near the bath surface in Figures 5.7 and 5.8, for nozzles depths of 133 and 200 mm, respectively. Both cases are separated at three arbitrary times of 0, 5s, l0s and 20s from left to right.

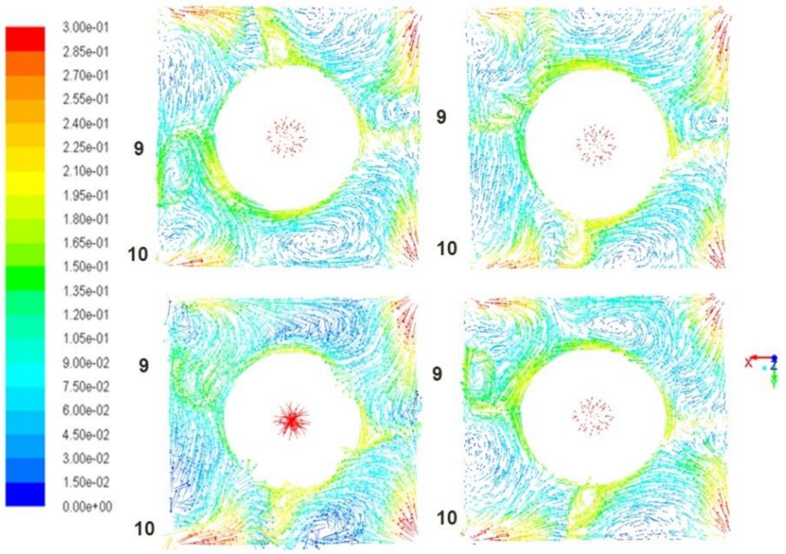

Figure 5.7 Velocity field on a transverse plane of the mold (m/s) located 20 mm below the meniscus, at a SEN immersion depth of 133mm, and at a casting speed of 2.0 m/min.

In the first case, Figure 5.7, an unstable vortex flow can be detected and is marked by number 9. The same phenomenon can be seen in the mold corners, especially that marked by number 10. Vortex flows are also observed on other sides of the square mold. It is worth underlining the large velocity vectors emerging through the mold corners which are actually responsible for transporting momentum to the bath surface, and inducing the previously mentioned meniscus instability. In the second case, shown in Figure 5.8, vortexes are formed with a smaller magnitude and frequency. Nevertheless, this must not be overlooked, since vortex flows are still clearly developed just beneath the bath surface, as was discussed for Figure 5.6.

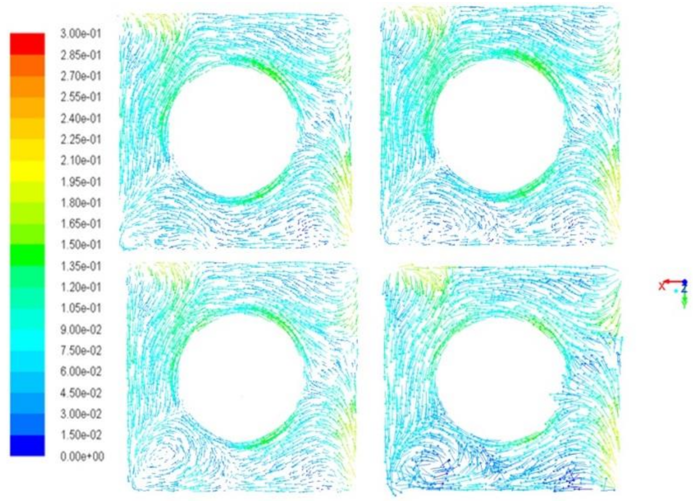

Figure 5.8 Velocity field on a transverse plane of the mold (m/s) located 20 mm below the meniscus, for a SEN immersion depth of 200 mm, and at a casting speed 2.0 m/min.

5.3.2 PIV measurements

The results obtained through the PIV measurements complement all the descriptions so far made through the mathematical simulations. Velocity and vorticity fields for a constant nozzle immersion depth of 133 mm, at two casting speeds of 1.3 and 2.0 m/min, are shown in Figures 5.9 and 5.10, respectively.

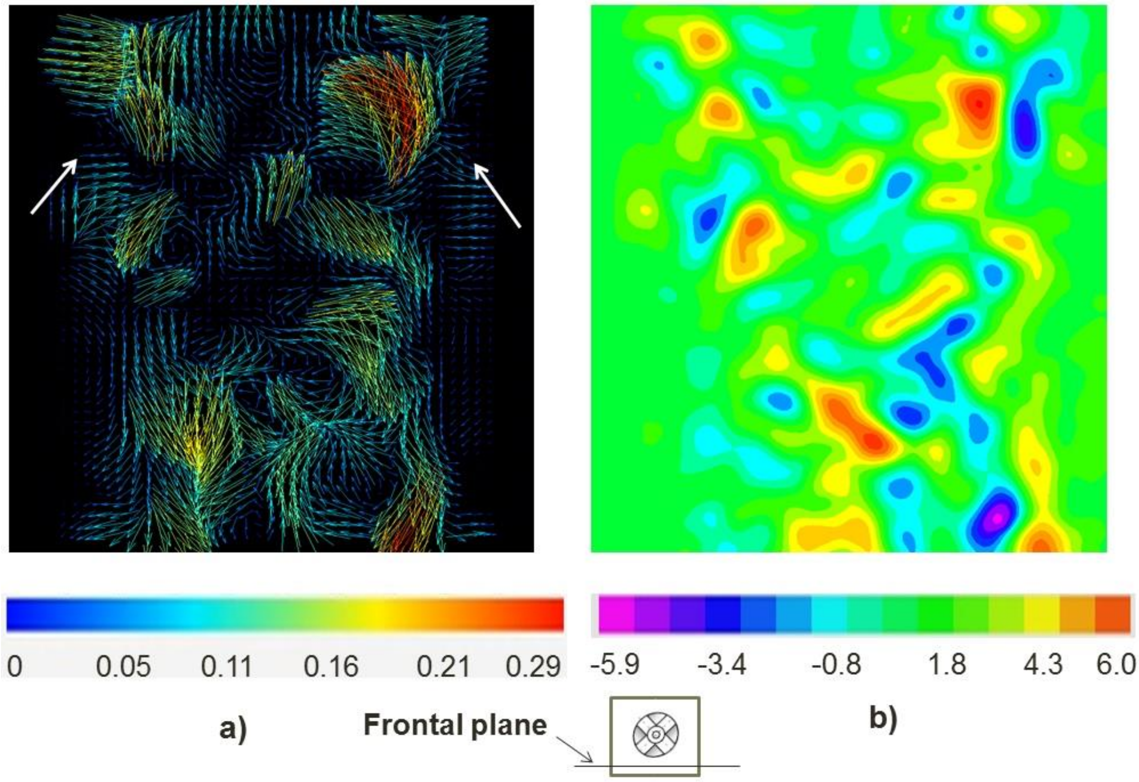

Figure 5.9 PIV and vorticity fields obtained in the frontal plane at a casting speed of 1.3 m/min a) Velocity fields (m/s) b) Vorticity contours (1/s).

The white arrows indicate the impinging region of the lateral jets and the division of those jets into upper and lower flows as seen in Figures 5.9a and 5.10a. Both Figures indicate the generation of multiple vortexes inside the mold, forming free-shear flows. The magnitude of the turbulence is provided by the vorticity fields shown in Figures 5.9b and 5.10b. Vorticity magnitudes in the second figure are double those observed in the previous example at a lower casting speed. Many vorticity islands are observed in the rest of the flow inside of the mold, indicating that the flow patterns do not remain fixed with time.

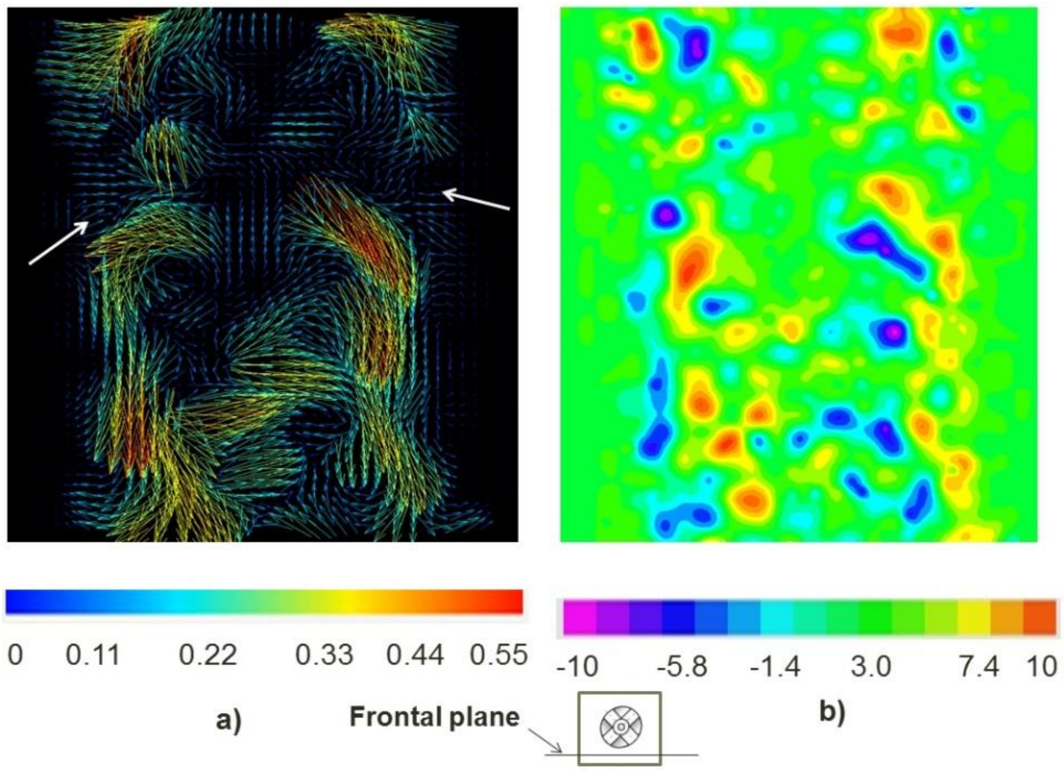

Figure 5.10 PIV and vorticity fields obtained in the frontal plane at a casting speed of 2.0 m/min. a) Velocity fields (m/s) b) Vorticity contours (1/s).

This condition provides for a very unstable flow, particularly near the bath surface. A flow field in the central plane where the nozzle is located is shown in Figure 5.11 for a casting speed of 2.0 m/min at a nozzle depth of 133 mm. In this plane, a completely different picture is observed since the velocities are very small at both sides of the nozzle and the vorticity is essentially concentrated in the central discharging jet. Higher vorticity magnitudes can be observed on the right side, given that the rising flow emerges with more momentum from this side of the mold due to the curvature in its geometry.

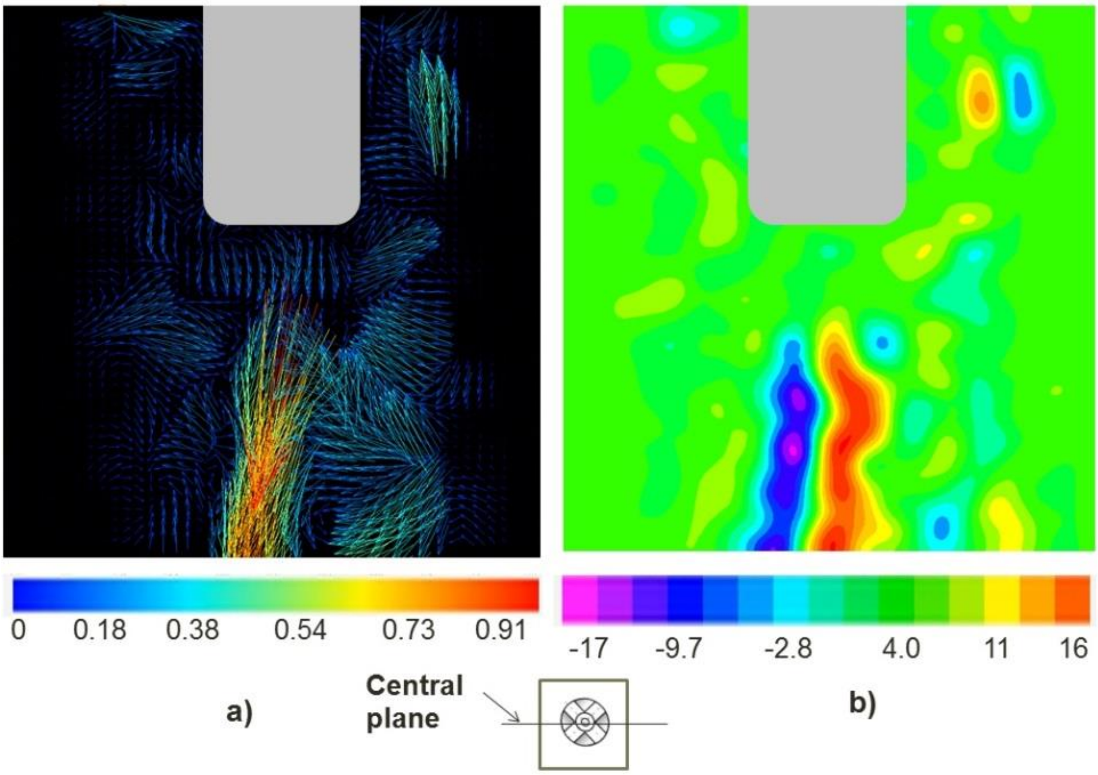

Figure 5.11 PIV and vorticity fíelds obtained in the central plane at a casting speed of 2.0 m/min. a) Velocity fields (m/s). b) Vorticity contours (1/s).

Figures 5.12 and 5.13 show the corresponding velocity and vorticity fields, in the frontal plane, for a nozzle immersion depth of 200 mm and two casting speeds of 1.3 and 2.0 m/min. These two figures show the effects of casting speeds for a deep nozzle position. As can be expected, internal vortex flows remain. It can be said that in spite of the deep nozzle position, highly turbulent conditions prevail, even for the lower casting speed, as can be corroborated through the vorticity maps.

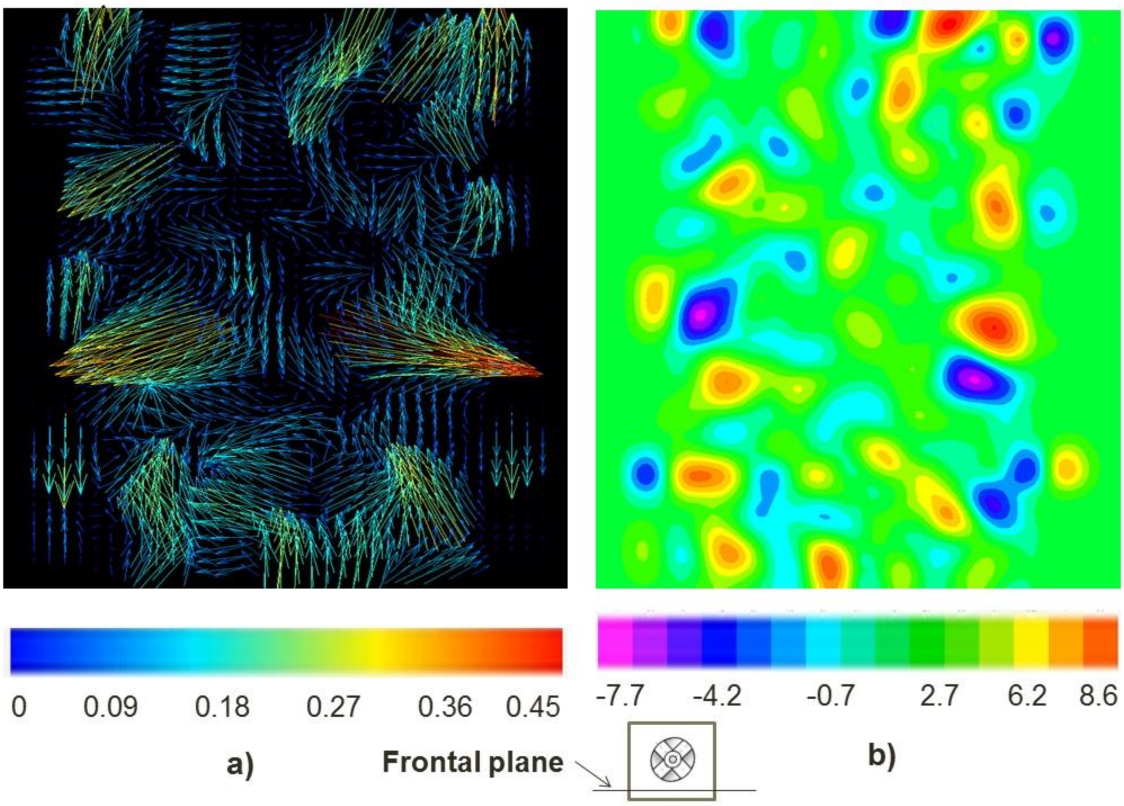

Figure 5.12 PIV and vorticity results obtained in the frontal plane at a casting speed of 1.3 m/min, and SEN depth of 200mm. a) Velocity fields (m/s) b) Vorticity contours (1/s).

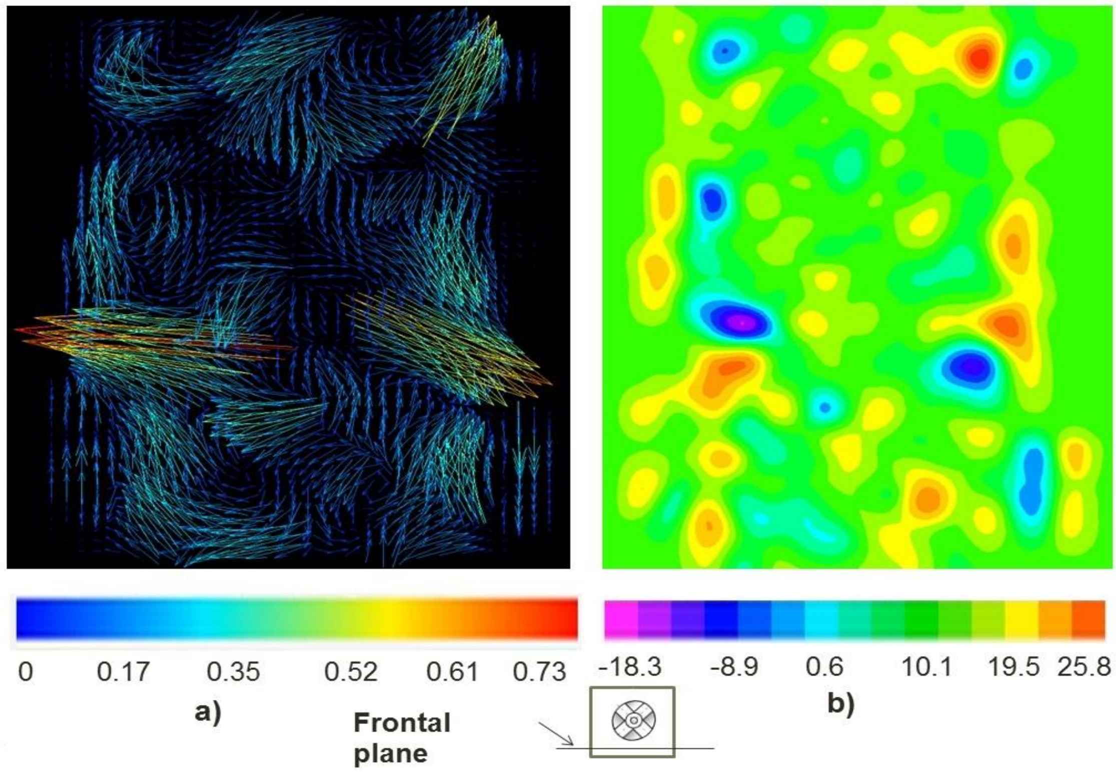

Figure 5.13 PIV and vorticity results obtained in the frontal plane at a casting speed of 2.0 m/min, and SEN depth of 200mm. a) Velocity fields (m/s) b) Vorticity contours (1/s).

5.3.3 Water-oil Experiments

Although oil experiments do not exactly reproduce conditions of flux in the mold, they can be very useful for obtaining a qualitative idea of the effects of such complex flows. Figures 5.14a-5.14c and 5.14d-5.14f show the oil dynamics, at different times, for a fixed nozzle immersion depth of 133 mm and two casting speeds of 1.3 and 2.0 m/min, respectively. At the low casting speed, the oil layer is quite disturbed, and lumps of this fluid are attached to every side of the mold walls. At a higher casting speed, the oil layer is completely removed from the mold corners and is strongly entrained into the mold forming large oil droplets. The strong entrainment tendencies suggest that other MPE mechanisms, which were discussed in section 2.4.1, other than mold level fluctuations are present in this case, given that a complete detachment of oil droplets was observed.

At higher casting speeds (2.0 m/min), Figures 5.15a-5.15f, and deeper nozzle positions, the oil layer forms lumps attached to the mold walls, without any strong entrainment tendencies, but with highly unstable interfaces.

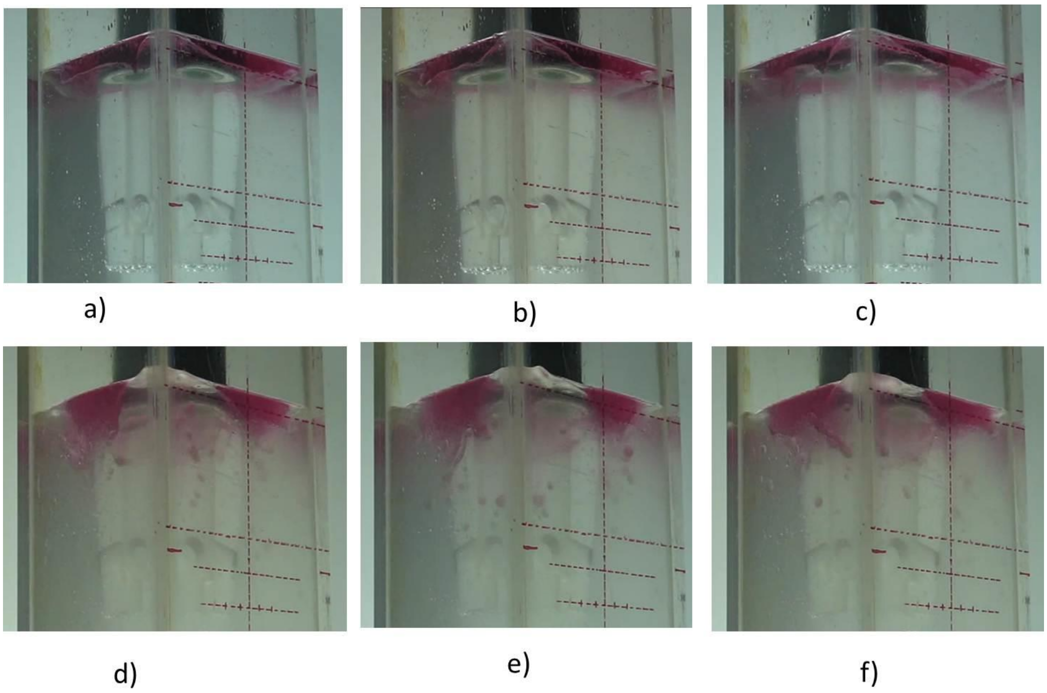

Figure 5.14 Snapshots, showing the interactions between water and oil in the physical model. a-c) at a casting speed of 1.3 m/min. d-f) at a casting speed of 2.0 m/min, for an SEN depth of 133 mm.

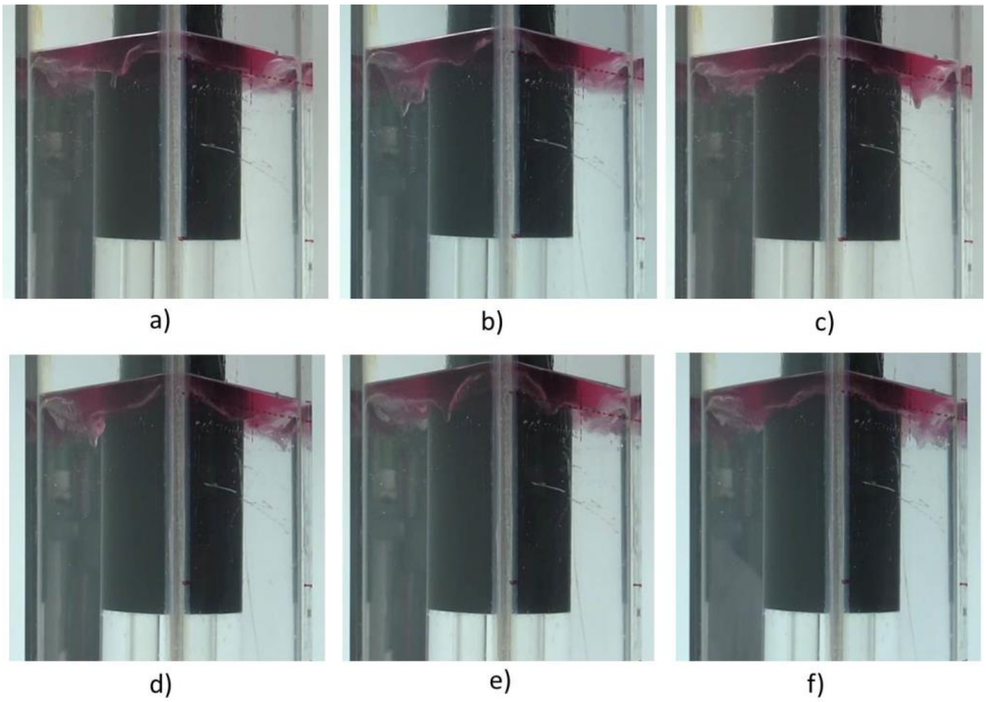

Figure 5.15 Snapshots showing the interactions between water and oil in the physical model. a-c) at a casting speed of 1.3 m/min and SEN immersion depth of 200 mm. d-f) at a casting speed of 2.0 m/min and SEN immersion depth of 200 mm.

5.3.4 Multiphase modeling

The VOF method was used in this section to consider the actual multiphase system consisting of steel, slag and air. The properties of liquid steel and the operating conditions for the square mold are summarized in Table 5.2. The details of the VOF modeling procedures were previously discussed in section 3.2.1.

Properties and conditions	Steel (1600°C)
Casting speed (m/min)	2.0
Immersion depth (mm)	200
Steel throughput (ton/min)	0.413
Steel density (ρ_s), $\mathrm{kg/m^3}$	7050
Slag density (ρ_m), $\mathrm{kg/m^3}$	2600
Air density (ρ_a), $\mathrm{kg/m^3}$	1.7894e-05
Interfacial tension, (N/m), steel / slag	1.3
Interfacial tension, (N/m), air / slag	0.075
Interfacial tension, (N/m), air / steel	1.6

Table 5.2 Properties of the mathematical modeling conditions

The volume fraction of the slag phase inside the mold was computed in two vertical planes for the fluid flow analysis as observed in Figure 5.16.

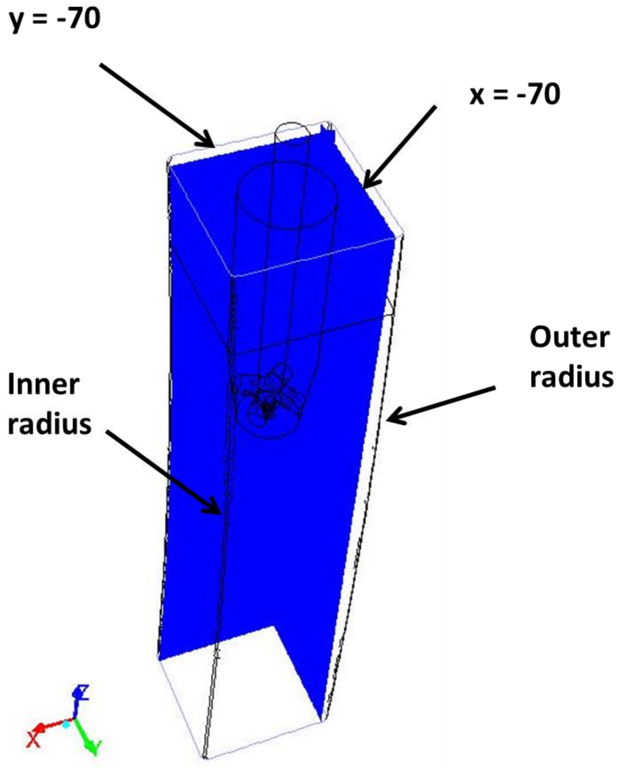

Figure 5.16 a) two vertical planes located at y = -70 and x = -70.

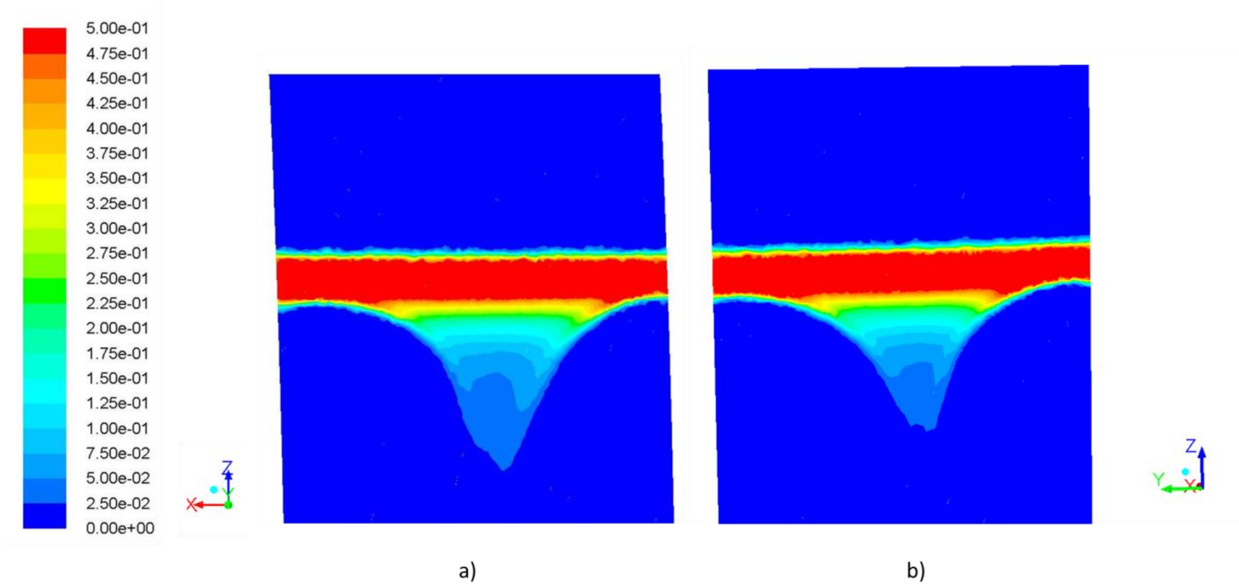

Figure 5.17 Contours of volume fraction of slag computed at vertical planes operating with the five-ported nozzle. a) Volume fractions from 0 to 0.5 at y = - 70. b) Volume fractions from 0 to 0.5 at x = -70.

Similar fluid flow patterns are observed in both planes of Figure 5.17. On these two planes, the slag is pulled into the liquid steel near the center region between the vertical walls of the mold. The solidifying steel shell remains exposed at all times to mold powder, given that the frequency of level fluctuations is constant and the slag deepens near to all four confining walls of the mold. However, this pulling is not strong enough for cutting or shearing lumps of slag into the liquid steel and causing slag entrainment. The different fluid flow phenomena that interact with the constantly pulled slag, in the actual process; such as slag rim formation, possible level fluctuations and mold oscillations of liquid steel, constantly expose the solidifying shell to even larger volumes of slag than those observed in the physical and mathematical simulations. The results of the multiphase (steel/slag/air) mathematical model qualitatively match the water-oil experiments.

5.3.5 SEN alignment

A biased nozzle off the vertical by 2 degrees toward both the inner, and outer, radii was considered in the following mathematical simulations. The effects on the fluid flow of the biased SEN combined with the mold geometry were studied. The tracer through the biased SEN under transient conditions was injected to observe the mixing behavior through the mold volume.

The effects on the mixing patterns for a sequence of 0.4s, 0.8 and 1.3 s following tracer injection when operating with a perfectly aligned and with a biased nozzle toward the inner radius can be observed in Figure 5.18. The tracer mixes slightly faster along the outer radius than its counterpart when operating with a perfectly straight nozzle as can be observed in Figure 5.18a. It is clear that the biased nozzle has a more pronounced effect on the mixing patterns as observed in Figure 5.18b, which results in an even faster mixing of the tracer along the outer radius as compared to the opposite side of the mold.

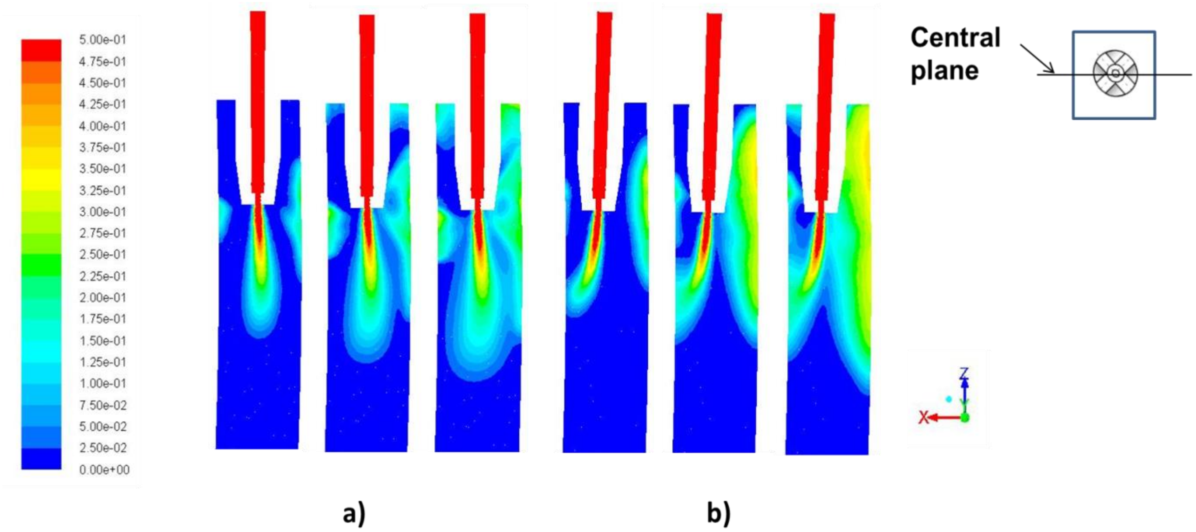

Figure 5.18 Scheme showing the dye mixing at the central plane at different times following dye injection at a casting speed of 2.0 m/min at an immersion depth of 200 mm. a) perfectly aligned nozzle. b) Nozzle biased off the vertical by 2 degrees toward the inner radius.

Similar mixing patterns are observed on the frontal plane in Figure 5.19 where the mixing is faster along the outer radius. A non-uniform mixing of the tracer is also observed in this plane.

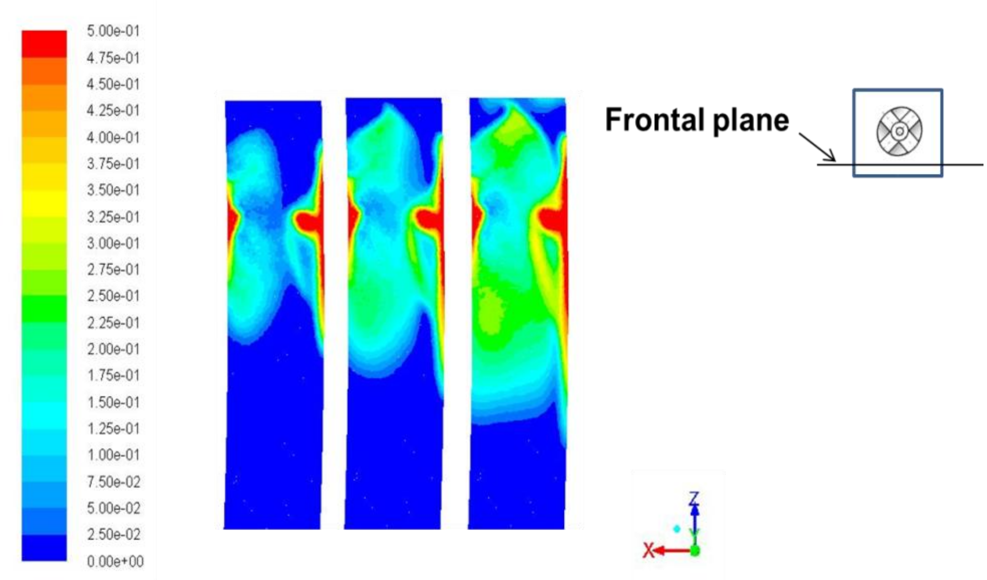

Figure 5.19 Scheme showing the dye mixing at the frontal plane at different times following dye injection at a casting speed of 2.0 m/min at an immersion depth of 200 mm. The nozzle is biased off the vertical by 2 degrees toward the inner radius.

The computed velocity fields for the frontal plane when operating with a biased nozzle are shown in Figure 5.20. Similar fluid flow tendencies as previously discussed for a perfectly aligned nozzle (Figure 5.5 and 5.6) are also found in this case. However, those jets near the corners of the outer radius of the mold extend more on both ways after colliding the mold walls as compared to the jets near the inner radius that are spread shorter distances after collision. Thereby, the tracer is transported faster on this side of the mold as observed in (Figure 5.18 and 5.19).

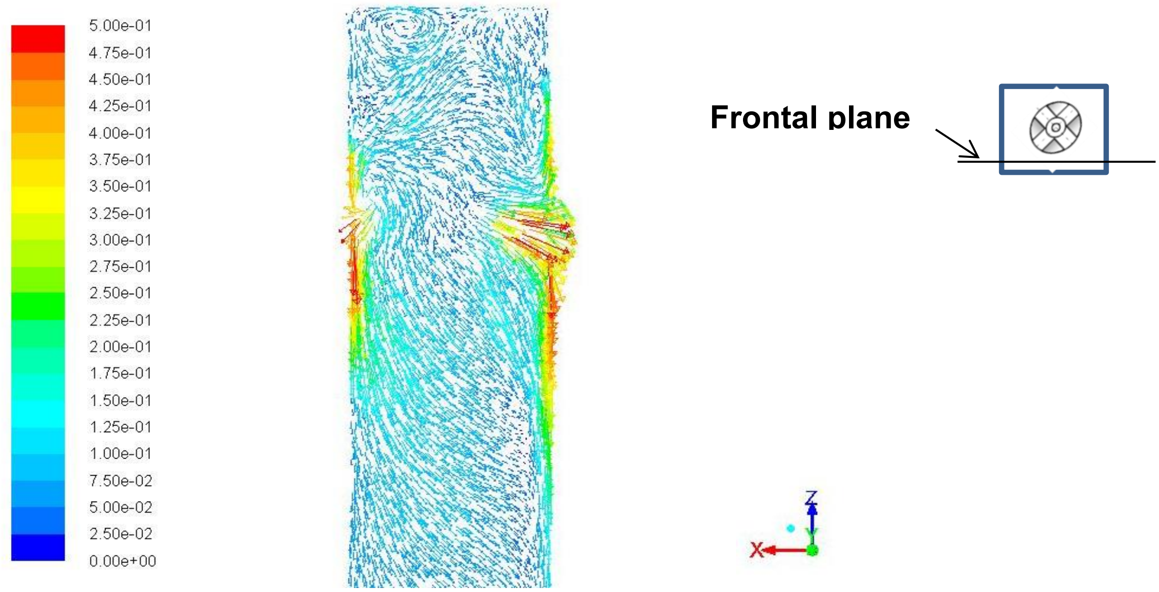

Figure 5.20 Velocity fields on the frontal plane of the mold (m/s) at an immersion depth of 200 mm, and a casting speed of 2.0 m/min. The nozzle is biased off the vertical by 2 degrees toward the inner radius.

The effects on the mixing patterns for a sequence of 0.4s, 0.8 and 1.3 s following tracer injection, when operating with a nozzle biased toward the outer radius; can be observed in Figure 5.21. In both, Figure 5.21a and 5.21b, the tracer is uniformly mixed. The jets extend similarly along each side of the mold on both ways after colliding with the mold walls. This is also observed in Figure 5.22 where the computed velocity fields confirm the symmetric fluid flow patterns. Evidently, a more symmetric fluid flow unfolds when working with a nozzle biased toward the outer radius versus the opposite case previously discussed. The velocity fields and the mixing patterns of the tracer when working with a nozzle biased toward the outer radius are very similar to those encountered in a perfectly straight nozzle operation as discussed in the previous section. Therefore, fluid flow is not significantly affected in this case.

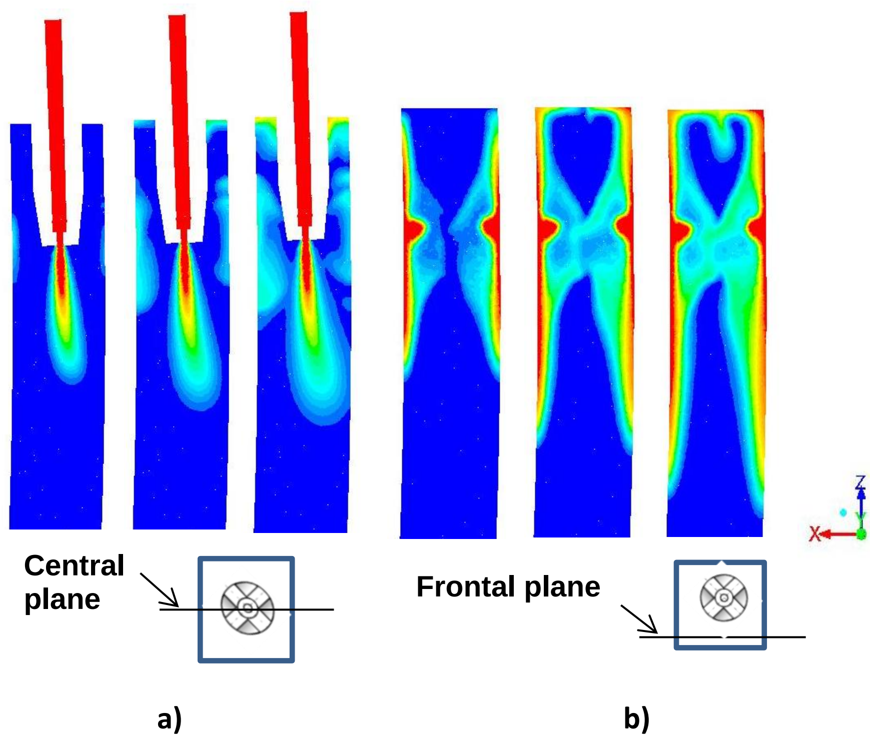

Figure 5.21 Scheme showing the tracer mixing at both, the frontal and central planes at different times following the dye injection, at a casting speed of 2.0 m/min and a SEN immersion depth of 200 mm. The nozzle is biased from the vertical by 2 degrees toward the outer radius. a) Tracer dispersion on the central plane. b) Tracer dispersion on the frontal plane.

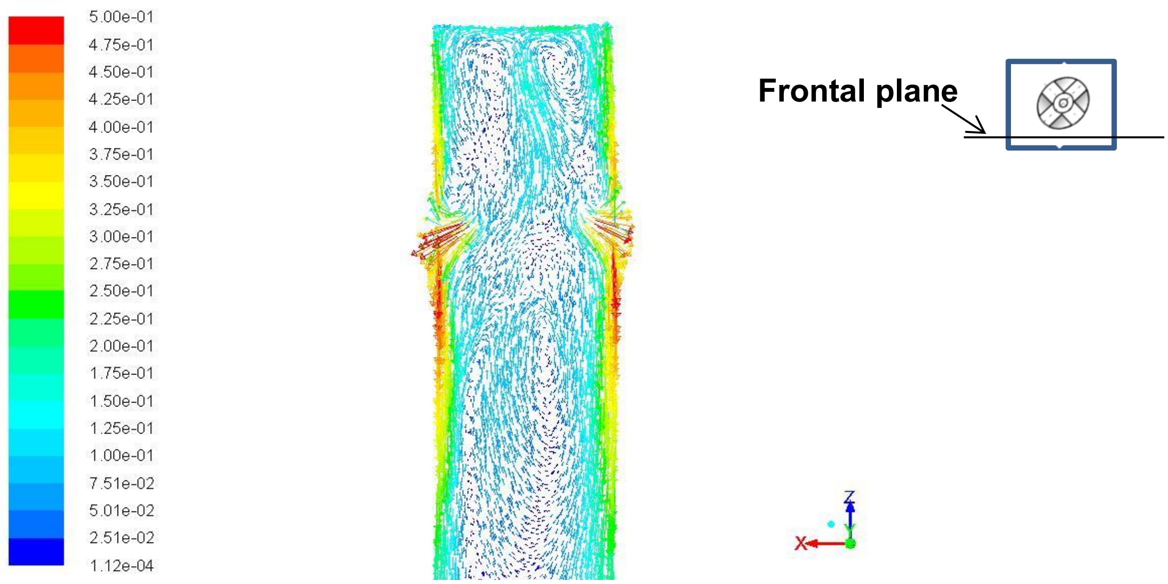

Figure 5.22 Velocity fields on the frontal plane of the mold (m/s) at an immersion depth of 200 mm, and a casting speed of 2.0 m/min. The nozzle is biased off the vertical by 2 degrees toward the outer radius.

An enlarged view of Figures 5.20 and 5.22 near the collision region can be observed in Figure 5.23. In the first case (Figure 5.23a), the jet collides strongly with the wall, with a velocity magnitude close to 0.8 m/s. As the nozzle was leaned toward the inner radius, a reduced space between the discharging port and the wall allows for a strong impingement on this side of the mold. Conversely, the opposite wall is farther from the corresponding discharging port so that the jets impinge on the wall with less force. In the other case, Figure 5.23b, the tilted nozzle toward the outer radius increases the distance between the discharging port and the inner radius wall. Therefore, the jets impinge with similar velocity magnitudes on both walls of the mold. This provides for a more uniform fluid flow throughout the mold cavity.

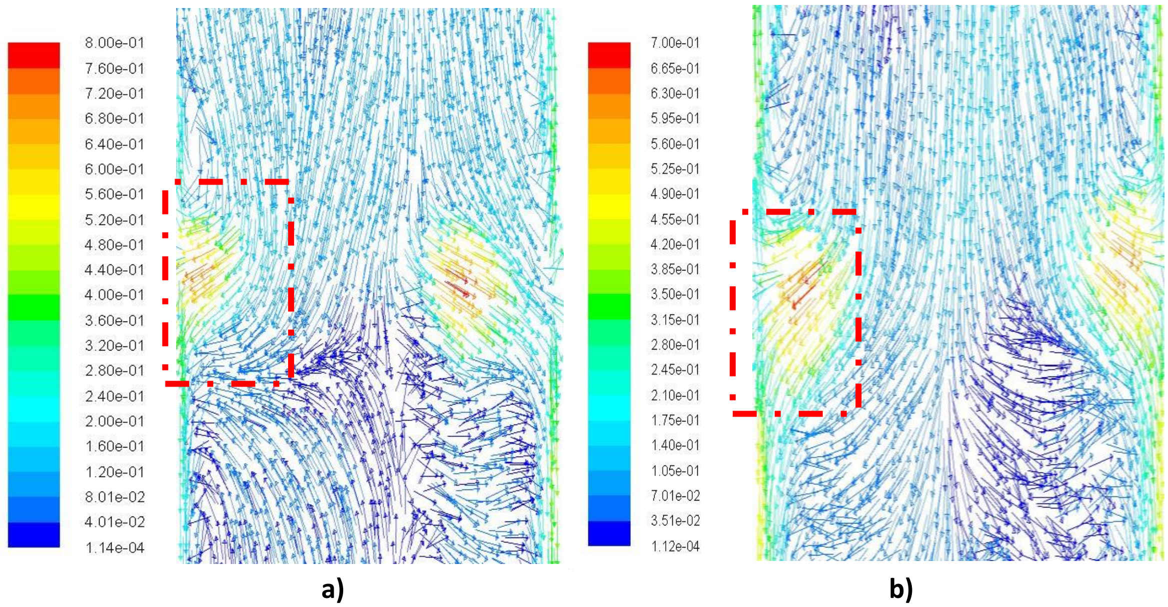

Figure 5.23 Velocity fields on the frontal plane of the mold (m/s) at an immersion depth of 200 mm, and a casting speed of 2.0 m/min. a) The nozzle is biased off the vertical by 2 degrees toward the inner radius. b) The nozzle is biased off the vertical by 2 degrees toward the outer radius.

5.4 Summary of Results

Mathematical simulations and physical models to characterize and understand fluid dynamics and its influence on problems related to mold powder entrainment, MPE, in a square billet mold arranged with a five ported SEN, have been performed for different casting conditions. From these results, the following summary can be made:

1. The flow in the central plane consists of one vertically discharging jet, which induces shear flows to its surroundings but without affecting the rest of the flow too much, since it is directed towards the bottom of the mold.

2. The flow in the frontal plane is highly complex, comprising multiple vortex flows and free shear flows, generating multiple islands of vorticity. The jets emerging from the lateral ports impinge in regions near the mold corners and split into upper and lower flows. The upper flow emerges through the mold corners, providing large momentum transfer that strongly alters the shape of the meniscus interface. Such a condition was practically independent of the nozzle immersion depths and casting speeds considered, since similar flow patterns have been encountered for all the cases [119].

3. The strength of vortex flows is not high enough to suck out slag from the molten powder and this is not the entrapment mechanism when operating at lower casting speeds or deeper immersions as observed in the results delivered by the multiphase mathematical model. Instead, the vortex flows thickens the slag layer (oil layer in the water model) at the mold walls. This gives origin to lumps of slag that overwhelm the pumping action of the oscillating molds and eventually lead to sub-surface entrapment of slag on the steel shell forming in the mold.

4. At a higher casting speed, and a shallow SEN position, the oil layer is completely detached from the free surface. The bath surface is subjected to variable and time dependent shear stresses that help in the oil's distortion, instability and subsequent entrapment. The high surface velocities observed on the physical and mathematical simulations, also indicate that MPE is very likely to happen under these operating conditions.

5. A strong impingement of the four jets onto the forming steel shell on the mold's sidewalls was observed. This could erode the local shell, possibly causing breakouts, and also hampering uniform shell growth.

6. When the nozzle was biased toward the inner radius, the reduced space between the discharging port and the wall allows for a strong impingement on this side of the mold. The magnitude of the impingement velocity could be as high as 0.8 m/s, which is higher than in any other case studied.

7. The short distance between the discharging ports and the inner radius of curvature of the mold also restricts the development of upper and lower flows when operating with a nozzle biased toward the inner radius. However, the opposite happens on the other side of the mold where the upper and lower flows develop rapidly. This contrasting behavior, leads to a non-uniform flow distribution.

6.0 Alternative SEN for Round and Square Billet Molds

6.1 Introduction

In the previous chapters, priority was given toward understanding the current process for the continuous casting of square and round billet molds at RTFT. Fluid flow has been characterized by physical and mathematical modeling tools, in order to understand the possible causes for MPE. After a thorough analysis of the casting process, it was found that the observed vortexes and flow disturbances near the meniscus region, act as the principal triggers for problems related to MPE. Therefore, in this first section, mathematical modeling has been conducted so as to explore and propose a multiport nozzle design that will decrease the magnitudes of the discharging jets, while at the same time, be efficient in maintaining the swirling motions throughout the billet mold cavity. After finding the suitable nozzle with the aid of numerical simulations, a plastic model of the SEN was manufactured and tested in both molds using physical modeling tools.

6.2 Experimental and mathematical modeling procedures

Similar physical and mathematical modeling procedures and conditions were applied as previously explained in Chapter 4 and 5 for the single phase simulations. However, steel was used as the working fluid in the current numerical simulations. The properties of liquid steel and the operating conditions for the round mold are summarized in Table 6.1. It is important to mention that the submergence depth for the multiport nozzles was defined as the distance from the top of the lateral ports to the meniscus.

Properties and conditions	Steel (1600°C)
Casting speed (m/min)	1.6
Immersion depth (mm)	123
Steel throughput (ton/min)	0.505
Steel density (ρ_s), $\mathrm{kg/m^3}$	7050
Kinematic viscosity ($\nu = {}^{\mu}/_{\rho}$), $\frac{m^2}{s}$	0.913 x 10^{-6}

Table 6.1 Properties of the mathematical modeling conditions for the round mold operation

6.3 Results and Discussion

6.3.1 Comparative study between SEN A and SEN B in the round mold

6.3.1.1 Flow patterns and mathematical simulation

The first multiport nozzle tested, hereinafter named SEN A; was the current design used in the bloom industry, which has been proven to induce swirling flows. The nozzle consists of four angled ports oriented 15º downwards. The geometry of this nozzle is observed in Figure 6.1.

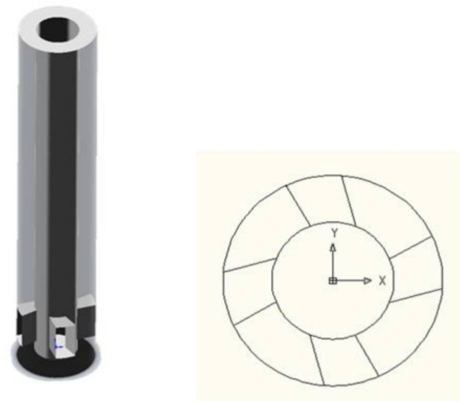

a) b)

Figure 6.1 a) Schematic of the SEN’s used for the numerical simulation. b) Cross sectional view of the SEN A ports.

In Figure 6.2, the discharging jet from each port maintains a straight direction while its magnitude of velocity gradually decreases as it approaches the mold wall. However, a smaller portion of fluid becomes separated from the main flow of the expanding jet. This separation follows a rotational motion around the nozzle in the direction of the angle of the port until this portion of the fluid meets the following discharged jet from the next port, and subsequently, creating a vortex at the point of collision owing to high velocity gradients.

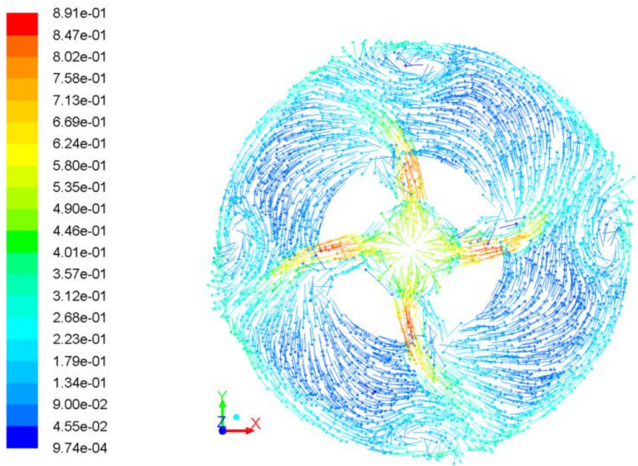

Figure 6.2 Velocity fields in a transverse plane at half height of SEN A (m/s)

The magnitude of the maximum impinging velocity inside the mold was observed at a vertical plane located 25 mm from the centerline of the mold. It coincides with one of the jets only. Similar patterns are observed for the remaining ports. Therefore, only one vertical plane is discussed. In Figure 6.3, it is observed that right after the jets of liquid steel impinge on the mold wall, it is divided into two large vertical recirculations, rotating with opposite directions. Both recirculations are eliminated by horizontal flows as the liquid metal moves forward in the vertical direction. An enlarged view of the enclosing box is observed on the right side of Figure 6.3. The magnitudes of the impinging velocities are found to be in the order of 0.4-0.5 m/s. According to A. Najera [115], an impinging velocity of 0.4 m/s is high enough to affect the uniform growth of the steel shell.

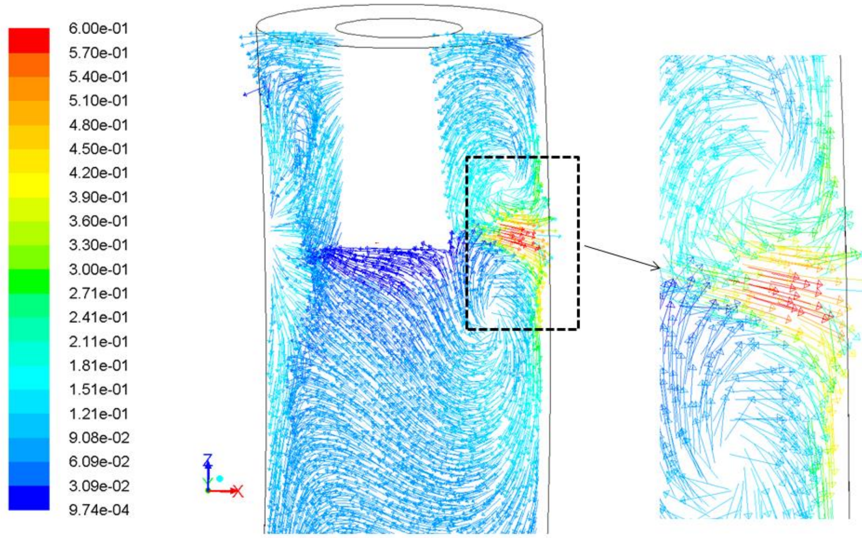

Figure 6.3. Scheme showing a vertical plane, located y = -25mm from the centerline of the mold, operating with the multiport SEN A.

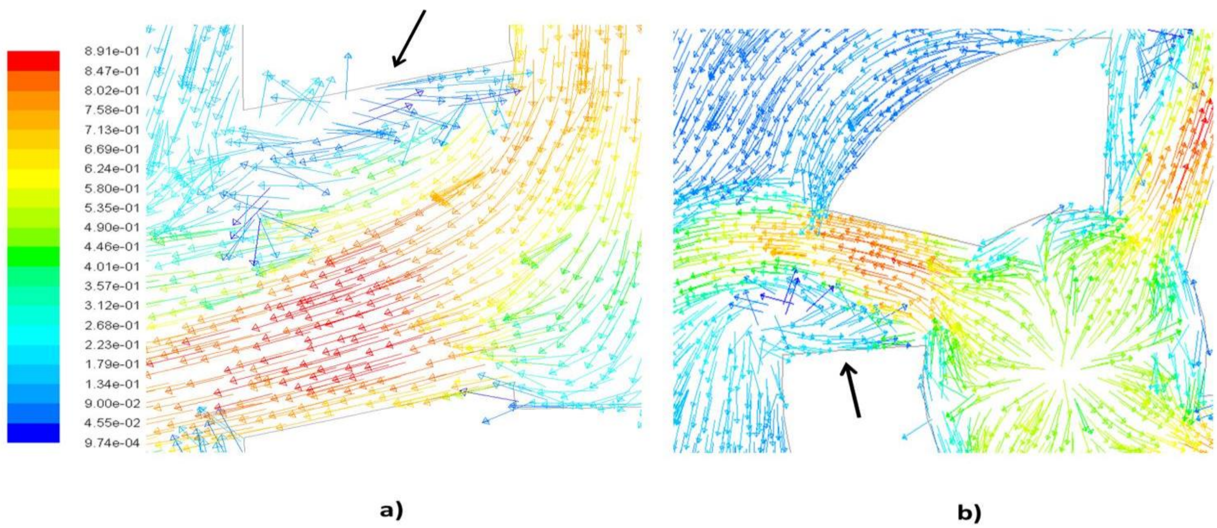

Figure 6.4. a) Velocity field on a vertical plane of the mold (m/s) at the centerline of the port. b) Velocity field in a transverse plane at half height of SEN A.

A closer view of the velocity field inside the port is shown in Figure 6.4. Velocity vectors flowing against the mainstream are observed in the upper part of Figure 6.4a and in the lower region in Figure 6.4b. These regions are marked by the arrows. It is clear that the mainstream, which transports the highest momentum flows, passes through a lower corner without occupying the remaining volume of the port. It can be inferred that a decrease in the discharging velocity is attainable if the geometry of the ports, in addition to producing swirling flows, requires the incoming liquid metal to fill a larger volume of the port. A proposal on the ports design in order to tackle this problem was made by S. Garcia et al. [116,117]. The authors attributed the port backflows to the disruption of the boundary layer triggered by the sharp edge located on top of the geometry of the ports. The upper edge of the ports was smoothed to a curved shape in order to avoid the drastic boundary layer separation. This study was conducted by mathematical models in a nozzle used for a continuous slab casting process. In this research, it was found that the upper radius contributed to the use of a larger volume of the discharging ports. As a consequence, the velocity magnitude of the jets flowing through the ports decreased, and finally resulted in lower bulk flow velocities. The decrease in the bulk flow velocity also reduced meniscus distortion. However, in the current multiport studied, it is observed that two boundary layers are simultaneously disrupted by the top and vertical edges of the port. Therefore, these two edges are smoothed to a curved shape so as to attain the effect described above. These two new features were considered in the geometry of the second SEN design studied, hereinafter named SEN B as observed in Figure 6.5.

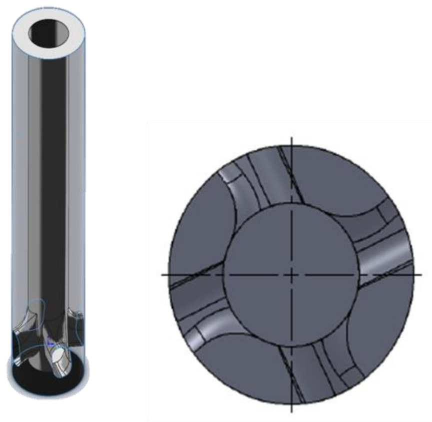

a) b)

Figure 6.5 a) Schematic of the SEN's used for the numerical simulation. b) Cross sectional view of the SEN B ports.

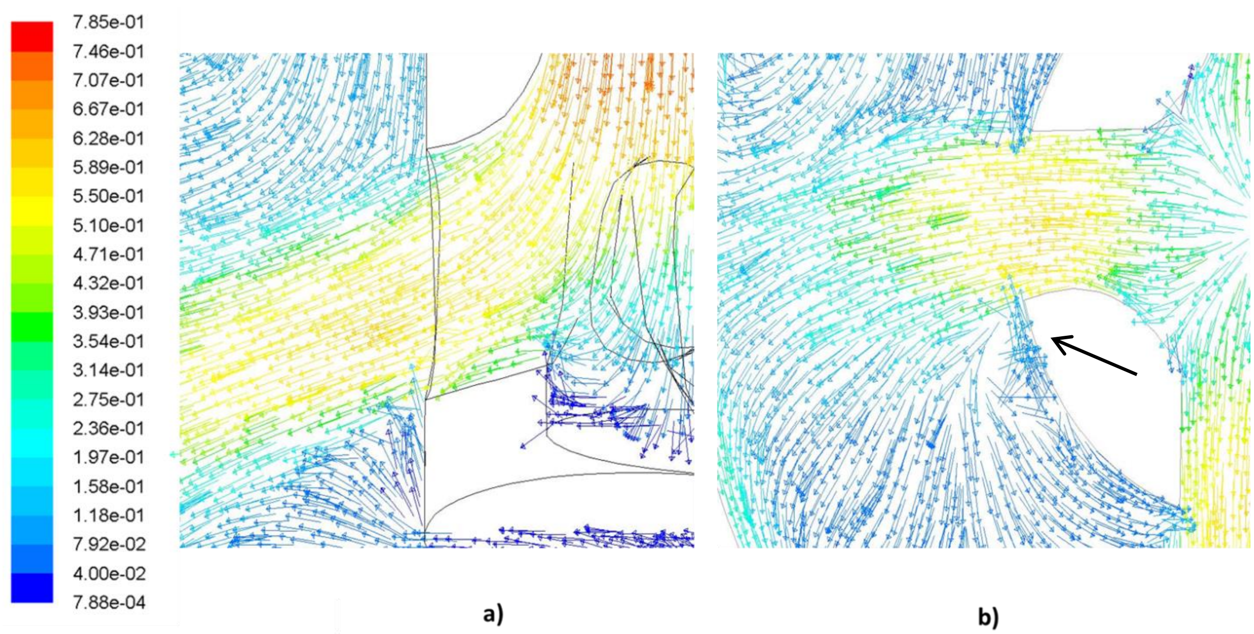

a) b)

Figure 6.6. a) Velocity field on a vertical plane of the mold (m/s) at the centerline of the port. b) Velocity field in a transverse plane at half height of SEN B.

A closer view on the velocity field inside SEN B ports is shown in Figure 6.6. In both Figures (6.6a and 6.6b), the velocity vectors that opposed the mainstream flow, and previously discussed for Figure 6.4, are no longer visible in this case. Rather, the backflows developed in the preceding case were exchanged by velocity vectors that follow the direction of the mainstream. Although a small zone showing backflow is observed as indicated by the arrow (Figure 6.6b), the two radiuses were shown to effectively suppress the backflows. This led to an increase in the volume of the ports filled by the incoming jet of liquid steel. In addition, a decrease in the magnitude of velocity is readily visible through the volume of the port.

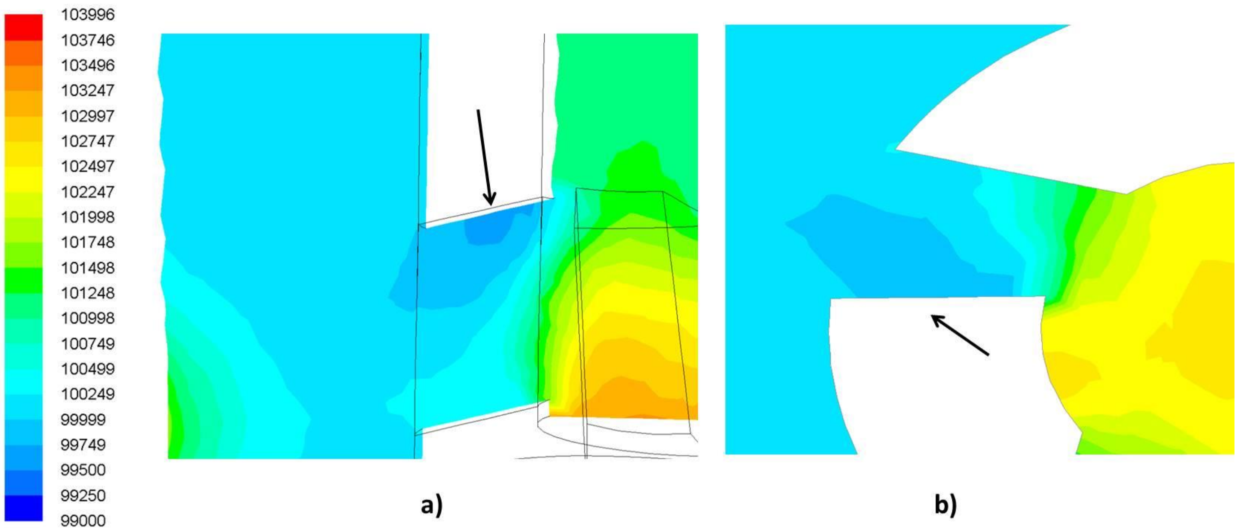

Figure 6.7 a) Contours of pressure (Pa) on a vertical plane of the mold at the centerline of the port of SEN A. b) Contours of pressure in a transverse plane at the mid-height of SEN A.

The mainstream that flows through the lower part of the ports, observed in Figure 6.4a, develops a low pressure zone indicated by the arrow in Figure 6.7a. These low pressure zones invert the direction of the flow, and thereby, create small recirculations and backflows in that region. This low pressure zone can also be observed in Figure 6.7b which corresponds to the velocity field in Figure 6.4b. Although the details of small fluctuations are not captured by the two-equation turbulence models, such as the one currently used in this research, it is expected that the fluctuations of the incoming turbulent jet will affect the filling of the port's volume at all times. Therefore, the effective volume hardly remains constant. The incessant expansion and contraction of the effective volume would also add to the myriad of variables that sustain the transient behavior of the liquid steel throughout the mold's volume.

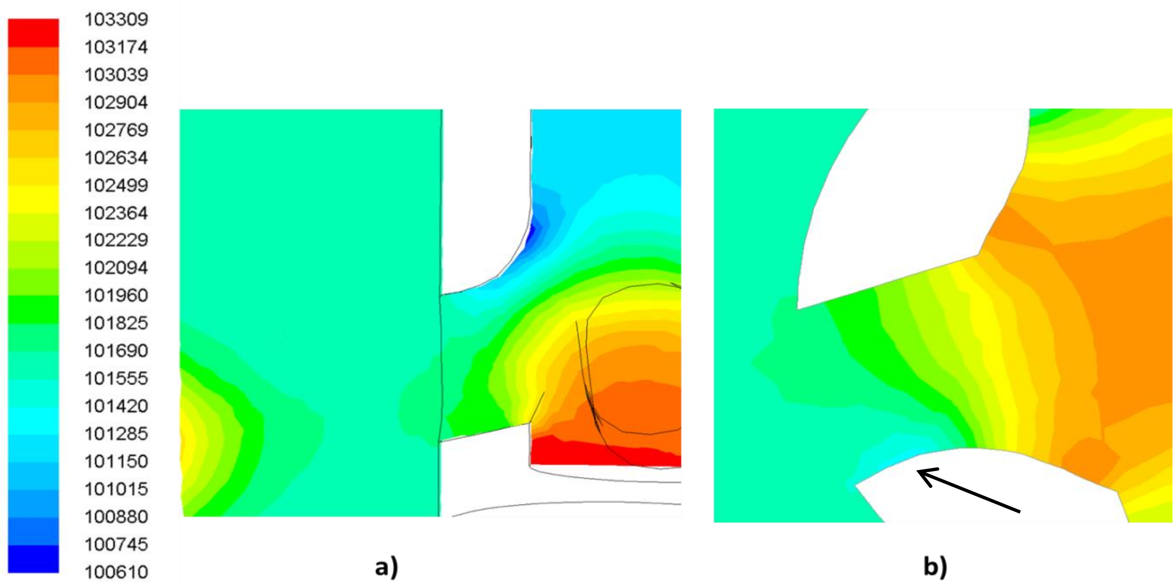

Figure 6.8 a) Contours of pressure (Pa) on a vertical plane of the mold at the centerline of the port of SEN B. b) Contours of pressure in a transverse plane at mid-height of SEN B.

It is observed in Figure 6.8a that the upper radius of the port reduces the steep pressure gradients previously observed in Figure 6.7a. Similarly to the preceding case, the pressure is lower in the upper part of the port. However, the variations in the pressure are not high enough to cause the backflows or restrict the flow of liquid steel through the smaller cross-sectional area near the lower corner of the port. The transverse view observed in Figure 6.8b also shows more gradual pressure gradients than its counterpart in Figure 6.7b. The lower part of the port is also subjected to the lowest pressure zone. It is observed that a low pressure area, indicated by the arrow, is surrounded by regions with higher pressure. This pressure gradient induces the backflows discussed in Figure 6.6b. However, the backflows observed in this case are weaker compared to those results delivered by SEN A.

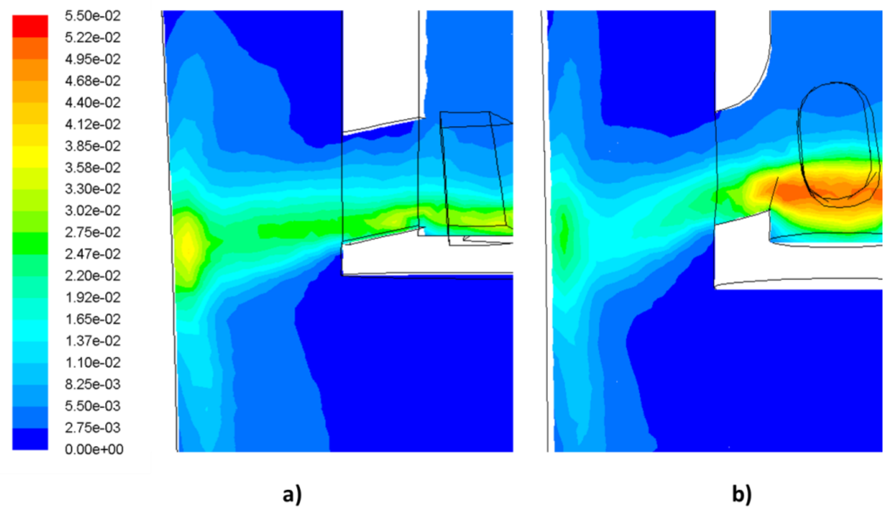

Figure 6.9 a) Contours of TKE (m^2/s^2) on a vertical plane of the mold at the centerline of the port of SEN A. b) Contours of TKE (m^2/s^2) on a vertical plane of the mold at the centerline of the port of SEN B.

A higher magnitude of Turbulent Kinetic Energy (TKE) is observed near the lower part of the port from the discharge, where the jet enters into the volume of the mold, and up to the mold wall, as can be observed in Figure 6.9a. Turbulence is also mainly transported through the lower part of the ports, as shown in Figure 6.9b. However, the upper radius reduces the steep gradients of TKE that were found in the previous case.

Turbulence is also transported through a larger volume of the port, which results in lower magnitudes of TKE. It is expected that the decrease in TKE will result in an overall decrease in turbulence and in the vorticity magnitude, throughout the mold volume.

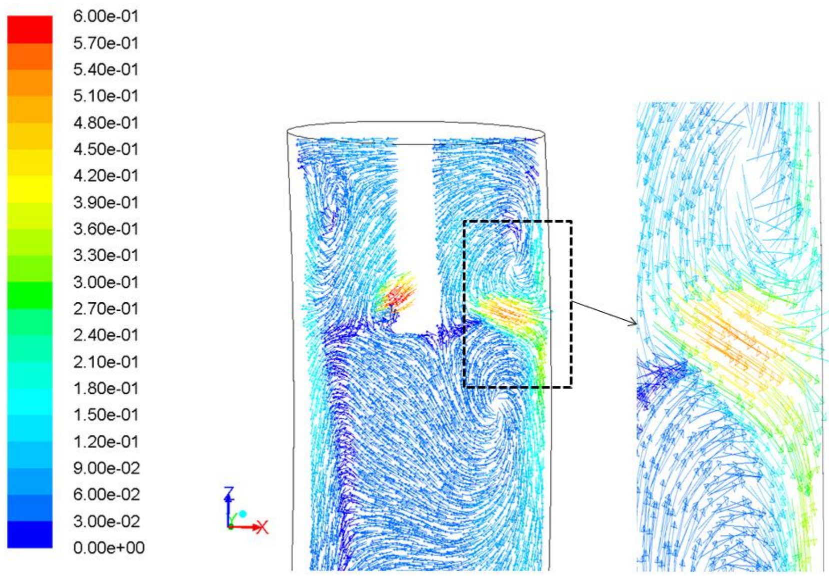

Figure 6.10 Scheme showing a vertical plane located y = -40mm from the centerline of the mold, operating with SEN B.

Similar fluid flow patterns are observed in Figure 6.10 to those obtained for the previous case (Figure 6.3). However, in this case, the magnitudes of velocity are lower throughout the volume of the mold. In the enlarged view of the enclosing box, it is observed that by using SEN B, the magnitudes of the impinging velocity are reduced compared to the previous case. These magnitudes of velocity are in the order of 0.3-0.33 m/s. It is reasonable to mention that this decrease in the magnitude of the impingement velocities would promote a more uniform shell growth. A more detailed view of the velocity field is observed in Figure 6.11. Figure 6.11a shows the recirculation flowing upward after the jet impinges on the mold wall. This recirculation is divided in a stream flowing horizontally in the upper part close to the free surface, and another that flows diagonally in the downward direction. The lower part of the mold is shown in Figure 6.11b. After the impingement on the wall, this recirculation also divides into two main streams that flow horizontally in opposing directions.

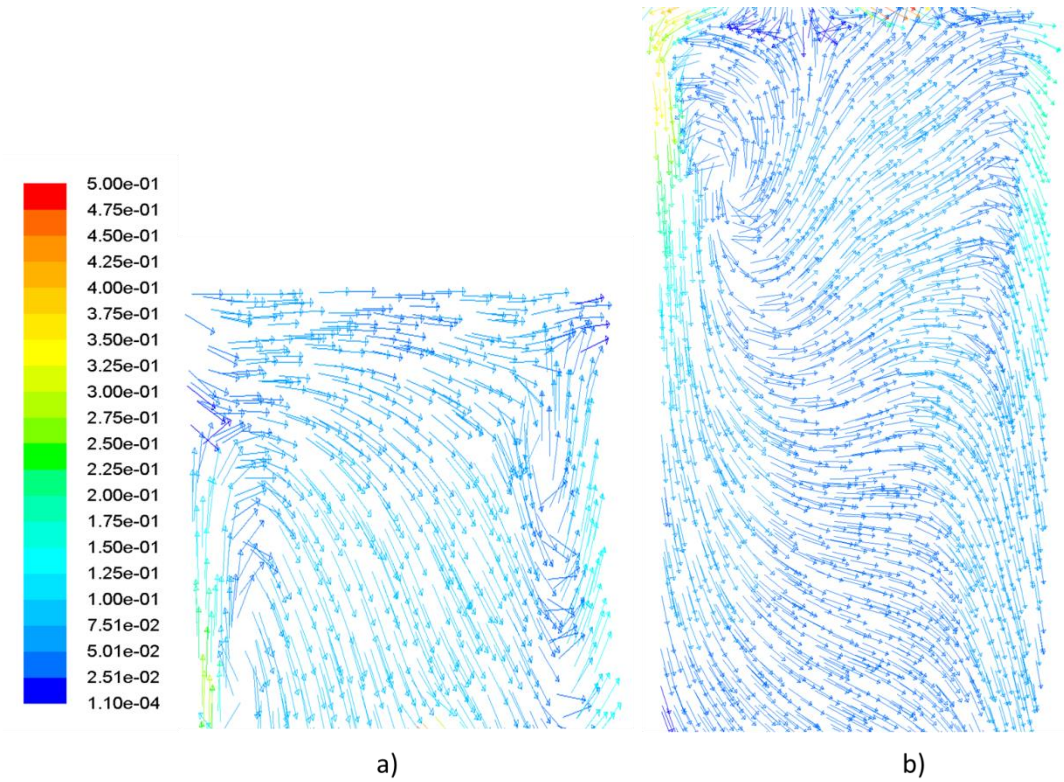

Figure 6.11 Velocity field on a vertical plane of the mold (m/s) located 50 mm from the centerline of the mold operation with SEN B. a) Velocity field in the upper part of the mold. b) Velocity field in the lower part of the mold.

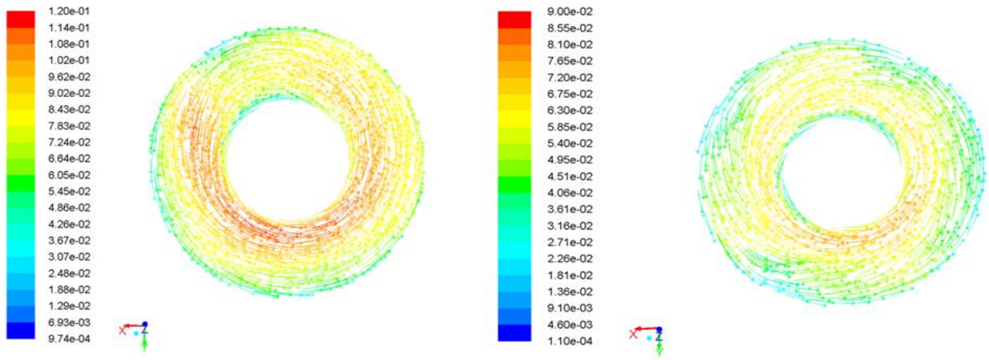

a) b)

Figure 6.12 Velocity field on a transverse plane of the mold (m/s) located 20 mm below the meniscus. a) Velocity field using SEN A. b) Velocity field using SEN B.

In Figure 6.12, the vortexing flows that were observed when operating with the straight nozzle (Chapter 4) were supressed completely and replaced by a rotational flow of liquid that surrounded the body of the nozzle. A higher magnitude of velocity, concentrated around the body of the nozzle is observed for the SEN A case. The momentum from the discharged mainstream is gradually dissipated as the recirculation ascends along the vertical direction, right after impinging on the mold wall. In an upper region, the momentum deficit of the ascending recirculation in the vertical direction is surpassed by horizontal rotational flows. Thereby, the vortex flows observed in Figure 6.2 are gradually suppressed as the ascending recirculation, merges, and no longer opposes the rotational flows. This same explanation applies to the lower regions of the mold. Although very low velocity magnitudes are observed in this region of the mold, the rotational fluid flow patterns extend to 70 mm below the meniscus as observed in Figure 6.13.

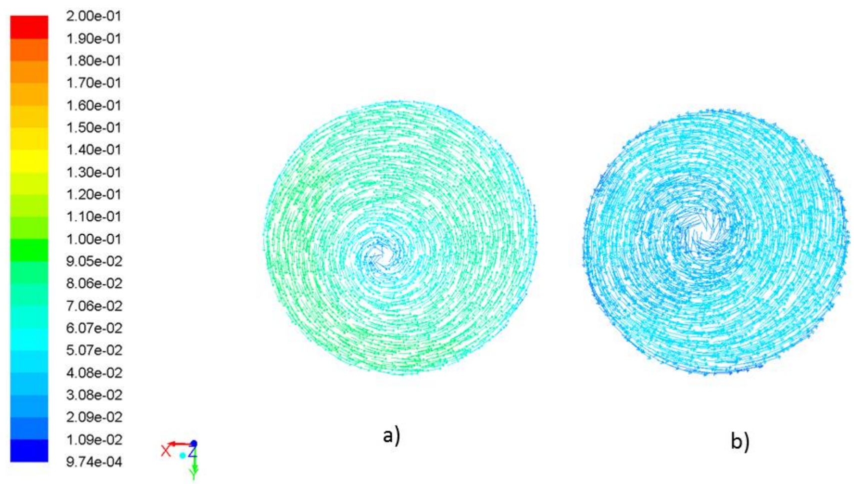

Figure 6.13 Velocity field on a transverse plane of the mold (m/s) located 70 mm below the meniscus. a) Velocity field using SEN A. b) Velocity field using SEN B.

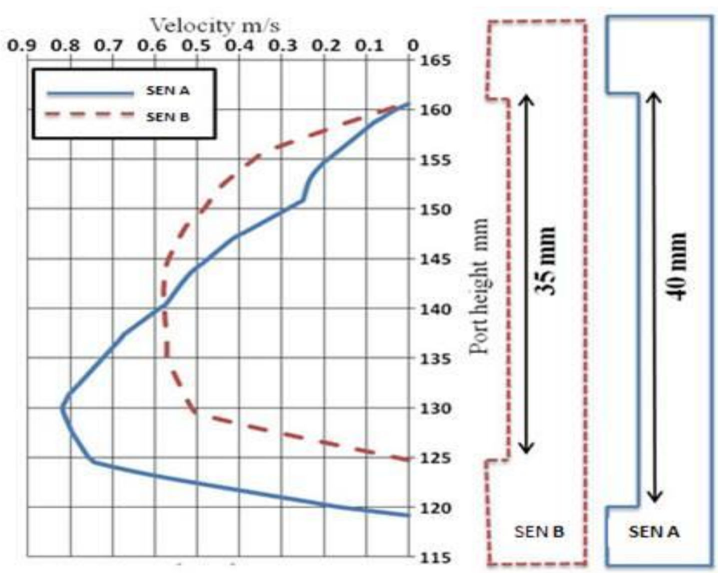

Figure 6.14 Vertical velocity magnitudes derived from the numerical model, down the midpoint of the port of SEN A and B.

The decrease in the velocity magnitudes observed in Figures 6.6, 6.10, 6.12 and 6.13 when operating with SEN B, is also plotted at the midpoint of the port as shown in Figure 6.14. For the same throughputs and bore diameters, SEN A concentrates the main flow in the lower part of the exit port, while SEN B distributes the liquid steel more evenly throughout the exit port. A more even distribution of the liquid metal through the port volume results in a curve with a more flattened nose, and thereby, a substantial decrease in the largest velocities of the discharged jets [120].

6.3.2 Tracer dispersion in the round mold with SEN B

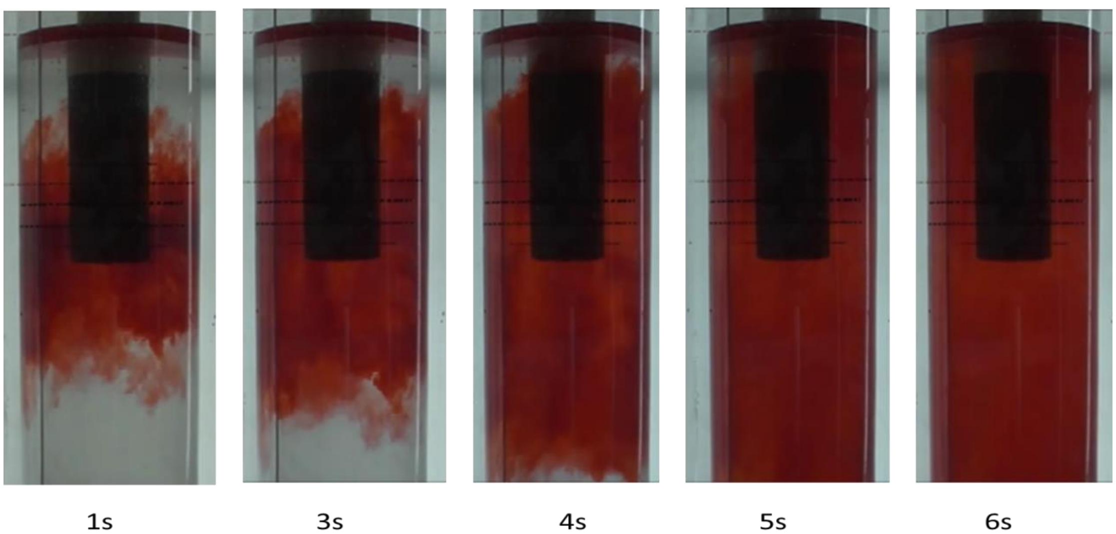

Figure 6.15 Snapshots showing the dye mixing at different times after the dye injection, operating with SEN B, at a casting speed of 1.15 m/min.

The fluid flow patterns revealed by dye injection when operating with SEN B, at a casting speed of 1.15 m/min, are shown in Figure 6.15, at different times after injection. The tracer follows a rotational motion once it enters the mold cavity. The two main recirculations, previously discussed, provide nearly horizontal swirling flows in both directions of the vertical, with similar tracer mixing times. This rotational motion is equally extended toward both directions after impinging on the wall. Therefore, symmetry is observed in the upper and lower part of the mold from the point of the jet's impingement. After 6s, the tracer has reached all zones in the upper region and it is almost completely mixed.

6.3.2 Water-oil experiments in the round mold with SEN B

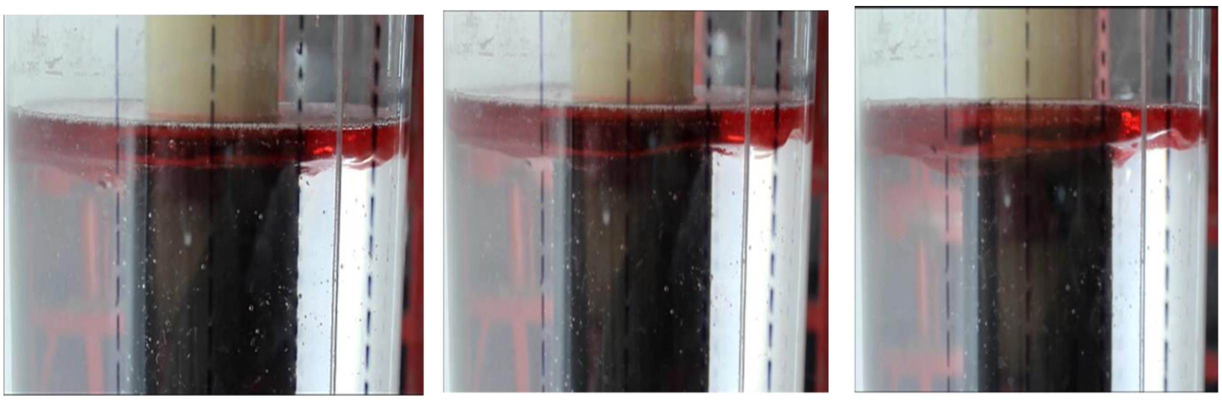

t 1 t 2 t 3

Figure 6.16 Sequence of snapshots showing the interaction between the water and oil in the physical model operating with SEN B at arbitrary times.

Although the horizontal swirling motions cannot be revealed in Figure 6.16, they were apparent during the video recordings that were taken for these experiments. The oil layer was observed to follow a swirling motion, at a constant velocity. The lower phase, in this case the water, transferred its rotational motion to the upper phase. The oil layer was slightly distorted at all times and adopted a curved shape, as observed in the upper right side of the instantaneous snapshots. These distortions are provided by small vortexes that were not predicted by the mathematical models. However, they are not strong enough to form funnels and they vanish rapidly. As the oil layer moves constantly, the oil phase remains very active in such a way that a good lubrication on the strand at all times is expected. The fluid in the upper part of the mold mainly follows the horizontal direction, and thereby, asymmetric flows that cause strong vortexing are decreased. The steep velocity gradients provided by the confluence of flows from different directions are decreased in this case.

6.3.4 Mathematical modeling in square mold with SEN B

After observing the positive impact that the upgraded swirling nozzle (SEN B) can have over the current multiport nozzle in affecting the bulk flow, including a significant reduction in velocities throughout the volume of the round mold, it was decided that further research on this type of nozzle was warranted. Additionally, the fact that the current multiport nozzle used at RTFT for casting square billets had led the operators to conclude that its geometry promoted MPE (as discussed in Chapter 5), made this nozzle a possible alternative. This alternative nozzle, already tested for the round mold, seems to be also a feasible option for the square billet mold operation. This is due to the fact that SEN B can certainly maintain those features sought from the five-ported nozzle, such as a hot meniscus and an even temperature distribution near the slag/steel interface. In addition to that, this nozzle would provide a better control of turbulence throughout the volume of the mold, which could further improve the process. The influence of its design on the fluid flow through the mold cavity is discussed in the following section. The properties of liquid steel and the operating conditions for the square mold are summarized in Table 6.2.

Properties and conditions	Steel (1600°C)
Casting speed (m/min)	1.3, 2.0
Immersion depth (mm)	200
Steel throughput (ton/min)	0.269, 0.413
Steel density (ρ_s), $\mathrm{kg/m^3}$	7050
Slag density (ρ_m), $\mathrm{kg/m^3}$	2600
Air density (ρ_a), $\mathrm{kg/m^3}$	1.7894e-05

Table 6.2. Properties of the mathematical modeling conditions

6.3.4.1 Effective placement of SEN B in the square mold

In the previous section, the swirling flows were obtained throughout the volume of the round mold by using either SEN A or SEN B. The curved nature of the mold adapts for a smooth rotational motion. However, the corners in the square mold could constrain the fluid from developing proper swirling flows. Moreover, if the placement of the nozzle is not done properly, vortex flows will be created. The arrows in Figure 6.17 show the point of impingement of the jets. In Figure 6.17a, it can be observed that the swirling flows were not developed. Rather, many vortexes were created in all sections of the transverse plane. Conversely, the placement observed in Figure 6.17b, successfully induced rotating flows. In this case, the jets flows are directed ahead of the corners. This maintained the circular flow direction along the horizontal without creating vortexes. It is for this reason that the placement of the exit ports of the SEN plays an important role when operating this swirling nozzle for a square mold.

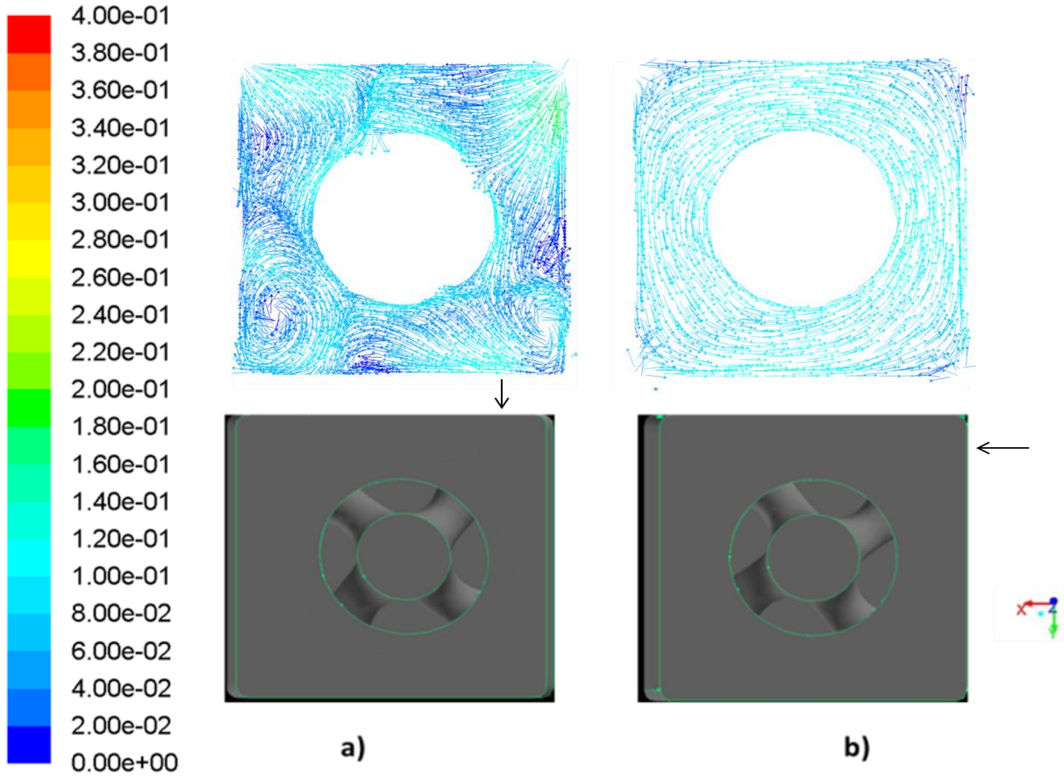

Figure 6.17 Velocity fields on the transverse plane 20 mm below the free surface of the liquid steel a) Predicted velocity field with the first placement b) Velocity field with the second placement.

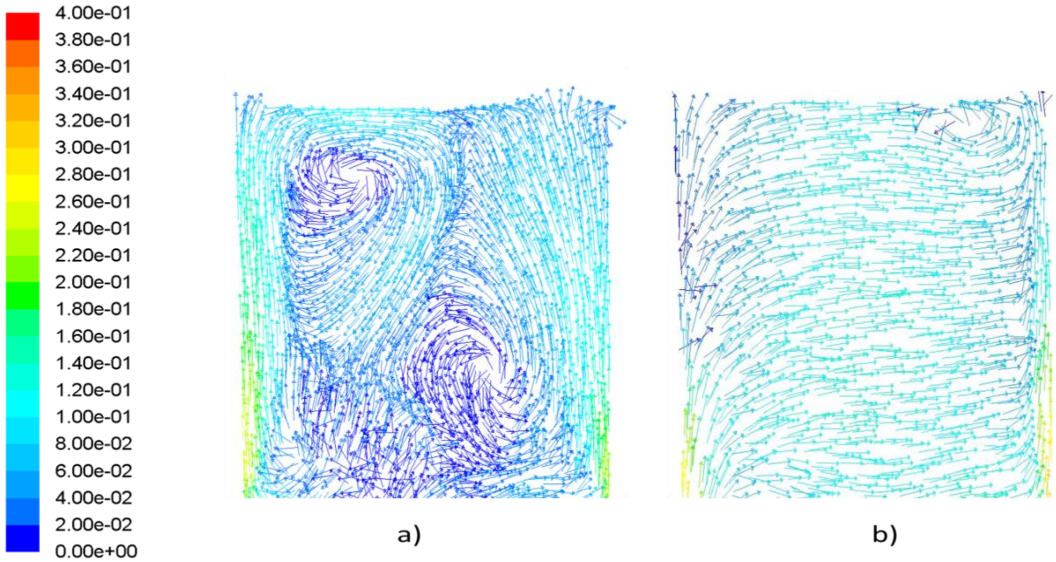

Figure 6.18 Velocity field at the frontal plane of the mold (m/s) operating with SEN B. a) Velocity field in the upper part of the mold with the first placement (see Figure 6.17a). b) Velocity field in the upper part of the mold with the second placement (see Figure 6.17b).

Fluid flow patterns greatly differ from one placement to the other, as observed in Figure 6.18. The issuing jet, streams rise toward the free surface in the vertical direction, creating asymmetric flows. In addition, a strong vortex is observed in the upper left part of the plane on Figure 6.18a. In the second placement of the nozzle, (Figure 6.18b), steel flows perpendicular to the mold length (i.e. radially) and a smaller vortex is observed in the upper right corner of the mold, caused by the geometry of the mold itself.

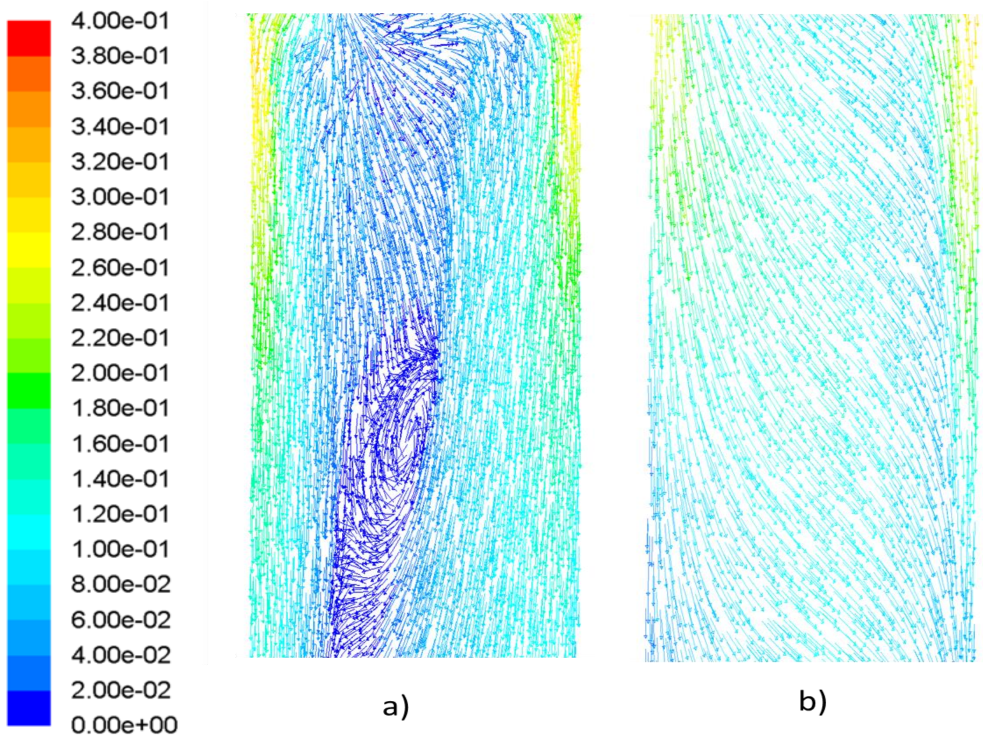

Figure 6.19 Velocity field at the frontal plane of the mold (m/s) operating with SEN B.

a) Velocity field in the lower part of the mold with the first placement. b) Velocity field in the lower part of the mold with the second placement.

The influence that the correct placement of the SEN has on the fluid flow extends to the rest of the mold volume. After colliding near the corners of the mold, the four jets issuing from the SEN mainly flow downwards in the vertical direction. It is clear from Figure 6.19a that the angled ports of SEN B, that induces rotational motions in the round mold, are not effective in this case. The fluid flow patterns in the lower parts of the mold, observed in Figure 6.19b, follow the same direction as in the upper part (Figure 6.18b). Asymmetric flows are not observed in this case. Once the effects of a misplaced SEN B have been discussed, in the next section, a comparative study between SEN B and the five ported nozzle, which was studied on Chapter 5, will be performed.

6.3.5 Comparative study between SEN B and the standard five-ported nozzle

6.3.5.1 Flow patterns and mathematical simulation

The fluid flow patterns revealed through the dye injection method, showed that fluid flows caused by SEN B, when using a casting speed of 1.3 m/min, are given in Figure 6.20a, for different times after injection. It is observed from this Figure that the dye mixes faster along the corners of the mold while the mixing is slower in the horizontal direction where swirling flows are dominant. After the jet impinges near the corner of the mold, it is divided into both vertical and tangential flows. It is noticed that the vertical flows are stronger than the rotational motion, given that the four corners of the mold restrain the flows in the horizontal direction. However, the mixing times are lower, while the distribution of the tracer is more even, than those observed with the five-ported nozzle (Figure 6.20b). Similar dye mixing patterns are observed at a high casting speed, as can observed in Figure 6.21. In this case the dye mixes faster as compared to the precedent case.

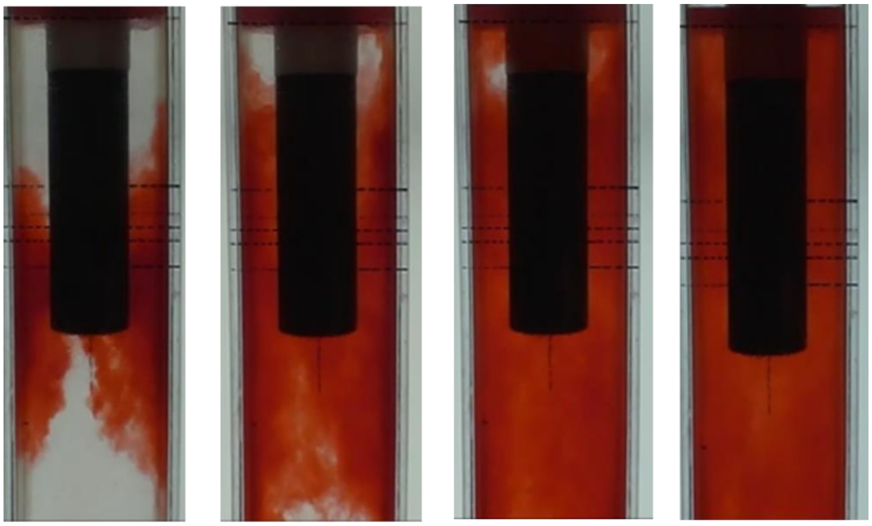

1s 2s 3s 4s

Figure 6.20 a) Snapshots showing the dye intermixing with water at different times after the dye injection; operating with SEN B at a casting speed of 1.3 m/min.

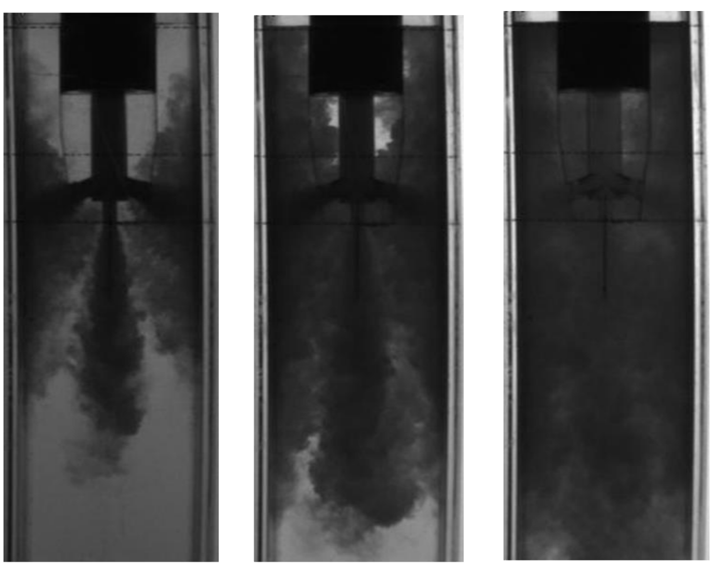

1s 2s 3s

b) Snapshots showing the dye intermixing with water at different times after the dye injection; operating with the five ported SEN at a casting speed of 1.3 m/min.

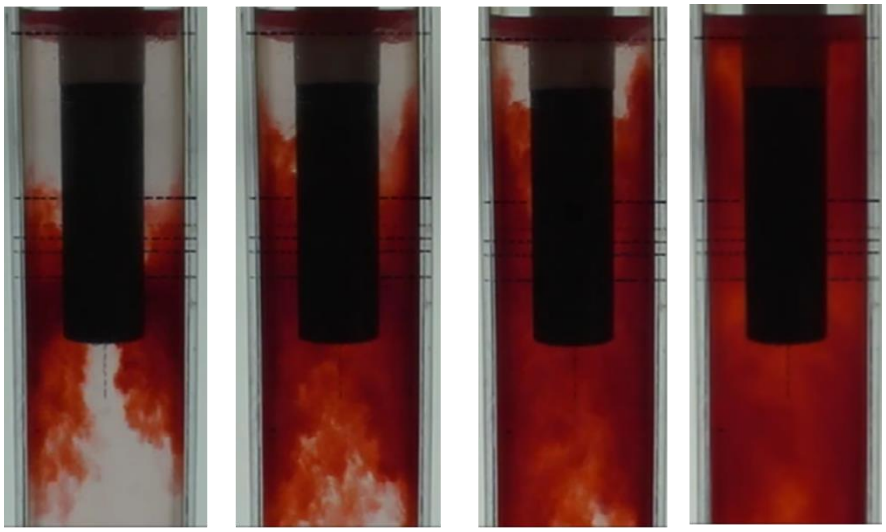

Figure 6.21 Snapshots showing the dye intermixing with water at different times after the dye injection; operating with SEN B at a casting speed of 2.0 m/min.

The computed velocity fields for the frontal plane when operating with SEN B under transient conditions are shown in Figure 6.22a. Strikingly, it is observed that once the jets impinge on the mold wall, the upper and lower streams, observed in Figure 6.22b, now follow a rotational horizontal motion from left to right. The rotating upper stream still provides some instability to the meniscus. However, the vortexes near the meniscus region are smaller as compared with those observed when operating with the five ported nozzle. On the other hand, the transverse areas of each of the ports of SEN B are larger than the corresponding areas of the currently used nozzle. In addition to an increase in the transverse area, the effect of the radiuses on the edges of the ports promotes a more efficient usage of the internal volume, which further enhances the decrease in the velocity of the bulk flow, and the level of vorticity transferred into the bulk liquid within the square billet mold. Accordingly, the strong impingements on the walls are largely damped. A more uniform growth of the shell can be expected given the magnitude of decrease of the discharge velocities from the SEN.

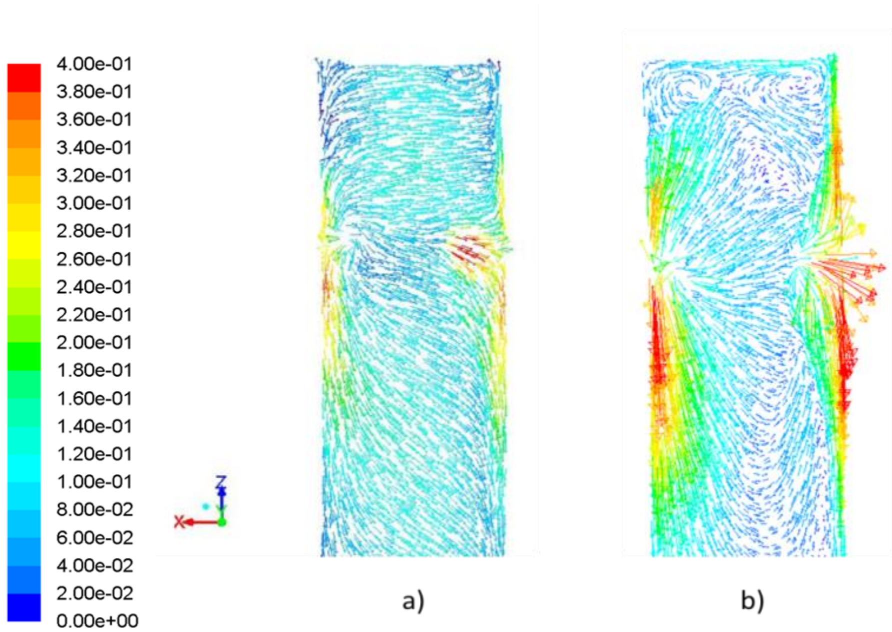

Figure 6.22 Velocity fields on the frontal plane of the mold (m/s) at an immersion depth of 200 mm, and a casting speed of 2.0 m/min. a) Velocity field with the alternative nozzle design. b) Velocity field with the five ported nozzle.

6.3.5.2 Water-Oil Experiments

With respect to the modeling of slag-steel interactions in the square billet mold, Figures 6.23a to 6.23c reveal a very unstable interface at all times. At some time steps, it is observed that the upper liquid stream flowing up toward the meniscus, is strong enough to remove the oil phase near the mold corner on the outer radius side. This allows the liquid to be in contact with air. This trend, found in the water model, can be qualitatively transferred to the actual process. There, liquid steel flows, which can remove the immediate layer of liquid slag and would then interact with the layer of sintered slag, would lead to mold powder entrainment. This region is marked by the arrow in Figure 6.23a. A more stable interface is observed; from Figures 6.23d to 6.23f, where the lumps of oil that fluctuate near the mold walls are not present in this set of Figures. In addition, the upper stream that completely removes the oil in Figure 6.23a is not observed on this set of snapshots. A less distorted interface is maintained in the second set of snapshots.

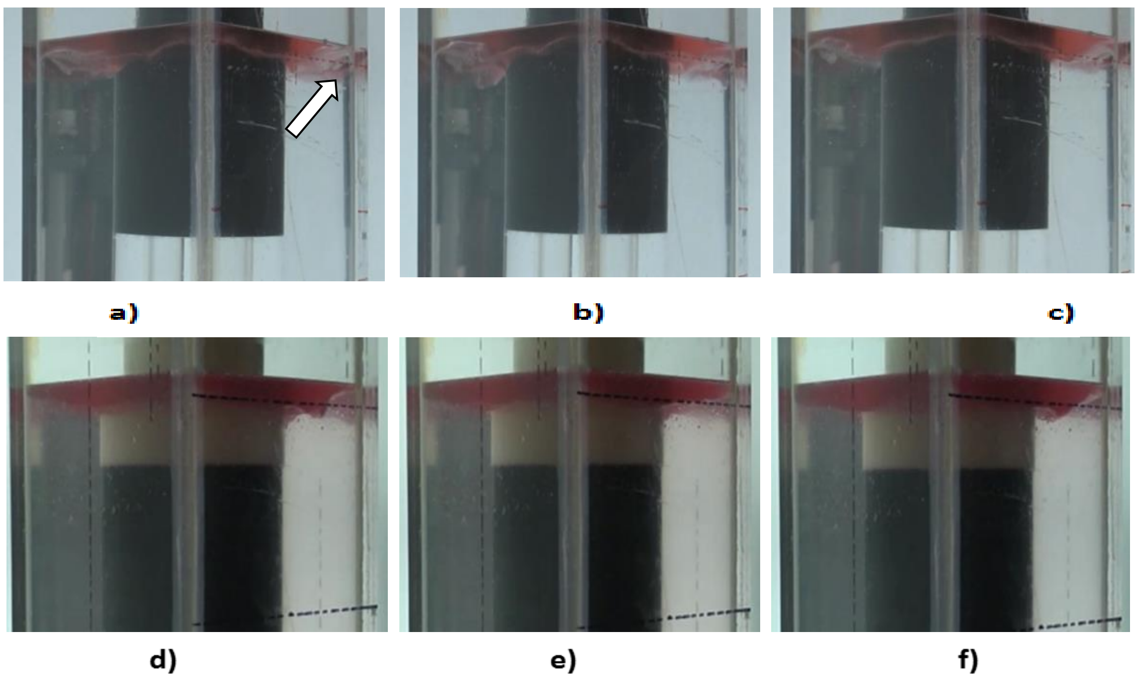

Figure 6.23. Snapshots, showing the interactions between water and oil in the physical model, at a casting speed of 2.0 m/min for an SEN depth of 200 mm. a-c) the five ports nozzle. d-f) The four ports nozzle (SEN B).

In both Figures 6.24a and 6.24b, a single vortex can be observed near the free surface. However, the size and strength of the vortex is not as strong as those discussed in

Chapter 5. The averaged velocity field obtained from the instantaneous PIV measurements shown in Figure 6.24a is in good agreement with the velocity field predicted by the mathematical model in Figure 6.24b. Figure 6.24b also corresponds to a zoomed view of Figure 6.22a. The impingement velocity is around 0.25 to 0.28 m/s.

6.3.5.3 PIV measurements

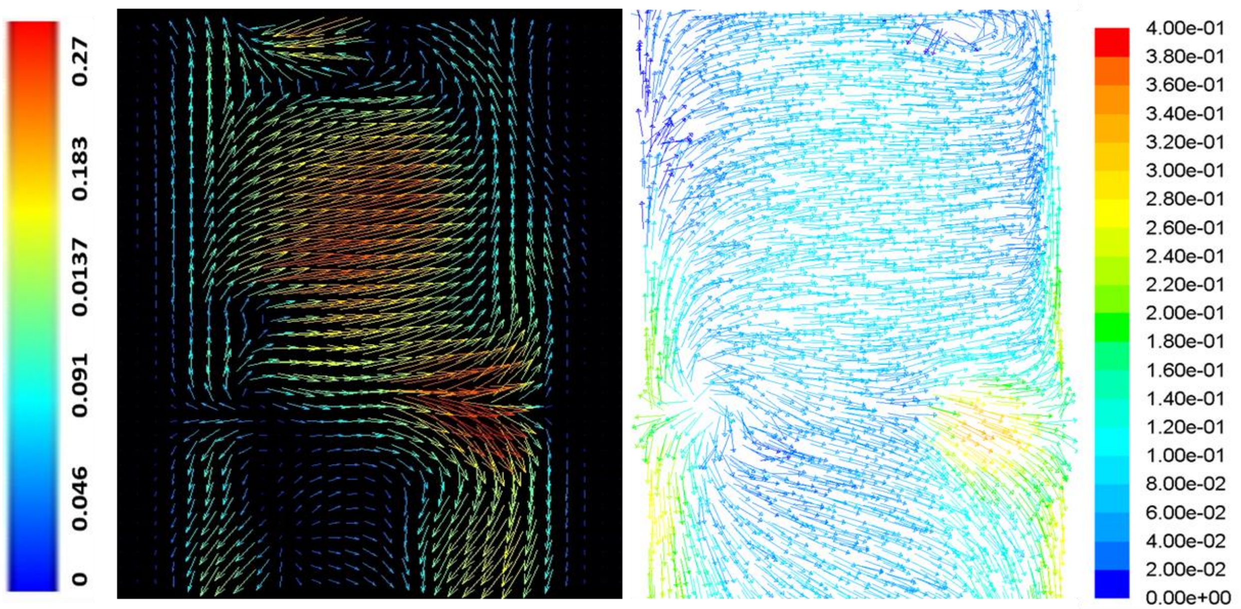

a) b)

Figure 6.24 Velocity fields on the frontal plane of the mold (m/s) at an immersion depth of 200 mm, and a casting speed of 2.0 m/min. a) Velocity field obtained from the PIV measurements. b) Velocity field obtained from the mathematical model.

Many vorticity islands can be observed on the frontal plane in Figure 6.25b. As the fluid is transported horizontally or radially, it is noticeable that the islands extend along the frontal plane from left to right. These fluid flow patterns differ from those observed in Figure 6.25a, in which islands extend vertically. In this case, turbulence is mainly transported along the corners of the mold in the vertical direction, while in the previous case, is distributed more evenly in the horizontal direction with less steeper gradients of vorticity along the frontal plane. It is also important to emphasize that the vorticity islands close to the surface are much lower in magnitude when operating with SEN B (i.e. up to 6.7 s^{-1} versus 25.85 s^{-1}). This would certainly help in reducing the incidence of mold powder entrainment.

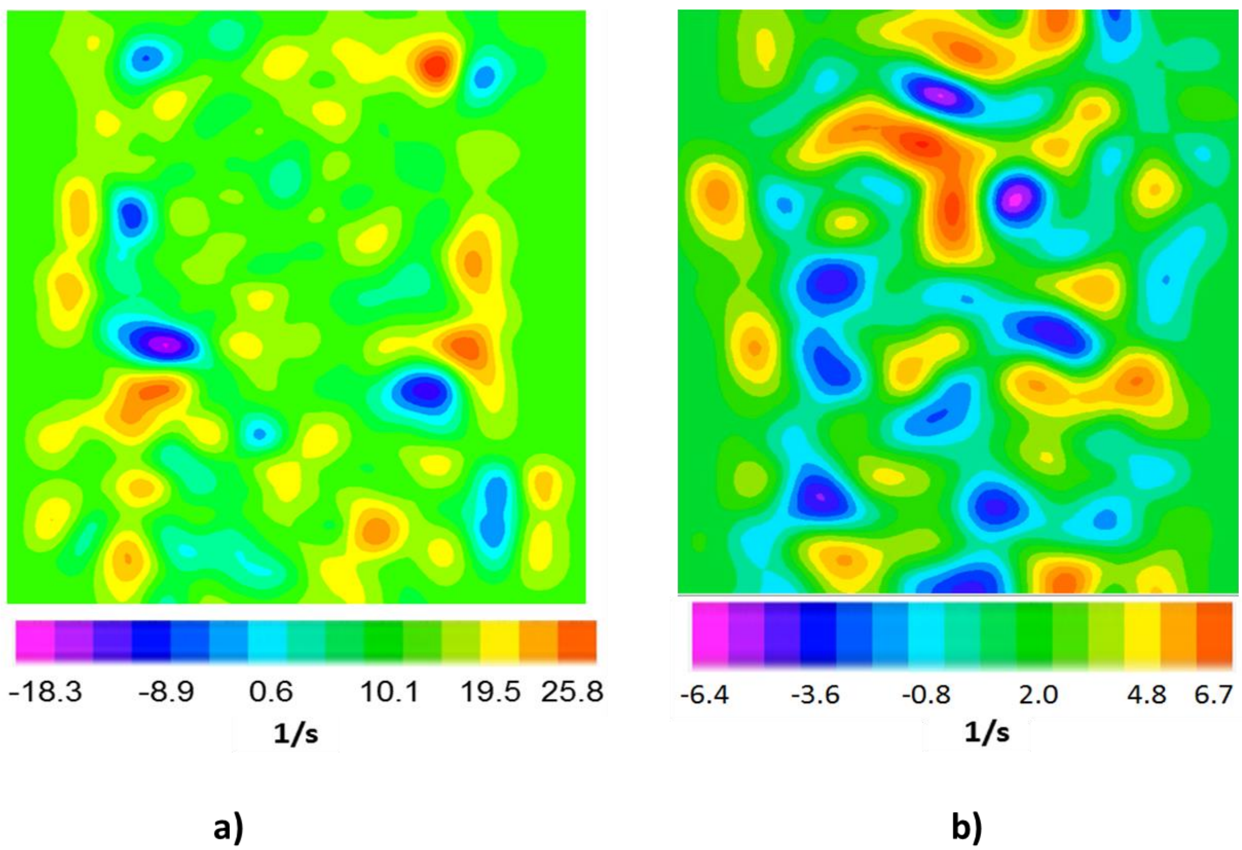

Figure 6.25. Vorticity contours obtained in the frontal plane at a casting speed of 2.0 m/min and SEN depth of 200 mm. a) five ports nozzle. b) alternative nozzle (SEN B).

6.3.5.4 Mutiphase modeling

The VOF method was used in this section to consider the actual multiphase system consisting of steel, slag and air. The properties of liquid steel and the operating conditions for the square mold are summarized in Table 6.3. The details of the VOF modeling procedures were previously discussed in section 3.2.1. The schematic of the mold and planes used to compute the results are found in section 5.3.4.

Properties and conditions	Steel (1600°C)
Casting speed (m/min)	2.0
Immersion depth (mm)	200
Steel throughput (ton/min)	0.413
Steel density (ρ_s), $\mathrm{kg/m^3}$	7050
Slag density (ρ_m), $\mathrm{kg/m^3}$	2600
Air density (ρ_a), $\mathrm{kg/m^3}$	1.7894e-05
Interfacial tension, (N/m), steel / slag	1.3
Interfacial tension, (N/m), air / slag	0.075
Interfacial tension, (N/m), air / steel	1.6

Table 6.3 Properties of the mathematical modeling conditions

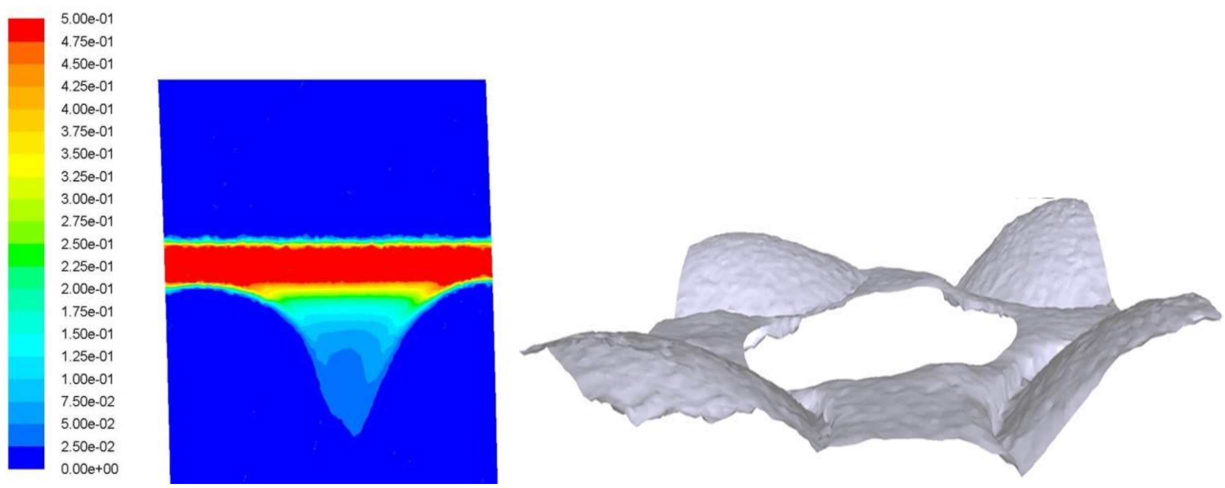

a) b)

Figure 6.26 Contours of volume fraction of “slag” computed at the frontal plane operating with the five-ported nozzle. a) Volume fractions from 0 to 0.5. b) Meniscus topography in 3D.

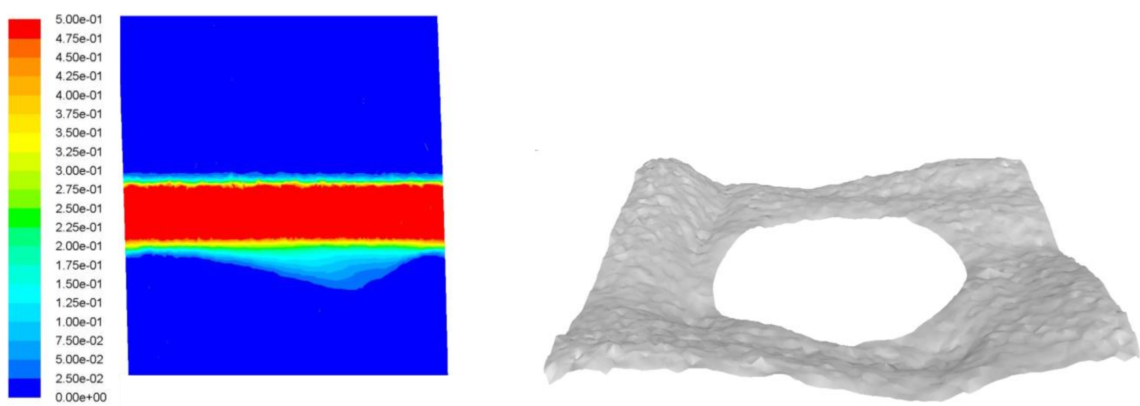

a) b)

Figure 6.27 Contours of volume fraction of “slag” computed at the frontal plane operating with SEN B. a) Volume fractions from 0 to 0.5. b) Meniscus topography in 3D.

The VOF method was used in this section to consider the actual multiphase system consisting of steel, slag and air. Figures 6.26 and 6.27 shows the volume fraction of slag computed for a plane where the darker areas correspond to a mass fraction of 0.5 or higher. It is clear in these figures that the meniscus is distorted in both cases. The interface is highly altered when operating with the five-ported nozzle, as observed in Figure 6.26a. The jets of liquid steel that rise upward along the corners from both sides of the mold, push slag toward the central region between the inner and outer radius. The accumulated slag at this point is entrained into the liquid steel and flows near the mold wall. The interaction between the slag phase and the solidifying shell could cause MPE. Although the interface is highly altered, detachment of slag was not observed. This interface behavior qualitatively matches the results observed in the water-oil experiments. Slag entrainment into the liquid pool is also observed when operating with SEN B as shown in Figure 6.27a. However, the meniscus preserves a less distorted shape than in the previous case. In addition, less amount of slag is entrained into the steel pool near the regions where slag tends to accumulate when operating with the five-ported nozzle [120]. The rotational motion combined with transient flows near the meniscus region; still produce some instability on the slag-metal region.

6.4 Summary of Results

1. The chamfering or smoothing of the upper and vertical edges of the nozzle fitted with angled ports successfully increased the effective transverse area of the port through which the liquid steel flows. The novel features on the ports geometry reduced the maximum discharge velocity of the incoming steel (water), while the low pressure regions and associated backflows within the four ports were suppressed. These improvements in the geometry of the four exit ports of the swirling SEN may allow for further refinements in the design of ports, such that further increases in the transverse area could result in even lower fluid flow velocities throughout the volume of the mold. To attempt increasing the area of the ports when operating with regular nozzle types, such as SEN A, results ineffective. This is because sharp edges of the ports reduce the effective volume through which the molten metal flows.

2. Lower magnitudes of impingement velocity were observed in the round mold operation using SEN B as compared to those delivered by SEN A. However, as the impinging velocities contribute to the rotation of the liquid metal, a stronger rotational motion is observed when operating with SEN A.

3. The rotational motions are more difficult to attain for the square mold operation. A misplacement of the nozzle will affect the fluid flow severely. Asymmetric flows and vortexes were observed when operating with a misplaced nozzle. However, swirling motions can be successfully attained, if SEN B is placed properly. The

split of the jet into vertical and rotational flows, together with the decrease in the magnitudes of the discharging velocity, provides more stability at the meniscus as compared to the flows encountered when the square mold is equipped with a five ported nozzle.

4. SEN B preserves the advantages of the five ported nozzle, such as fast mixing times near the meniscus region, while at the same time reduces fluctuations at the meniscus. This could result in lower incidence of MPE defects and needs to be tested in practice.

5. The largest velocities of impingement on the square and round mold walls when operating with SEN B are insufficient to endanger the uniform growth of the shell or to cause a strand breakout.

7.0 Conclusions

In the present doctoral thesis, fluid flow characterization was performed in round and square billet molds in order to understand the causes for MPE and related subsurface defects in billet casting operations. For that purpose, physical and mathematical modeling tools have been applied under different casting conditions. The details of the findings on fluid flow were summarized at the end of each chapter. Therefore, in this section, the aftermath of those findings are discussed to provide a more general overview. Thus, it was observed throughout this research, that although mathematical models did not perfectly match with the experiments, given that fluid flow in the actual molds is very transient in nature; they do provide good insights into the process. They work as a useful tool to complement the results delivered by the different sets of experiments. The combined use of both tools helped in understanding the current process and in providing subsequent recommendations for steel quality improvements. The mathematical models developed to analyze different mold conditions proved to be in reasonable agreement with experimental measurements.

MPE entrainment mechanisms relevant to slab casting operations were not detected for the billet casting processes currently studied for square and round molds. From the MPE mechanisms mentioned in Chapter 2, entrainment by mold level fluctuations is the only predominant mechanism. Other MPE mechanisms, such as upward flow impinging upon the top surface and top surface balding, only occurred when a very shallow position of the nozzle, combined with a high casting speed, were considered. In any case, these conditions are not executed during current casting conditions at the plant and were only examined to explore the effect of an unusually shallow position. In fact, a strong shearing force, dragging down or complete detachment of a section of slag into the underlying liquid steel is not always necessary for mold powder entrainment to occur. Therefore, even if a strict control of the operation is performed, MPE entrainment may take place if meniscus level stability is not maintained properly. Transient fluid flows combined with slag rim formation, sudden level fluctuations and mold oscillation may result in MPE. Under the current operation, it was observed that both nozzles promote asymmetric, vortexing flows, inside the volume of the corresponding mold, without strongly dragging or shearing slag droplets, but providing meniscus level instability. Other transients added to the process, such as misalignment of the nozzle, would further reinforce asymmetric flows and a decrease in steel quality. Therefore, a strict control on operating conditions and a proper SEN design that supports the meniscus stability are fundamental for obtaining better steel qualities.

After a careful analysis of the results obtained, it was found that the SEN plays a very important role in controlling fluid flow, and that many of the previously mentioned defects, are related to the design of a SEN. Hence, in this research, attention was focused on the proper SEN design for the billet casting process. The proposed SEN design is capable of developing swirling flows in square and round billet molds, while an appropriate control of fluid flow is attained. It is also expected that with the proposed design, a more symmetric fluid flow pattern and uniform heat transfer will be attained near the meniscus region. MPE and related subsurface defects would also be reduced, since vortexes and asymmetric flows are supressed near the meniscus region with SEN B. This design can be also suitable for the bloom casting process, where similar types of nozzles are established faster as compared with those nozzles proposed for the billet casting process. This is because the volume of the bloom is larger, and therefore, allows for a less stringent control of fluid flow. A very detailed SEN design is not always necessary in bloom casting operations. This creates an opportunity for the current plant and other steel plants to properly control fluid flow in all their long products with a single SEN design. If the proposed nozzle is placed correctly in a square mold, the rotational motion is attained successfully. This rotational motion provided by the nozzle, would contribute when combined with Electromagnetic Stirring (EMS) devices. In this case, less energy consumption would be required to trigger the rotational motion, given that the incoming fluid discharged by the nozzle is already coupled with the stirrer motion.

Contribution to Original Knowledge

This work is intended as a contribution in extending our knowledge in the area of SEN design for billet casting. The aim of this research is for steel quality improvement. Furthermore, a description of the mechanisms found for slag entrapment in billets molds which, given the very narrow spaces, should differ from those reported in slab molds, is not available on the literature. A contribution on the understanding of fluid flows and related MPE mechanisms acting in the operation of billet molds was also sought.

The following parts of this thesis are claimed to be original and have been performed for the first time:

1. Detailed analysis of fluid flow in terms of instantaneous velocity and vorticity fields in a full scale water model for square and round mold billets was conducted. Important details, such as mold curvature, usually neglected in

previous research were considered for the current experiments and shown to be very important.

2. A detailed MPE mechanism related to mold level fluctuations and based on fluid flow analysis has been proposed for the continuous casting of round billet molds operating with a straight nozzle in Chapter 4.

3. It was shown that under normal operating circumstances, the sole MPE mechanism acting on billet molds is the entrainment by mold level fluctuations. Only at very high levels of turbulence, other MPE mechanisms reported for slab casting may be present as discussed in Chapter 5.

4. Physical modeling, using PIV measurements and water-oil experiments, showing swirling motions delivered to the mold cavity through the ports of a SEN, was conducted. The previously reported research found in the literature is mainly focused on mathematical modeling.

5. An alternative nozzle for billet casting has been proposed. The design is supported by physical and mathematical modeling. The features and characteristics of this new nozzle differ from those previously reported in the literature. The feasibility of using a single nozzle for casting round and square billets, while having positive results in fluid flow control, has also been studied. We now need to conduct plant tests/trials.

Future Work

1. The water model considered the billet casting operation, without taking into account the possible influence that the sliding gate has on the fluid flow. A study of the fluid flow by considering the sliding gate geometry could provide more insights on the process.

2. The current research was based on isothermal conditions. However, an investigation of the temperature distribution, inside the round and square molds, and shell growth in both molds is needed. A more detailed picture of the actual process will be obtained by considering these variables.

3. To study the effect of the fluid flow together with Electromagnetic Stirring (EMS) practices. The influence of EMS on fluid flow remains an area that needs further research. This will allow for further improvements in the operation.

4. Further efforts to study possible improvements on the proposed SEN design are to be conducted. Plant trials with the proposed nozzle design would provide further insight on the process.

5. An issue that remains unsolved in the operation of RTFT is the proper alignment of the SEN. A study of a misaligned nozzle by considering the proposed nozzle could solve this problem.

REFERENCES

1. B.G. Thomas, "*Continuous Casting: Modeling*," *The Encyclopedia of Advanced Materials*, (J. Dantzig, A. Greenwell, J. Michalczyk, eds.) Pergamon Elsevier Science Ltd., Oxford, UK, Vol. 2, 2001, 8p., (Revision 3, Oct. 12, 1999).

2. Guthrie, R.I.L., *Engineering in Process Metallurgy.* Oxford University Press, 1992.

3. D. Mazumdar, J.W. Evans, *Modeling of Steelmaking Processes.* CRC Press, 2011.

4. Zhang, L., S. Yang, X. Wang, K. Cai, J. Li, X. Wan, and B.G. Thomas, "*Investigation of Fluid Flow and Steel Cleanliness in the Continuous Casting Strand"*, Metallurgical and Materials Transactions B, 38B:1, Feb., 2007, pp. 63-83

5. L.J. Heaslip, J.S., *Physical Modeling and Visualization of Liquid Steel Flow Behavior During Continuous Casting.* Iron & Steelmaker, 1999. 26(1): p. 33-41.

6. R. Chaudhary, B.T.R., B.G. Thomas, *Differences between Physical Water Models and Steel Continuous Casters: A Theoretical Evaluation.* Materials Science and Technology, 2009: p. 1091-1001.

7. D. Gupta and A.K. Lahiri, *Cold model study of the surface profile in a continous slab casting Mold:Effect of second phase*, Met. & Mats Trans. B, Vol. 27B, Aug 1996, pp. 695-697.

8. X.K. Lan, J.M. Khodadadi, F. Shen, *Evaluation of Six k-e Turbulence Model Predictions of Flow in a Continuous Casting Billet-Mold Water model Using Laser Doppler Velocimetry Measurements.* Metallurgical and Materials Transactions B, 1997. 28B: p. 321-332.

9. B. Thomas, Q.Y., S. Sivaramakrishnan, T. Shi, S.P. Vanka, M. Assar, *Comparison of Four Methods to Evaluate Fluid Velocities in a Continuous Slab Casting Mold.* ISIJ, 2001. 41(10): p. 1262-1271.

10. S. Sivaramakrishnan, H.B., B. Thomas, S. Pratap, P. Dauby, M. Assar, *Transient Flow Structures in Continuous Casting of Steel.* Steelmaking Conference Proceedings, 2000. 83: p. 541-557.

11. Versteeg, H. K and Malalasekera, W., *An Introduction to Computational Fluid Dynamics: The Finite Volume Method*, McGraw-Hill, Loughborough University, (1995).

12. B. Launder, D.S., *Mathematical Models of Turbulence.* Academic Press, 1972.

13. Qinfu, H., Zongshu, Z., *Comparison Between Standard and Renormalization Group k-ε models in numerical simulation of Swirling Flow Tundish*, ISIJ International, (2005) 45(3), pp 325-330.

14. Patankar, S. V., and Spalding, D. B., *A Calculation Procedure for Heat, mass and Momentum Transfer in Three Dimensional Flows,* International Journal of Heat and Mass Transfer, (1972) 15, 1787-1806.

15. Donald E. Hershey, Brian G. Thomas and Fady M. Najaar, *Turbulent Flow Through Bifurcated Nozzles*, International Journal for Numerical Methods in Fluids, Vol. 17, 23-47 (1993).

16. S. Sivaramakrishnan, B.G.Thomas and S.P.Vanka, *Large Eddy Simulation of Turbulent Flow in Continuous Casting of Steel,* Materials Processing in the Computer Age III, V. Voller and H. Henein, eds.,TMS Annual Meeting, Nashville, TN, March 12-16, 2000, pp. 189-198.

17. Quan Yuan, Bin Zhao, Pratap Vanka, Brian G. Thomas, *Study of Computational Issues in Simulation of Transient Flow in Continuous Casting*, steel research int. 76 (2005) No. 1, pp.33-43

18. Brimacombe, J. and K. Sorimachi, *Crack formation in the continuous casting of steel.* Metallurgical and Materials Transactions B, 1977. 8(2): p. 489-505.

19. Lankford, W., *Some considerations of strength and ductility in the continuous-casting process.* Metallurgical and Materials Transactions B, 1972. 3(6): p. 1331-1357.

20. Brian G. Thomas and Claudio Ojeda, *Ideal Taper Prediction for Slab Casting*, 2003 ISSTech Steelmaking Conference, Indianapolis, IN, USA, April 27-30, 2003, ISS-AIME, Warrendale, PA, 2003, pp. 295-308.

21. Ya Meng and Brian G. Thomas, *Heat-Transfer and Solidification Model of Continuous Slab Casting: CON1D*, METALLURGICAL AND MATERIALS TRANSACTIONS B, VOLUME 34B, OCTOBER 2003, 686-705.

22. C. Li & B.G. Thomas, *Maximum Casting Speed For Continuous Cast Steel Billets, Based on Sub-mold Bulging Computation*, 85th Steelmaking Conf. Proc., ISS, Warrendale, PA, (held in Nashville, TN, March 10-13, 2002), pp. 109-130.

23. Dukman Lee, C.H. Moona, S.C. Moonb,1, H.D. Park, *Development of healing control technology for reducing breakout in thin slab casters*, Control Engineering Practice, Volume 17, Issue 1, January 2009, Pages 3–13.

24. Hoseok NAM, Hwa-Soo PARK and J.K. YOON, *Numerical Analysis of Fluid Flow and Heat Transfer in the Funnel Type Mold of a Thin Slab Caster*, ISIJ International, Vol. 40 (2000), No. 9, pp. 886–892.

25. Roland Kempf, Jurgen Adamy, *Sequential pattern recognition employing recurrent fuzzy systems, Fuzzy sets and systems*,Volume 146, Issue 3, 16 September 2004, Pages 451–472.

26. Yale Zhang, Michael S. Dudzic, *Online monitoring of steel casting processes using multivariate statistical technologies: From continuous to transitional operations,* Journal of Process Control Volume 16, Issue 8, September 2006, Pages 819–829.

27. Jansto, S., *Effect of melting and casting parameters on the hot ductility behavior of Nb-bearing beams, billets and slabs.* Steel in Translation, 2011. 41(9): p. 711-718.

28. Yasumoto K., Maehara Y., Ura S. and Ohmori Y., *Effects of sulphur on hot ductility of low-carbon steel austenite.* Materials Science and Technology, 1985. 1(2): p. 111-116.

29. Shankar, V., Gill T.P.S., Mannan S.L. and Sundaresan S., *Solidification cracking in austenitic stainless steel welds.* Sadhana, 2003. 28(3): p. 359-382.

30. Brimacombe, J., *The challenge of quality in continuous casting processes.* Metallurgical and Materials Transactions B, 1999. 30(4): p. 553-566.

31. Wolf, M. and W. Kurz, *The effect of carbon content on solidification of steel in the continuous casting mold.* Metallurgical and Materials Transactions B, 1981. 12(1): p. 85-93.

32. Brimacombe, J., F. Weinberg, and E. Hawbolt, *Formation of longitudinal, midface cracks in continuously-cast slabs.* Metallurgical and Materials Transactions B, 1979. 10(2): p. 279-292.

33. Sorimachi, K., *Improvements in mathematical modelling of stresses in continuous casting of steel.* Ironmaking & steelmaking, 1977. 4(4): p. 240.

34. Chunsheng Li and Brian G. Thomas, *Maximum casting speed for continuous cast steel billets based on sub-mold bulging computation* 85th Steelmaking Conf. Proc., ISS, March 10-13, 2002: p. 109-130.

35. Li, C. and B. G. Thomas, *Thermomechanical finite-element model of shell behavior in continuous casting of steel.* Metallurgical and Materials Transactions B, 2004. 35(6): p. 1151-1172.

36. K. R. Michalek, T.G. O'Connor, B. G. Thomas, and J. A. Dantzig, *Initial development of thermal and stress fields in continuously cast steel billets.* Metallurgical and Materials Transactions A, 1988. 19(10): p. 2589-2602.

37. X. Li, H. Ding, Z. Tang, and J. He, *Formation of internal cracks during soft reduction in rectangular bloom continuous casting.* International Journal of Minerals, Metallurgy, and Materials, 2012. 19(1): p. 21-29.

38. Thomas, B., *Modeling of continuous casting defects related to mold fluid flow.* Iron and Steel Technology, 2005. 3(5): p. 128-143.

39. Lifeng Zhang and Brian G. Thomas, *Evaluation and control of steel cleanliness review.* 85th Steelmaking conference proceedings 2002: p. 431-452.

40. L. Zhang, Y. Wang, and X. Zuo, *Flow Transport and Inclusion Motion in Steel Continuous-Casting Mold under Submerged Entry Nozzle Clogging Condition,* Metallurgical and Materials Transactions B, Vol. 39B, August 2008, pp. 534-550.

41. Brian G. Thomas, Alex Dennisov, and Hua Bai, *Behavior of Argon Bubbles during Continuous Casting of Steel, SS 80th Steelmaking Conference*, Chicago, IL, ISS, April 13-16, 1997, Proceedings pp. 375-384. B.

42. L. Zhang, J. Aoki, and Brian G. Thomas, *Inclusion Removal by Bubble Flotation in a Continuous Casting Mold*, Metallurgical and Materials Transactions B, Vol. 37B, JUNE 2006, 361-379.

43. C. Pfeiler, M. Wu, A. Ludwig, *Influence of argon gas bubbles and non-metallic inclusions on the flow behavior in steel continuous casting*, Materials Science and Engineering A 413–414 (2005) 115–120.

44. Zhang, L., S. Yang, X. Wang, K. Cai, J. Li, X. Wan and B.G. Thomas. *Physical, Numerical and Industrial Investigation of Fluid Flow and Steel Cleanliness in the Continuous Casting Mold at Panzhihua Steel,* AISTech 2004, Nashville, TN, Sep.15-17, 2004. Assoc. Iron Steel Technology, Warrendale, PA.

45. Thomas, B.G., *Mathematical modeling of fluid flow in continuous casting.* ISIJ international, 2001. 41(10): p. 1181.

46. Gert Abbel, W.Damen, G. Gendt and W. Tiekink, *Argon Bubbles in Slabs.* ISIJ international, 1996. 36(Supplement): p. S219-S222.

47. B. Santillana, Brian G. Thomas, G. Botman and E. Dekker, 3D *Thickness Measurement Technique for continuous Casting Breakout Shells*, Proc. 7th ECCC, METEC, Düsseldorf, Germany, (2011), Session 3, 1.

48. S. Garcia-Hernandez, J.J. Barreto, R.D. Morales and H. Arcos-Gutierrez, *Numerical Simulation of Heat Transfer and Steel Shell Growth in a Curved Slab Mold*, ISIJ International, Vol. 53 (2013), No. 5, pp. 809–817.

49. V. Ludlow, A. Normanton, A. Anderson, M. Thiele, J. Ciriza, J. Laraudogoitia and W. van der Knoop, *Strategy to minimise central segregation in high carbon steel grades during billet casting*, Ironmaking and Steelmaking,32(2005), 68-74.

50. Takeuchi, E. and J. Brimacombe, *The formation of oscillation marks in the continuous casting of steel slabs.* Metallurgical and Materials Transactions B, 1984. 15(3): p. 493-509.

51. Joydeep Sengupta, B.T., *Visualization of hook and oscillation mark formation mechanism in ultra-low carbon steel slabs during continuous casting.* JOMe Journal of the Minerals, Metals and Materials Society, 2006.

52. M.S. Jenkins, Ph.D., *Heat transfer in the continuous casting mold*, thesis (Clayton, Vic., Australia: Monash University, 1999.

53. K.C. Mills, A.B. Fox, R.P. Thackray and Z. Li, *The performance and properties of mould fluxes*, VII International Conference on Molten Slags Fluxes and Salts, The South African Institute of Mining and Metallurgy, 2004.

54. Kenneth C. Mills and Alistair B. Fox, *The Role of Mould Fluxes in Continuous Casting-So Simple Yet So Complex*, ISIJ International, Vol. 43 (2003), No. 10, pp. 1479–1486.

55. I. Samarasekera, D.L. Anderson, and J.K. Brimacombe, *The Thermal Distortion of Continuous-Casting Billet Molds*, I.V. Metallurgical Transactions B, Vol. 13B, 1982, 91-104.

56. I. Samarasekera and J.K. Brimacombe, *The Influence of Mold Behavior on the Production of Continuously Cast Steel Billet*, I.V., Metallurgical Transactions B, 13B, 1982, 105-116.

57. K. Okazawa, T. Kajitani, W. Yamada and H. Yamamura, *Infiltration Phenomena of Molten Powder in Continuous Casting Derived from Analysis Using Reynolds Equation Part 1: Steady Analysis*, ISIJ International, Vol. 46 (2006), No. 2, pp. 226–233.

58. J. M. Harman and A. W. Cramb, *A Study of the Effect of Fluid Physical Properties upon Droplet Emulsification,* Proc. 79th Steelmaking Conf.,1996, P. 773-784.

59. Jari Savolainen, Timo Fabritius and Olli Mattila, *Effect of Fluid Physical Properties on the Emulsification*,ISIJ International, Vol. 49 (2009), No. 1, pp. 29–36.

60. P.R. Scheller, R. Hagemann, *Model Investigations on Slag Entrainment in Continuous Casting*, Vol. 57, No.1, Archives of Metallurgy and Materials, 283-289.

61. Lance C. Hibbeler and Brian G. Thomas, *Investigation of Mold Flux Entrainment in CC Molds Due to Shear Layer Instability*, AISTech, Pittsburgh, PA, May 4-7, 2010.

62. Lance C. Hibbeler, Rui Liu and Brian G. Thomas, *Review of Mold Flux Entrainment Mechanisms and Model Investigation of Entrainment by Shear-Layer Instability.* Metec Conference 2011, Düsseldorf.

63. Lance C. Hibbeler and Brian G. Thomas, *Mold Slag Entrainment Mechanisms in Continuous Casting Molds,* AISTech 2013 Proceedings, Pittsburgh PA, 1215-1230.

64. Z. Xiao, Y. Peng, and C. Liu, "*Modelling study of the entrapment phenomena at the slag-metal interface in the gas-stirred ladle*," Chinese Journal of Metal Science and Technology, vol. 3, pp. 187–193, 1987.

65. Y. Gutierrez , R. Morales, *Control of Meniscus Stability in Medium Thickness-straight Walls Slab Mould,* ISIJ International, Vol. 53 (2013), No. 2, pp. 230–239.

66. J. Sengupta, C. Ojeda and B. G. Thomas, *Thermal-mechanical behaviour during initial solidification in continuous casting: steel grade effects*, International Journal of Cast Metals Research, 22 (2009), No. 1-4,

67. Ojeda, C; Thomas, B.G.; Barco, J.; Arana, J.L.;*Model of Thermal-Fluid Flow in the Meniscus Region During an Oscillation Cycle*; Proc.,AISTech 2007, P. 269-283, AISTech 2007, Steelmaking Conference Proc., (May 7-10, Indianapolis, IN), AIST, Warrendale, PA, Vol. 1, 2007.

68. B. Li and F. Tsukihashi, Vortexing flow patterns in a water model of slab continuous casting slab, *ISIJ International*, 45 (2005), No1, 30-36.

69. Patrick J. Hanley, S.G.K., B. Thomas, *The Making, Shaping and Treating of Steel,*AIST, 2010. Casting Volume(11): p. 287-297, 467-506.

70. B. Thomas, L.M., F. Najjar, *Simulation of Fluid Flow Inside a Continuous Slab Casting Machine.* Metallurgical and Materials Transactions B, 1990. 21: p. 387-400.

71. F. Wilson, M.H., A. Nicholson, A. Hills, *Effect of Fluid Flow Characteristics on Nozzle Blockage in Aluminum-killed Steels.* Ironmaking & Steelmaking, 1987. 14(6): p. 296-309.

72. McPherson, N., *Continuous Cast Clean Steel.* Steelmaking Conference Proceedings, Warrendale Pa., Iron and Steel Society, 1985. 68: p. 13-25.

73. N. Najjar, B.T., D. Hershey, *Turbulent Flow Simulations in Bifurcated Nozzles:Effects of Design and Casting Operations,*Metallurgical Transactions B, 1995. 26(4): p. 749-765.

74. S.Yokoya, S.T., M.Iguchi, Y.Asako, R.Westoff, S. Hara, *Swirling Effect in Immersion Nozzle on Flow and Heat Transport in Billet Continuous Casting Mold.* ISIJ, 1998. 38(8): p. 827-833.

75. S. Yokoya, S.T., H. Souma, M. Iguchi, K. Marukawa, W. Yasugaira, S. Hara, *Development of Swirling Flow Generator in Immersion Nozzle.* ISIJ, 2000. 40(6): p. 584-588.

76. S. Yokoya, S.T., H. Souma, M. Iguchi, Y. Asako, S. Hara, *Removal of Inclusion through Bubble Curtain Created by Swirl Motion in Submerged Entry Nozzle.* ISIJ, 1998. 38(10): p. 1086-1092.

77. S. Yokoya, S.T., M. Iguchi, K. Marukawa, W. Yasugaira, S. Hara, *Swirling flow control in immersion nozzle for Continuous Casting process.* ISIJ, 2001. 41: p. S41-S57.

78. S. Yokoya, S.T., K. Tada, M. Iguchi, K. Marukawa, W. Yasugaira, S. Hara, *Swirling flow effect in Bottomless Immersion Nozzle on Bulk Flow in High Throughput Slab Continuous Casting Mold.* ISIJ, 2001. 41(10): p. 1201-1207.

79. L. Hallgren, S.T., R. Eriksson, S. Yokoya, P. Jonsson, *Effect of Nozzle Swirl Blade on Flow Pattern in Runner during Uphill Teeming.* ISIJ, 2006. 46(11): p. 1645-1651.

80. Z. Zhang, S.Y., A. Tilliander, P. Jonsson, *A Numerical Study of Swirl Blade Effects in Uphill Teeming Casting.* ISIJ, 2010. 50(12): p. 1756-1762.

81. Yokoya, S., et al., *The effect of swirl flow in an immersion nozzle on the heat and fluid flow in a billet continuous casting mold.* Scandinavian Journal of Metallurgy, 2004. 33(1): p. 22-28.

82. S. Kholmatov, S.T., L. Jonsson, P. Jonsson, S. Yokoya, *Development of Flow Field and Temperature Distribution during Changing Divergent Angle of the Nozzle using Swirling Flow in a Square Continuous Casting Billet Mold.* ISIJ, 2007. 47(1): p. 80-87.

83. E. Torres Alonso, R.D.M., S. Garcia-Hernandez, A. Najera Bastida, A. Sandoval Ramos, *Influence of Straight Nozzles on Fluid Flow in Mold and Billet Quality.* Metallurgical and Materials Transactions B, 2008. 39B: p. 840-852.

84. H. Sun, J.Z., *Effect of Feeding Modes of Molten Steel on the Mould Metallurgical Behavior for Round Bloom Casting.* ISIJ, 2011. 51(10): p. 1657-1663.

85. C. Capurro, J. Copola, S. Ferro, C. Cicutti, "*Effect of Submerged Entry Nozzle Design on the Distribution of Inclusions in Cast Products"*, AISTech 2013 Proceedings, Pittsburgh, PA, 1027-1036.

86. Neff, H.P., *Introductory electromagnetics,*1991: Wiley.

87. Moreau, R.J., *Magnetohydrodynamics*1990: Kluwer Academic Publishers.

88. Yu Haiqi Yu, H. and M. Zhu Miaoyong Zhu, *Three-Dimensional Magnetohydrodynamic Calculation for Coupling Multiphase Flow in Round Billet Continuous Casting Mold With Electromagnetic Stirring.* IEEE Trans Magn, 2010. 46(1): p. 82-86.

89. Hirayama, R., K. Fujisaki, and T. Yamada, *Dual in-mold electromagnetic stirring in continuous casting.* Magnetics, IEEE Transactions on, 2004. 40(4): p. 2095-2097.

90. Wu, H.-j., et al., *Effect of M-EMS on the solidification structure of a steel billet.* International Journal of Minerals, Metallurgy, and Materials, 2011. 18(2): p. 159-164.

91. Javurek M., B.M., Gittier P., Rockenschaub K., Lechner M., *Flow Modelling in Continuous Casting of Round Bloom Strands with Electromagnetic Stirring.* Steel Research International, 2008. 79(8): p. 617-626.

92. Barna, M., et al., *Numerical Simulations of Mould Electromagnetic Stirring for Round Bloom Strands.* BHM Berg- und Hüttenmännische Monatshefte, 2009. 154(11): p. 518-522.

93. Sivak, B., et al., *MHD processes in the electromagnetic stirring of liquid metal in continuous section and bloom casters.* Metallurgist, 2009. 53(7): p. 469-481.

94. Yoon, J.K., *Applications of Numerical Simulations to Continuous Casting Technology.* ISIJ, 2008. 48(7): p. 879-884.

95. B. Thomas, R.C. *State of the Art in Electromagnetic Flow Control in Continuous Casting of Steel Slabs: Modeling and Plant Validation*. in *EPM 2009*. 2009.

96. S. Kobayashi, S.I., M. Yoshihara, Y. Sugitani, *Factors Affecting Equiaxed Zone Generation in Electromagnetic Stirring.* Transactions ISIJ, 1988. 28: p. 939-944.

97. S. Kobayashi, S.I., *Analysis of Turbulent Flow Field Induced by Rotating Electromagnetic Field in Round Billets.* ISIJ 1988. 28: p. 754-760.

98. Schlichting, H., *Boundary-layer theory,*1968: McGraw-Hill.

99. H. Mizukamia, M.K., M. Kitagawa, K. Kawakami, *Effect of Electromagnetic Stirring at the Final Stage of Solidification of Continuously Cast Strand.* ISIJ international, 1984. 70(2): p. 194-200.

100. Yazuda, I.O., R. Ishii, S. Fujita, Y. Tamura, Investigation of the Melt Flow on Solidified Structure by a Levitation Technique Using Alternative and Static Magnetic Fields. ISIJ, 2005. 45(7): p. 991-996.

101. Zhou, S.-c., et al., *Effect of low-frequency rotary electromagnetic-field on solidification structure of continuous casting austenitic stainless steel.* Journal of Central South University of Technology, 2009. 16(3): p. 360-364.

102. H. Nakata, T.I., H. Mori, K. Ayata, T. Murakami and T. Kominami, *Improvement of Billet Surface Quality by Ultra-high-frequency Electromagnetic Casting.* ISIJ, 2002. 42(3): p. 264-272.

103. W. Yamada, A.K., J. Nakashima, J. Fukuda, K. Okazawa and K. Miyazawa, *Coagulation and Trapping into Solidified Shell of Nonmetallic Inclusions in Continuous Casting Mold of Steel.* CAMP-ISIJ, 1999. 12(682).

104. Matsumiya, T., *Recent Topics of Research and Development in Continuous Casting (Review).* ISIJ, 2006. 46(12): p. 1800-1804.

105. Y. Tsukaguchi, S.F., M. Kawamoto, *Wood Metal Experiment of Swirling Flow Submerged Entry Nozzle for Round Billet Casting.* ISIJ, 2004. 44(2): p. 350-355.

106. K. Stransky, F.K., B. Sekanina, J. Stetina, V. Gontarev, J. Dobrovska, *The Effect of Electromagnetic Stirring on the Crystallization of Concast Billets.* Materials and Technology, 2011. 45(2): p. 163-166.

107. K. Ayata, T.M., T. Fujimoto, T. Ohnishi, I. Wakasugi, *Improvement of Macrosegregation in Continuously Cast Bloom and Billet by Electromagnetic Stirring.* ISIJ, 1984. 24.

108. T.H. Shih, W. W. Liou, A. Shabbir, Z. Yang, and J. Zhu: *Computers Fluids*, 24(1995), 227.

109. ANSYS-FLUENT 14.0 User Guide.

110. S.B. Pope, *Turbulent Flows*, Cambridge University Press, Cambridge, London, New York, (2000), 83-92.

111. R. Issa, A.D. Gossman and A.P. Watkins, *The Computation of Compressible and Incompressible Recirculating-flows by a Noniterative Implicit Scheme*, Journal of Computational Physics, 1986, 62, 66-82.

112. Lee G, B .G. Thomas, H.J. Shin, S.K. Baek, C.H. Choi, D.S. Kim, S.J. Yu and S.H. Kim, *S. Kim*, *Microstructure Near Corners of Continuous-cast Steel Slabs Showing Three-dimensional Frozen Meniscus and Hooks,* Acta Materialia, 55 (2007), 6705-6712.

113. N. Kasai, M. Iguchi, *Water Model Experiment on Melting Powder Trapping by Vortex in the Continuous Casting Mold*, ISIJ Int., 47 (2007), 982-987.

114. Q. He, *Observations of Vortex Formation in the Mould of a Continuous Slab Caster*, ISIJ Int, 33 (1993), 343-345.

115. A. Najera, *Fluid Flow and Heat Transfer Analysis for the Continuous Casting of Billet Molds,* Ph.D. Thesis, National Polytechnic Institute, Mexico City.

116. S. Garcia, R.D. Morales, J.J. Barreto and Ken Morales-Higa, *Numerical Optimization of Nozzle Ports to Improve the Fluidynamics by Controlling Backflow in a Continuous Casting Slab Mold*, ISIJ International, Vol. 53 (2013), No. 10, pp. 1794.–1802.

117. Saul Garcia-Hernandez, R.D. Morales, J. De J. Barreto, *Numerical Optimization and Design of Nozzle Ports to Improve the Fluidynamics in a Curve Slab Mould,* 5th International Congress on the Science and Technology of Steelmaking 2012, Dresden, Oct. 1-3.

118. K. Morales-Higa, R.I.L. Guthrie, M. Isac, R.D. Morales, C. Labrecque, F. Lapointe, *A Fluid Flow and Steel Intermixing Study of a Round Billet Mold*, AISTech 2013 Proceedings, Pittsburgh PA, 1373-1384.

119. K. Morales-Higa, R.I.L. Guthrie, M. Isac, R.D. Morales, C. Labrecque, F. Lapointe, *The Effects of Fluid Flow on Flux Entrainment in a Square Billet Mold, AISTech 2013 Proceedings,* Pittsburgh PA, 1461-1472.

120. K. Morales-Higa, R.I.L. Guthrie, M. Isac, R.D. Morales, C. Labrecque, F. Lapointe, *A Comparative Study of Multiport Nozzles in a Square Billet mold*, 8th European Continuous Casting Conference, Graz Austria, 477-486.